A fundamental study on plasmonic hot electron injection using photo-electrochemistry

Anirudh Venugopal

Technische Universiteit Delft

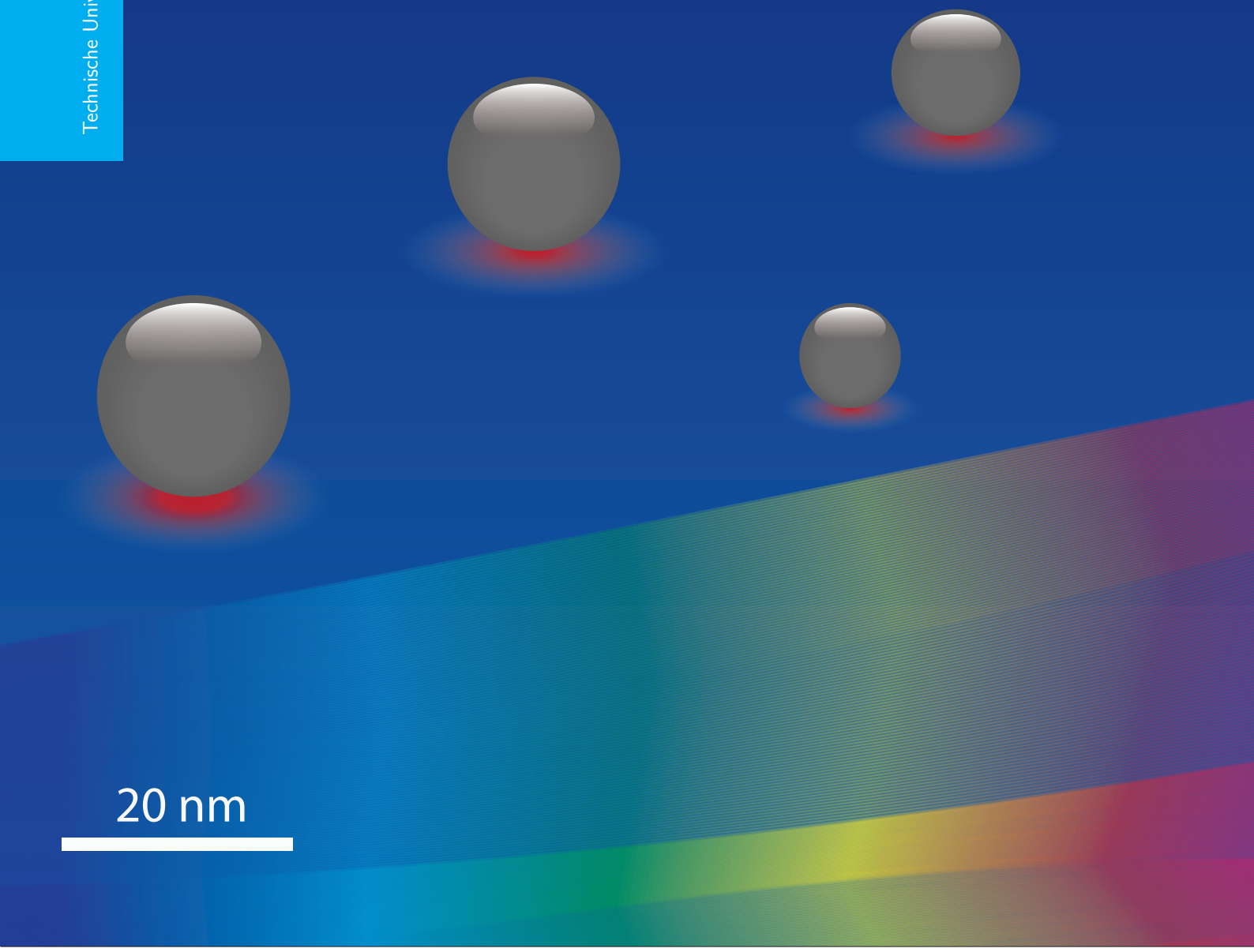

TU Delft Delft University of Technology

Challenge the future

A FUNDAMENTAL STUDY ON PLASMONIC HOT ELECTRON INJECTION USING PHOTOELECTROCHEMISTRY

by

Anirudh Venugopal

in partial fulfillment of the requirements for the degree of

Master of Science

in Chemical Engineering

at the Delft University of Technology,

to be defended publicly on Wednesday May 10, 2017 at 10:00 AM.

Student number:	4450051	
Supervisors:	Dr. Wilson Smith	
	Prof. Dr. Andreas Schmidt-Ott	
	Marco Valenti	
Thesis committee:	Dr. Wilson Smith,	MECS, TU Delft
	Prof. Dr. Andreas Schmidt-Ott,	MECS, TU Delft
	Dr. David Vermaas,	TP, TU Delft

This thesis is confidential and cannot be made public until December 31, 2017.

TU Delft Delft University of Technology

ABSTRACT

Owing to global warming and fast depleting fossil reserves, the world is currently witnessing an energy transition into cleaner and greener energy sources like the wind and solar energy. At present, most of this clean energy is converted into electricity and used up directly or stored in the grids or batteries to be used later. Chemical storage of this energy is an attractive alternative due of its high energy density. Artificial photosynthesis is a hot field wherein researchers try to mimic the photosynthesis process of plants and try to convert solar energy into chemicals that can be stored. Photo-electrochemical (PEC) water splitting is one such pathway that is extensively investigated. However, the ideal semiconductor required to make this conversion efficient and economical is yet to be discovered. A big share of research also focuses on materials or techniques to improve the performance of these PEC devices independent of the semiconductor. Plasmonics, or plasmonic hot electron injection in particular, is such a technique that is being extensively investigated.

Plasmonic hot electron injection is a relatively new phenomenon that could have potential application in many fields including photo-electrochemistry and photovoltaics. It is coveted as one of the techniques that could directly improve the performance efficiencies of solar and photo-electrochemical cells. But a fundamental understanding of this phenomenon is still lacking. This is crucial for improving and optimizing this technology before it can have any practical application. In this thesis, photo-electrochemistry is used as a tool to study the plasmonic hot electron injection and shed more light on the fundamental aspects, at the nanoscale, involved in the excitation and injection of hot electrons into the conduction band of a semiconductor. Silver, gold and 50% silver – 50% gold alloy nanoparticles are used in this work to systematically study the effect of composition, size and concentration of these nanoparticles on the hot electron injection efficiency. Through this work, some fundamental understanding of the factors affecting the energy of the excited hot electron and hot electron injection process is obtained.

ACKNOWLEDGEMENTS

This thesis would not have been a success without the help and support from many. I would like to begin by thanking Prof. Andreas Schmidt-Ott whose lectures on nanoparticle technology inspired me to work in this field for my master thesis. He offered me this thesis topic and introduced me to Dr. Wilson and Marco Valenti and for that I would like to thank him. As an expert in nanoparticle technology, he was there to share his knowledge when I was looking for answers. I would also like to thank Dr. Wilson for finding time for me when I needed it the most. The enthusiasm he shares during the Smithlab group meetings always sends out a positive vibe. Next, I would like to thank Dr. David Vermaas for accepting my invitation to be in my master thesis defence committee.

I would like to thank Ir. Herman Schreuders, who took time out of his schedule and did the sputtering depositions for me and also for all the other help. Same goes to Ir. Joost Middlekoop,for providing us with the everything we need to work smoothly. I would also like to thank Ruben Geutjens who helped me with his experience with the spark set up, when I had troubles. I would like to thank everyone else within the MECS group who helped me at different points. I would also like to address my gratitude to Dr. Wiel Evers (OM, TU Delft) who helped me with the TEM analysis. I would also like to thank Nienke Firet for helping us with the XPS measurements.

I cannot thank enough the support Marco Valenti has given me as a daily supervisor. He was always there to share his knowledge and clear my doubts. The excitement and energy he brings always passed on positive energy to me and my work. I am sure his childlike curiosity for science and the energy he always carries will take him to the heights he envision. I wish him good luck for all his future endeavours.

I would also like to thank all my friends at the TU who supported me throughout this past two years. It was a fantastic learning experience for me and they all contributed to that. Life would have been different without them.

Last, but not the least, I would like to thank my family who was there with me through my up's and down's. I am nothing without them in my life.

Anirudh Venugopal
25 - 04 - 2017

CONTENTS

1

INTRODUCTION

With rapid advances in technology and health care, there has been an exponential increase in human population over time. The average energy usage per person has also gone up during this period. As of 2016, there are about 7.4 billion people around the world consuming more than 14000 Mtoe of energy.[1, 2] The demand is only going to go up in the future with further advances in technology. Catering to this energy demand is a challenge that the society will have to face in the future. At present, most of the energy requirements are met through fossil fuels, namely - coal, oil and natural gas. These resources are finite and hence cannot fuel our lives forever. Statistics say that there is enough fossil fuels to supply to our needs for another few centuries. But we will start to feel the effect of these diminishing resources sooner, either with increasing prices or with shortage of supply, mainly because of the unconventional nature of these resources.

Even if we had infinite amounts of fossil reserves left, there are more pressing issues that push for this energy transition to non-polluting energy sources. Global warming, catalysed by the use of these fossil fuels, is already causing serious damage to our environment. A transition into clean, renewable energy substitutes for fossil fuels is touted as the only solution to tackle this. At the Paris climate change summit 2015, the world leaders collectively agreed on the urgent need for this transition. They have agreed on cutting carbon emissions from their countries and setting ambitious targets on producing energy from renewable energy sources. Solar, wind and tidal energy are some of the options these countries could focus on for renewable energy, depending on their geographical advantages. This transition cannot be done single-handedly by a corporation or a country. It requires extensive cooperation between countries and also between research institutes and technical universities like TU Delft, doing their small bit and aiding this transition.

1.1. MOTIVATION

Energy from the sun could be one of the main sources of clean energy in the future. Figure 1.1 shows the energy potential of different forms of clean energy sources available. Depending on geographical locations, different combinations of these sources would be the best solution for the energy requirements of that location. What is clear from figure 1.1 is the massive potential of solar energy compared to other sources. But one common problem pointed out when there is a discussion on solar energy is the erratic nature of this energy source. This erratic nature can disrupt the energy supply line and is not ideal. One solution is to store the energy when it is produced and then use it according to demand. Chemical storage of solar energy is one of the most effective ways to store this energy because of high energy density (Appendix A) of such fuels compared to other options like batteries. Artificial photosynthesis can be used to convert solar energy to fuels. Photo-electrochemical (PEC) hydrogen production is a way to implement it in practice. But this technology is still in its early stages of development and has to achieve sufficient improvements in terms of efficiency before it can be used in practice. One way to improve this efficiency is to make use of plasmonic nanoparticles. To be specific, plasmon induced hot electron injection was recommended as a way to improve the efficiency

of such devices [3, 4]. But this concept still needs further understanding at the fundamental level before we can evaluate its true potential. Through this master thesis, this possibility is studied experimentally to see the practical increase in the efficiency of these devices due to plasmon induced hot electron injection and to understand the factors effecting it.

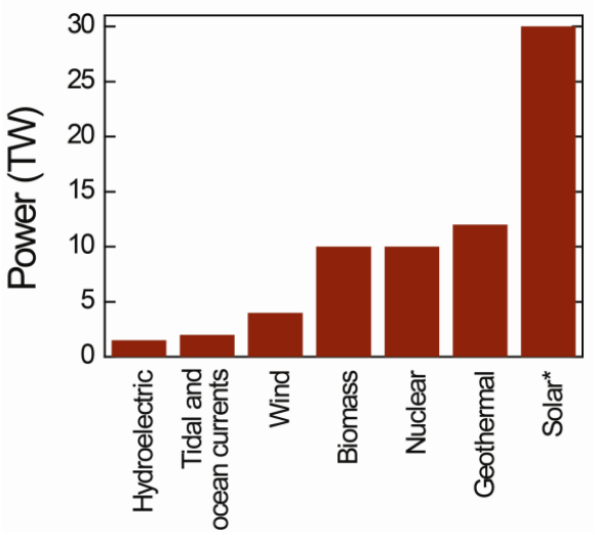

Figure 1.1: Power generating potential of different renewable energy sources (globally) [5]

1.2. CONCEPT

1.2.1. WHY ARTIFICIAL PHOTOSYNTHESIS?

Life on earth – our food and oxygen supply – is sustained by the conversion of solar energy to chemical energy by plants through the process of biological photosynthesis. In this process the plants use abundant resources like carbon dioxide and water along with the energy from the sun to produce oxygen and other chemical compound which serves as the "fuel" for plant life. For decades, we have been trying to mimic this process; using sunlight to drive thermodynamically uphill the reactions involving earth abundant materials to produce fuels. A clean and storable energy source from solar energy is considered as the "holy grail" by many. In 1972, Fujishima & Honda [6, 7] provided a breakthrough to this field by demonstrating photo-electrochemical water splitting to produce hydrogen and oxygen gas using TiO_2 semiconductor photo-anodes. Subsequently, many semiconductors have been investigated for solar water splitting [8–10]. The solar to hydrogen conversion efficiency of the current devices needs further improvement, before they can be used for practical purposes.

The band gaps of most of these semiconductors are in the UV region and blue part of visible region of light spectrum. Only 5% of the sunlight accounts for this UV region. A major fraction, 45% of the light spectrum, is for the visible light.[11] Most of this part is unused by these semiconductors and hence extending the light absorption of these semiconductors in the visible region would be an obvious way to improve the efficiency of these devices. Also the electronic and catalytic properties of these semiconductors are far from ideal and hence often exhibit poor reaction kinetics. One way to improve these devices in terms of light absorption and electronic properties is to decorate the semiconductor surface using plasmonic nanoparticles.[3, 4, 12]

1.2.2. WHY PLASMONICS?

Plasmonics is a jewel in the fascinating field of nanophotonics. It a result of the direct interaction between the electromagnetic waves (or light) and the conduction electrons of the light incident metallic surfaces or metallic nanostructures. These plasmons (or surface plasmons) are electromagnetic waves that propagate on metal surfaces with free electrons, upon illumination with solar radiation. These free electrons start oscillating with

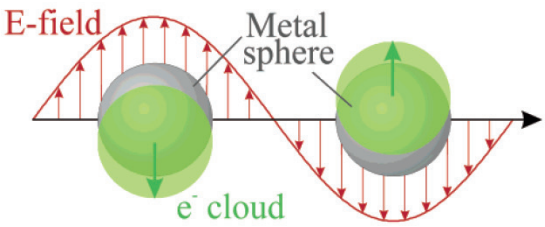

Figure 1.2: Schematic illustration of Surface Plasmon Resonance in metal nanoparticles [13]

the incoming light waves, creating a resonance. These resonant interactions give rise to unique properties for these materials [3, 4, 14–16]. When the surface plasmon excitation is on isolated metallic nanoparticles, the electron excitations are confined and this results in Localised Surface Plasmon Resonance (LSPR). By decorating the surface of thin film semiconductor photoelectrodes with plasmonic nanoparticles, the LSPR can be used to improve its performance [3, 4, 12, 16]. This is done either by confining the light or scattering back the unabsorbed light and increasing its path length within the semiconductor for improved absorption efficiency. These are the indirect ways LSPR can improve the performance of such devices. Plasmonic nanoparticles also improve the electronic and catalytic properties of the semiconductor when it is placed in the semiconductor-electrolyte interface. Above this, the LSPR can directly improve the performance by injecting high energy electrons (called "hot-electrons") into the conduction band of the semiconductor [3, 4, 12, 17, 18], increasing the photo-electrochemical water splitting efficiency of the cell.

1.2.3. WHY PLASMON INDUCED HOT ELECTRON INJECTION?

After the LSPR excitation in these nanostructures, the resonance starts to decay in a femtosecond time scale[3]. This can happen either by the radiative or the non-radiative path ways [4]. For particles of size less than ~ 40 nm, the non-radiative path ways of plasmon decay is the preferred mechanism. This non-radiative pathway results in the formation of electrons with energy higher than the fermi-level of the metal, called the hot electrons. If this hot electrons can be successfully extracted from the metal nanoparticle, it can be used to drive chemical reactions. If the hot electrons have sufficient energy to overcome the metal-semiconductor Schottky barrier, it can be injected into the conduction band of the semiconductor and then sent to the cathode via an external circuit for the reduction of hydrogen ions. This plasmon induced hot electron injection (HEI) mechanism offers many advantages over other plasmonic enhancement mechanisms [4]. The HEI helps to absorb light outside the optical band gap edge (OBGE) of the semiconductor, there by extending the light absorption capabilities of the device to a larger spectrum. Since it is a direct enhancement mechanism, the efficiency enhancement does not depend on the type of the semiconductor and hence can be plugged into any semiconductor without affecting its performance. The plasmonic resonance and hence the HEI, can be tuned depending on the particle size, shape, composition and the surrounding environment such that it is outside the OBGE of the semiconductor and hence does not screen light to the semiconductor. Yet this phenomenon of plasmon induced hot electron injection is not fully understood, mainly because of its recent discovery. Therefore, sufficient research has to be done on the plasmon induced HEI at the fundamental level before we can evaluate its true potential. This master thesis aims to explore and explain certain aspects of the plasmon induced HEI from a fundamental level.

1.2.4. RESEARCH QUESTIONS

The field of plasmonics is yet to gain complete understanding of the parameters that effects the plasmon induced hot electron energies and its injection efficiencies. At present, the reported values of efficiencies of hot electron injection are really low, for any practical use. [19] Only with a complete understanding of these concepts, we can optimize this technology and facilitate its practical application. The goal of this research is to contribute to the field of plasmonics, by trying to fill some of these knowledge gaps in terms of fundamental understanding of the factors that affect the plasmonic hot electron injection phenomenon. Through this thesis, answers to the following questions are experimentally investigated:

- What is effect of tuning the surface plasmon resonance, by alloying two plasmonic nanoparticles, on the plasmonic hot electron energies and injection efficiency?
- What is the effect of the size of the nanoparticle on the plasmonic hot electron injection efficiency?
- What is the effect of the number density (or concentration) of nanoparticles, on the substrate surface, on the plasmonic hot electron injection efficiency?

1.2.5. APPROACH

Spherical plasmonic nanoparticles are the best choice to do such fundamental studies mainly because of their isotropic plasmonic behaviour. Silver and gold nanoparticles are used for this study because of their activity in the visible region of light. The plasmonic nanoparticles used in this work are prepared using the spark ablation technique. Spherical nanoparticles of different sizes can be easily synthesized using this technique. 10nm TiO_2 film on an FTO substrate is used as the semiconductor. The high optical band gap edge of ~ 380 nm of TiO_2 helps to independently study the plasmonic hot electron injection phenomena. The synthesized plasmonic nanoparticles are characterised using UV-Vis spectroscopy, Transmission Electron Microscopy (TEM) and X-Ray Photoelectron Spectroscopy (XPS) measurements. The hot electron injection of these plasmonic nanoparticles is studied using photo-electrochemistry techniques like IPCE measurements and cyclic voltammetry. These techniques offer an easy way to study the composition, size, concentration and wavelength dependent properties of these plasmonic nanoparticles.

1.2.6. REPORT OUTLINE

This report consists of 7 chapters including this one. A brief outline of the concepts involved in this work is discussed in Chapter 2. Chapter 3 discusses the experimental procedures and details of the equipment's used for this work. In Chapter 4, the important results from this work is presented. Detailed discussions on these results are left for Chapter 5. In Chapter 6 & 7, the important conclusions from this work and some recommendations for the future are presented.

2

THEORY

2.1. PHOTOELECTROCHEMICAL (PEC) WATER SPLITTING

Photo-electrochemical (PEC) water splitting using semiconductor photo-electrodes has many advantages over other conventional water splitting methods. One of the main advantage is that the oxygen and hydrogen evolution is on different electrodes and can be spatially separated. This is an important safety aspect as hydrogen is easily flammable [20] and also allows for the easy separation of these gases. Such photo-electrodes are mainly constructed from inorganic materials and provides with longer durability compared to the routes that make use of organic and biological components. A route that can closely compete with photo-electrochemical water splitting is the photovoltaic-electrolysis (PV-E) route. All the advantages mentioned above are also applicable for the PV-E route. But the PEC route offers two additional advantages over the PV-E route in terms of lower overpotential required because of the low current densities involved [20, 21] and also lower manufacturing costs because of its compact size [20]. An ideal photo-electrode should fulfil several contradicting tasks at once – high light absorption, good charge separation and charge transport and facilitate easy hydrogen or oxygen evolution reactions at the surface. The photo-electrode material should also be cheap and should be stable in aqueous conditions. There is no material currently that can offer us all these advantages. Therefore, trade-offs have to be made and metal oxide semiconductors are the ones that come close.

A simple PEC cell consists of atleast three components – a photo-electrode, a metal counter electrode and an electrolyte. Since a metal oxide semiconductor was used as a photo-anode for this thesis, the focus of this section would be on the mechanism of such a setup. The incoming photons excite the electron from the valence band of the semiconductor to its conduction band, leaving a vacancy or a hole in the valence band. A minimum photon energy, that is equivalent to or more than the band gap of the semiconductor, is required to excite this electron to the conduction band. Once the electrons are spatially separated from the holes, they are sent to the metal counter electrode, via an external circuit, where it is used to reduce hydrogen ions. The left over holes in the valence band of photo-anode is used to oxidize water to produce oxygen gas. [20] A simple schematic illustration of this mechanism can be seen in figure 2.1. The two half reactions are as depicted below. The reaction potential of each half reactions are also mentioned [22]. The required cell potential is calculated from equation 2.1. Therefore, thermodynamically, a cell potential of 1.23 V is required to drive the water splitting reaction.

$$4\,H^+ + 4\,e^- \rightleftharpoons 2\,H_2 \qquad E^0{}_{red} = 0.00\ \text{V vs NHE}$$

$$2\,H_2O + 4\,h^+ \rightleftharpoons 4\,H^+ + O_2 \qquad E^0{}_{red} = 1.23\ \text{V vs NHE}$$

$$E^0_{cell} = E^0_{cathode} - E^0_{anode} = 0 - 1.23 = -1.23\ \text{V vs NHE} \tag{2.1}$$

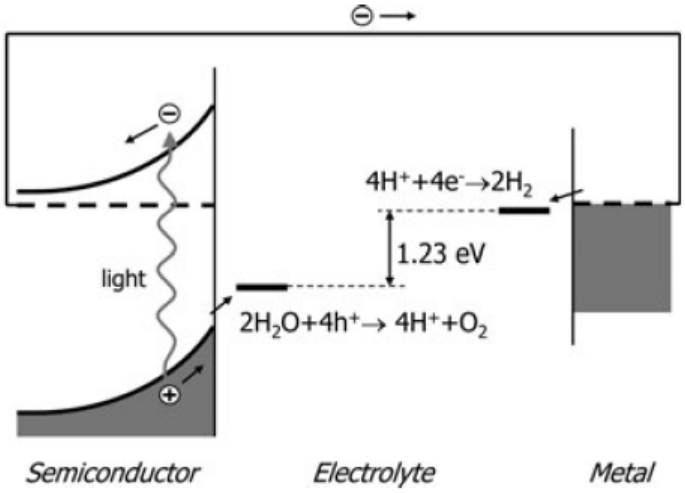

Figure 2.1: Illustration of photo-electrochemical water splitting [20]

2.1.1. METAL-OXIDE SEMICONDUCTORS AS PHOTO-ANODES FOR WATER SPLITTING

To achieve a high conversion efficiency, high absorption of visible light by the semiconductor electrode is necessary. For the past few decades, metal oxide semiconductors (TiO_2, Fe_2O_3, $BiVO_4$ etc.) have been investigated as PEC photoanodes [23]. The thermodynamic potential required for water splitting reaction is 1.23 V. Therefore a minimum band gap of 1.23 eV is required for the semiconductor to efficiently facilitate each half reaction. This is schematically represented in figure 2.1. Considering the thermodynamic losses and overpotentials a minimum of 1.9 eV is required as the bandgap of the semiconductor [24–26]. To achieve the standard target of 10% solar to hydrogen conversion efficiency for the device, an average current density of 8 mA/cm^2 is required. This would translate to a maximum band gap of around 2.4 eV. Therefore, the ideal semiconductor should have a band gap between 1.9 eV – 2.4 eV. Murphy et al. [25] estimated that the band gap of an ideal semiconducting photo-anode to be 2.03 eV. To summarise, semiconductors suitable to be used as photo-anodes should have the following traits :-

- High chemical stability under all cell conditions
- A band gap of approximately 2 eV
- Suitable positioning of the bands in terms of oxidation and reduction potentials required for water splitting
- Good catalytic activity and charge transport properties
- Cheap and abundant material and processing technique

However, this ideal photoanode material is yet to be discovered. The current photoanode materials which have lower band gap, i.e. those that can absorb the visible light well, lack stability under operating conditions and vice versa.

2.2. PLASMONICS IN METAL NANOPARTICLES

In the 1980's, it was experimentally shown that by directing light into the interface between a metal and a dielectric, such as air or glass, a resonant interaction can be induced between the electromagnetic waves of light and the free electrons at the surface of the metal [27]. That is, the oscillations of the free electrons at the surface of the metal matches that of the electromagnetic waves outside the metal. This results in a density

wave of free electrons, called surface plasmons, which propagates along the metal-dielectric interface like ripples in water. From then on, this field was known by the name "plasmonics" and the resonant interaction is known as surface plasmon resonance. The research in this field has grown substantially in recent years and plasmonics have found applications in different fields ranging from chemical and biological detectors and spectroscopy to photo-electrochemistry [14]. If the free electron excitations by the electromagnetic waves are on small metal nanoparticles in a dielectric environment, the plasmonic interactions are localised and is hence known as localised surface plasmon resonance (LSPR) [28].

2.2.1. ELECTROMAGNETIC WAVES IN CONFINED SPACES

Maxwell's equations can be used to understand the interaction of small metal nanoparticles with light from a classical framework. Maxwell's equations for the electromagnetic waves of light are as follow [28]:-

$$\nabla.D = \rho_{ext} \tag{2.2}$$
$$\nabla.B = 0 \tag{2.3}$$
$$\nabla \times E = -\frac{\delta B}{\delta t} \tag{2.4}$$
$$\nabla \times H = \frac{\delta D}{\delta t} + J_{ext} \tag{2.5}$$

where D is the dielectric displacement, E is the electric field, H is the magnetic field, J is the current density, ρ is the charge density and B is the magnetic flux density and for an isotropic and non-magnetic material,

$$D = \epsilon_0 \epsilon E \qquad\qquad B = \mu_0 \mu H \tag{2.6}$$

where ϵ_0 and μ_0 is the electric permittivity and magnetic permeability of vacuum, respectively. ϵ is the relative permittivity and μ is the relative permeability of the nonmagnetic medium. Maxwell assembled these equations to help explain the propagation of light waves in a medium. Through these equations he suggested that when an electromagnetic mode oscillates, in every half period, the energy is transferred from electric field energy to magnetic field energy and back. This way the oscillations are self-sustaining. This is pictorially demonstrated in figure 2.2 (a). This is true when the characteristic length a » λ/2n, where n is the refractive index. But when the characteristic length a « λ/2n, the phase of harmonically oscillating waves in that confined space is practically constant. If it is assumed that the electric field is dominating in this region, then the contribution of magnetic field and hence the magnetic energy is small. This is again demonstrated in figure 2.2 (b). Therefore, the propagation cannot be self-sustaining unless there is another form of energy to make a balance with the electric field energy. In case metal nanoparticles, which contains free carriers, this balance can be restored by storing energy in the form of kinetic energy of these free carriers [19].

$$U_E \approx \frac{1}{2}\epsilon E^2 \tag{2.7}$$
$$U_H \approx \frac{1}{2}\frac{1}{\mu}H^2 \tag{2.8}$$
$$U_K \approx \frac{1}{2}\epsilon_0 \frac{\omega_p^2}{\omega^2}E^2 \tag{2.9}$$
$$U_E = U_K + U_H \tag{2.10}$$

Thus in confined spaces, depending on the geometry under consideration, the energy balance can be restored at certain frequencies ω_{spp}. This is precisely the frequency of surface plasmon polarisations (SPP's). The spatial dependence of the wave in this confined region is given by $\sin(\pi z/a)$ [19]. Therefore, as the characteristic length decreases (smaller nanoparticle size), lesser the contribution of magnetic energy and hence

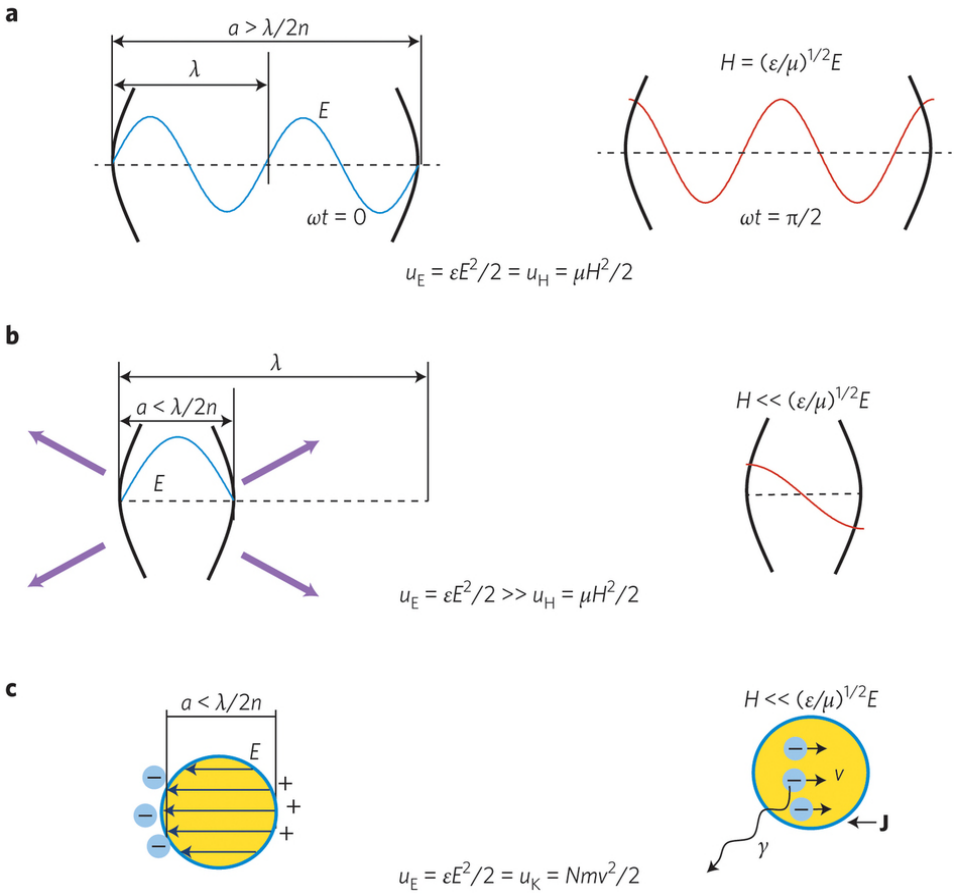

Figure 2.2: (a) Electromagnetic wave propagation in a free space (b) Electromagnetic wave propagation in a confined space (c) Oscillating electrons or plasmons in the metal nanoparticle [19]

more energy is stored in the form of kinetic energy of these free carriers. More kinetic energy implies that more momentum is also imparted to these free carriers (excited electrons). Since the contribution of magnetic field is negligible, as per faraday's law the electric field is nearly irrotational - resembling an electrostatic field.

2.2.2. SMALL SPHERICAL METAL NANOPARTICLES

This resonance enhanced field is homogeneous throughout the volume of very small particles ($a \ll \lambda$) and produces a dipolar field outside the particle. This results in an enhanced near field around the particle and enhanced absorption and scattering cross-section for the electromagnetic waves [29]. The resonant behaviour in these small metal nanoparticles is a result of the confinement of the electrons in the small volume. These electrons all moves in phase with the incoming light waves and leads to a build-up of charges on the surface, which act as a restoring force. This condition results in a resonance with a particular frequency known as plasmon frequency. The electrons move in a $\pi/2$ phase lag with the driving field [30].

For spherical nanoparticles, the Clausius – Mossotti relation [29] connects the dielectric function with the particle polarizability α,

$$\alpha = 3V \frac{\epsilon_d - \epsilon_m}{\epsilon_d + 2\epsilon_m} \tag{2.11}$$

where V is the volume of the particle, ϵ_d is the permittivity of the particle and ϵ_m is the permittivity of the medium. The absorption and scattering cross sections of small spherical nanoparticles of arbitrary sizes,

proposed by Gustavo Mie [31] can then be simplified as in equations 2.12 and 2.13, where k is the wavenumber. This simplification is valid in the range $ak \ll 1$ and $mak \ll 1$ where, a is the diameter of the particle and m is the relative refractive index of the particle with respect to the medium. The relation developed by Mie has later been developed to accurately predict the absorption and scattering cross-sections of particles of different shapes as well [32].

$$C_{sca} = \frac{k^4}{6\pi} \mid \alpha^2 \mid \tag{2.12}$$

$$C_{abs} = k\Im m(\alpha) \tag{2.13}$$

The drude permittivity for spherical nanoparticles is given by [33],

$$\epsilon_d(\omega) = \epsilon_\infty - \frac{\omega_p^2}{\omega^2 + i\gamma_d\omega} \tag{2.14}$$

where, $\epsilon_d(\omega)$ is the frequency permittivity of the metal. ϵ_∞ accounts for the additional screening of the positive ion core by the bound valence electrons. ω_p is the bulk plasma frequency which is dependent on the electron density, ϵ_0 is the vacuum permittivity and γ_d is the damping of electrons due to electron-phonon scattering in the metal. From this the frequency dependent dielectric function of the metal can be derived, which is the ratio of the frequency dependent permittivity of the metal to the permittivity of free space (ϵ_0). Therefore from equations 2.12 and 2.13, the relation between the scattering and absorption cross-sections to the diameter of the particle can be written as [34],

$$C_{sca} \propto \frac{a^6}{\lambda^4} \tag{2.15}$$

$$C_{abs} \propto \frac{a^3}{\lambda} \tag{2.16}$$

where, a is the diameter of the particle. From these relations, it can be summarised that for very small particles (<25 nm) the absorption cross-section dominates over the scattering cross-section. This absorption and scattering cross-sections dictate the response of the spherical nanoparticle to the incoming electromagnetic waves. Therefore, from the above equations, it is evident that the polarizability determines the optical properties of the spherical nanoparticle and have a maximum when the denominator of the equation 2.11 is zero. The frequency at which this happens is the surface plasmon resonance frequency.

2.2.3. TUNING OF SURFACE PLASMON RESONANCE FREQUENCY

BY VARYING NANOPARTICLE SIZE

From the Clausius – Mossotti relation given in equation 2.11, for a particular surrounding medium and spherical metal nanoparticle, the polarizability is dependent on the size of the particle and the frequency dependence of the dielectric constant of the nanoparticle material. As explained in the previous section, the surface plasmon resonance frequency is the frequency at which you have the maximum polarizability of the nanoparticle material. Therefore, for metal nanoparticles of different diameters, the frequency at which the polarizability is maximum is different. Hence, by changing the nanoparticle size, we can tune the surface plasmon resonance frequency. From equations 2.12 and 2.13, the nanoparticle will have maximum extinction cross-section (sum of absorption and scattering cross-section) at this resonance frequency. Therefore, a shift in this maximum is observed from absorption measurements by UV-Vis spectroscopy, by changing the nanoparticle size. These shifts in plasmon resonance frequency with particle size were shown by El-Sayed et al. [35]. The resonance wavelength blue shifts with decrease in particle size. In practice, these shifts are really small (< 1 nm with a change in particle size by 3-4 nm) and hence often not visible or hard to distinguish.

BY VARYING THE SURROUNDING ENVIRONMENT

Another factor that is included in the Clausius – Mossotti relation is the permittivity/dielectric constant of the surrounding medium. With a constant nanoparticle size, maximum polarizability is obtained at when the denominator of this equation is zero. That is,

$$\epsilon_d(\omega) = -2\epsilon_m \tag{2.17}$$

Therefore, the frequency at which this relation is satisfied is the plasmon resonance frequency. From this it is clear that by changing the surrounding environment, we can tune the surface plasmon resonance frequency. G. Xu et al. demonstrated the shift in plasmon resonance frequency of silver by coating it with titanium dioxide. [36].

BY VARYING NANOPARTICLE SHAPE

Mie theory described in section 2.2.2 is applicable only for spherical nanoparticles. For other shapes, this theory was modified by Richard Gans and is known as Mie-Gans theory [29]. It gives a modified equation for the polarizability of the particle by accounting for the geometric shape of the particle. This would then have an effect on the plasmon resonance frequency similar to the above explanations. Therefore, by changing the aspect ratio of the particle, we can tune the surface plasmon resonance frequency.

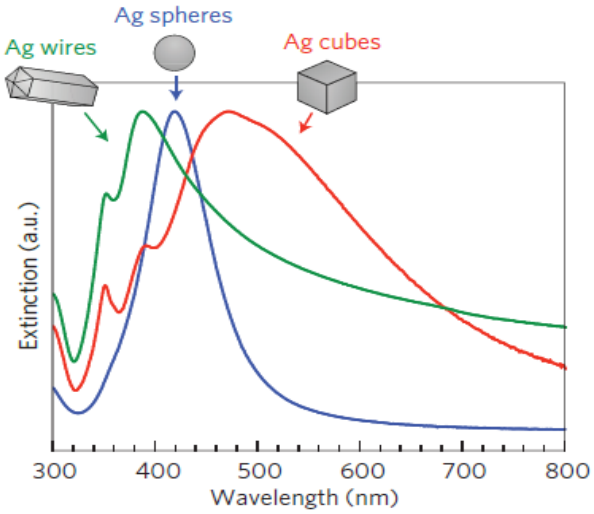

Figure 2.3: Shift in plasmon resonance peak with different nanoparticle shapes [37]

BY VARYING THE NANOPARTICLE COMPOSITION

Different metals have different frequency dependent dielectric constant. As per the drude model, given in equation 2.14, dielectric constant is proportional to the plasma frequency ω_p. This plasma frequency is given by [38],

$$\omega_p = \sqrt{\frac{Ne^2}{\epsilon_0 m_{eff}}} \tag{2.18}$$

where, N is the electron density and m is the effective mass (accounting for the coupling with the ion core) and e is the charge of one electron. This suggests that different metals have different dielectric constant because of different electron density in their valence band. It follows from equation 2.11, that different metal also have different plasmon resonance frequency. The reported values of plasmon resonance wavelength for

gold and silver spherical nanoparticles are around ~ 500 nm and ~ 380 nm in air [37], respectively. By alloying two metals, we can produce a new material with a different electron density in valence band. This way, we can tune the surface plasmon resonance frequency by changing the ratio of two metals in the alloy. This has been demonstrated by El-Sayed et al. by producing alloy nanoparticles of gold and silver in different ratios [38].They suggested a linear dependence in the plasmon resonance wavelength shift with alloy composition.

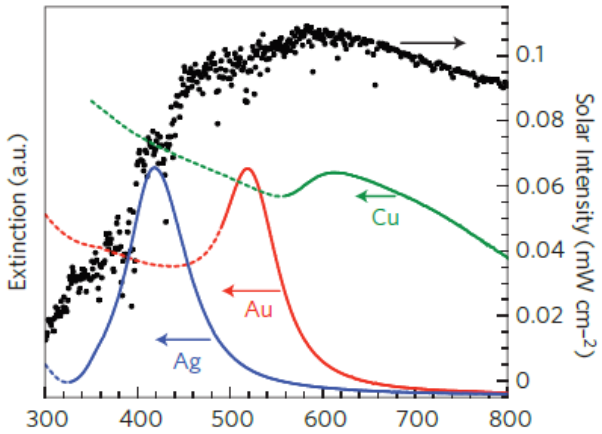

Figure 2.4: Valence band electron density dependence of the surface plasmon resonance. That is one reason why you have different plasmon resonance frequencies for different metals [37]

2.2.4. SIZE DEPENDENCE OF PLASMONIC NEAR FIELD

Optical enhancements in plasmonic devices are directly dependent on the plasmonic near field ($\|E_n^2\|$) of the particles. Such enhancements leads to an increased rate of electron-hole formation.[4] This is the reason why geometric shapes with sharp tips are preferred for plasmonic applications as they give more optical enhancement because of its stronger plasmonic near field. The size dependence of this plasmonic near-field of gold nanoparticles were experimentally studied by Deeb et al. [39] and validated it using their electrodynamic simulations. They show that the size dependence of the plasmonic near field of a spherical gold nanoparticle has a volcanic plot like structure with a peak at 50 nm. They attribute such behaviour to the interplay between three competing factors – non-radiative damping, radiative damping and dynamic polarization. Non-radiative damping of surface plasmons is favoured for small sized nanoparticles (< ≈ 25 nm) whereas radiative damping is the favoured decay mechanism for bigger nanoparticles. The dynamic polarization has a dual effect. It results in the damping of the field for large particle (>50nm) and reduces dissipation for small particles (<50nm). [39, 40] A same trend for size dependence of the plasmonic near field can be expected for silver nanoparticles, though, the peak position and magnitude of the plasmonic near fields would be different.

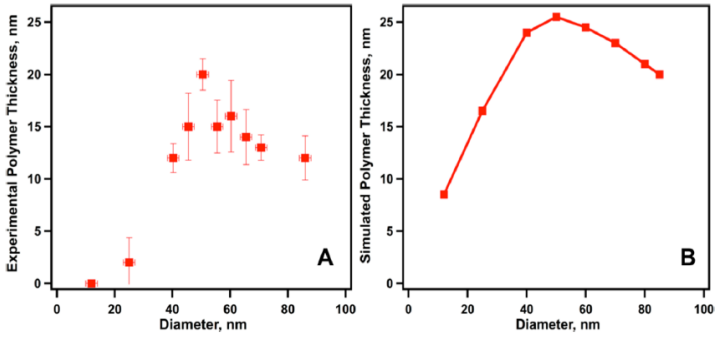

Figure 2.5: Size dependence of the plasmonic near field in case of gold nanoparticles (Left) Experimental (Right) Theoretical prediction [37]

2.2.5. DISCRETE ENERGY STATES FORMED WITH THE DECREASE IN NANOPARTICLE SIZE

The size of the particle will have an effect on the energy distribution of the hot carriers produced by the decay of surface plasmon resonance. Manjavacas et al. [41] theoretically predicts the effect of nanoparticle size and the life time of the hot carriers on the number and energy distribution of the hot electrons produced in silver nanoparticles. Figure 2.6 shows the energy distribution and the number of hot electrons produced for silver nanoparticles for two different sizes. According to their predictions, nanoparticles of smaller diameter produced more energetic carriers and they attribute this to the density of electronic states of these systems. They point out that for systems with finite number of electrons, there will only be finite number of energy levels and hence have discrete density of states. Therefore, with a decrease in particle size, the energy levels will be more discrete and this allows for excitation of hot electrons of higher energies.

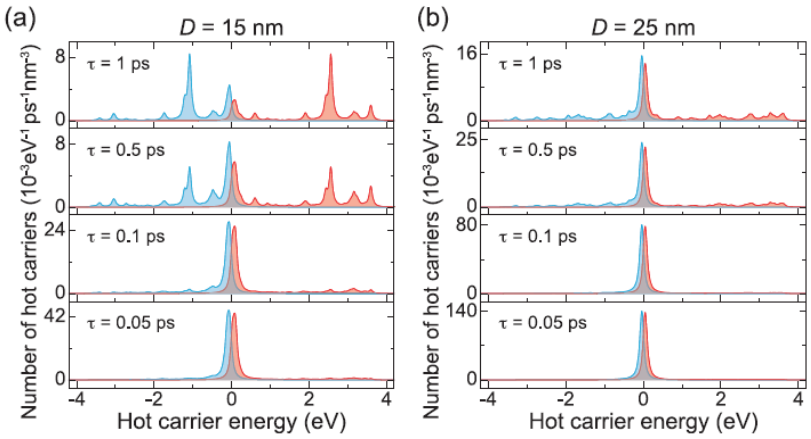

Figure 2.6: Distribution of energies of hot electrons (red) and holes (blue) with particle size and relaxation time in case of silver nanoparticles [37]

2.2.6. PLASMONIC HOT ELECTRON INJECTION

The decay of surface plasmon can happen broadly in two ways – radiative decay and non-radiative decay. The non-radiative decay process, the preferred mechanism for nanoparticles smaller than 25 nm, often results in the formation of electron – hole pairs which have energies much higher (for electrons) or much lower (for holes) than the fermi level of the metal. These high energy electrons are often called hot electrons, and have energies ranging from E_f to $E_f + \hbar\omega$. If these hot electrons can be efficiently extracted from these plasmonic nanoparticles, by preventing their recombination, they can be used for many applications [3, 12, 42]. One such application is the use in the field of photo-electrochemistry. It has been shown that, by depositing these plasmonic nanoparticles on the surface of the semiconductor photo-electrode the efficiency of the photo-electrochemical device can be enhanced [43]. If the hot electrons formed by the non-radiative plasmon decay have enough energy, it can be injected across the metal - semiconductor Schottky barrier, into the conduction band of the semiconductor. This injected hot electron is then sent to the counter electrode via an external circuit to drive chemical reactions. The charge neutrality in the metal nanoparticle is maintained by removing the hot holes by the coupled half reaction.

Plasmon induced hot electron injection was first reported by Zhao et al. [44] in 1996, when they reported anodic photo-current on visible light illumination of TiO_2 semiconductor containing gold or silver nanoparticles. Subsequently, many have demonstrated hot electron injection in different semiconductor materials and also with nanoparticles of different shapes. [45, 46] The parameters effecting the hot electron injection efficiency is not fully understood yet. Mubeen et al. [18] recently demonstrated a method wherein he used an extremely thin layer of TiO_2 semiconductor with nanoparticles on top to study the hot electron injection phenomena. This way they were able to ensure that the semiconductor had minimum influence on the resulting photo-current measurements, allowing them to independently study the effect of plasmonic hot electron injection.

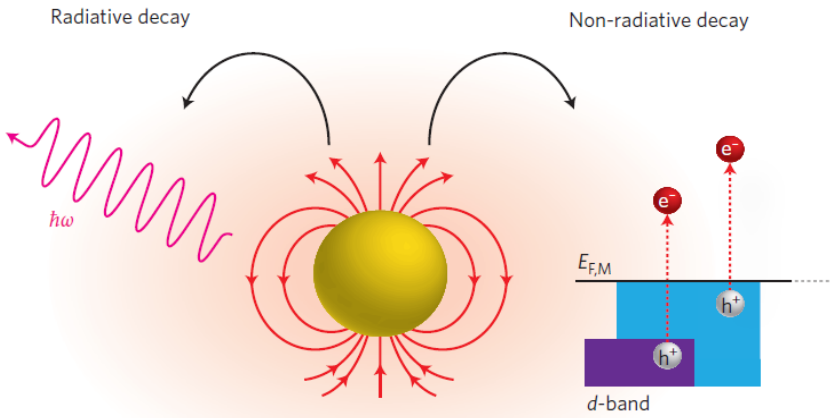

Figure 2.7: Plasmon resonance decay mechanism - radiative and non radiative decay [3]

METAL SEMICONDUCTOR SCHOTTKY JUNCTION

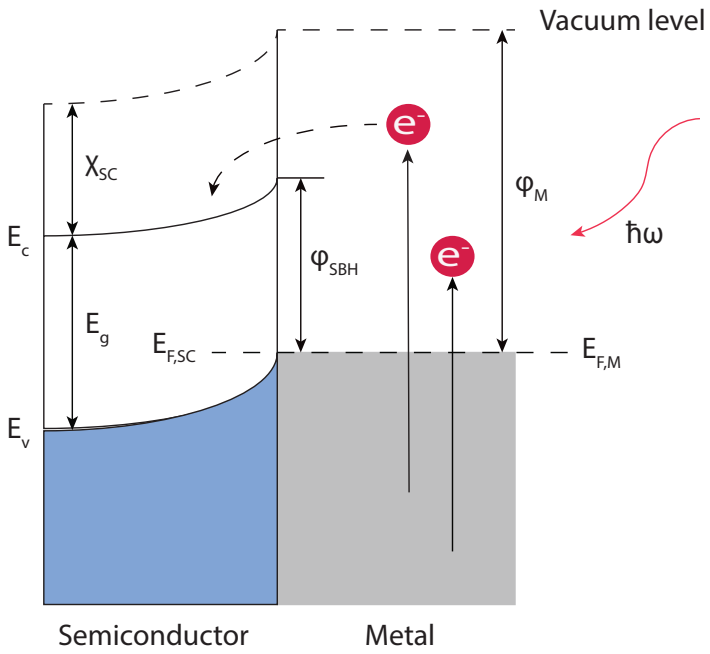

Figure 2.8: Schematic representation of plasmonic hot electron injection into a semiconductor

When a metal and semiconductor comes in contact, the interface between them can induce a depletion layer in the semiconductor. This results in a built-in potential called the “Schottky barrier” to appear between the bulk of the semiconductor and the surface. The magnitude of this potential is called “Schottky barrier height (SBH)”. For an n-type semiconductor – metal junction, this barrier height can be approximately estimated by the Schottky – Mott model [47],

$$SBH\ (eV) = \varphi_M - \chi_{SC} \tag{2.19}$$

where, φ_M is the work function of the metal and χ_{SC} is the electron affinity of the semiconductor. When the metal and semiconductor initially come in contact, the bands bend down in the direction of the side with lower work function (the semiconductor in this case). The electrons from the conduction band of the semiconductor, donated by dopants, jumps into the metal on initial contact and thus forms a depletion region near the interface - resulting in band bending. But in reality, the prediction by Schottky – Mott rule is not so

accurate because of interface surface states and defects. The hot electrons produced by the non-radiative decay of surface plasmons need to have energy greater than the SBH to get injected into the conduction band of the semiconductor. This implies that higher this barrier energy, lower is the hot electron injection efficiency.

INTERBAND AND INTRABAND TRANSITIONS IN METALS

When photons of sufficient energy are incident on a metal, the electrons in the crystal get excited into an unoccupied higher energy level. For these transitions, the total momentum must be conserved. If the electron transition is between two different bands, it is called an interband band transition. Interband transitions have a minimum energy threshold. [48] For silver, this threshold energy is 3.7 eV ($\approx 335nm$) meaning that there are no interband transitions, upon excitation with visible light. Whereas for gold, this interband threshold is at 2.3 eV ($\approx 539nm$).[43]

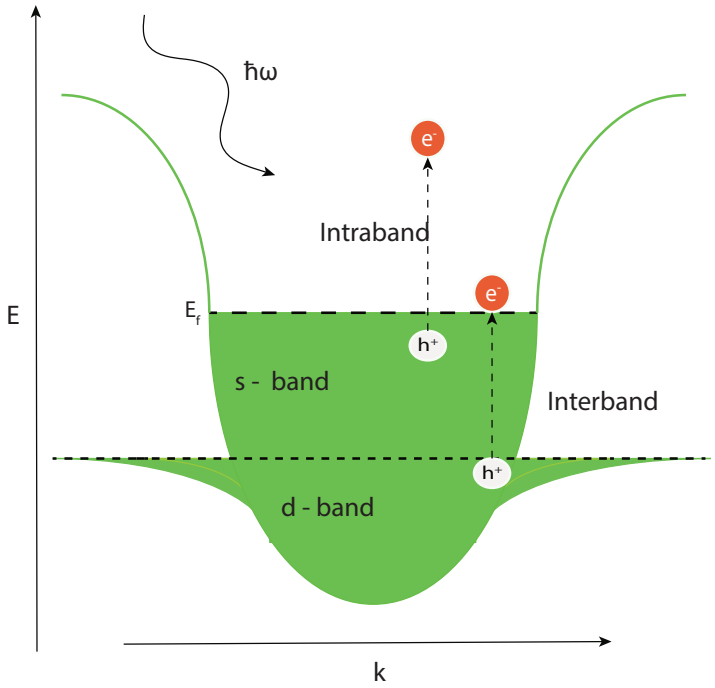

Figure 2.9: Schematic represetation of interband and intraband transitions in a metal

Under certain circumstances, the photons can excite an electron into an higher energy level with the same band. But such transitions occur in participation with a phonon (a lattice vibration quantum). This is because the incoming photon does not have enough momentum to excite electron to a higher energy level [48]. This additional momentum can be obtained from the phonons. These transitions are called intraband transitions. Figure 2.9 depicts the interband and intraband transition in a metal. Intraband transitions create hot electrons with a higher energy distribution compared to that of interband transitions. [49] Therefore, to create a higher energy hot electrons for an efficient hot electron injection process, intraband transitions are preferred.

FOWLER'S THEORY

Fowler [50] introduced a technique to measure the actual SBH in a metal – semiconductor interface using the photoemission technique, by exciting electrons from the fermi level in the metal to the conduction band of the semiconductor. The excitation is done using a monochromatic light source, where the photon energy ($h\nu$) is different for each wavelength of incoming light. The resultant photo-current is measured to determine the barrier height. A sharp increase in photo-current occurs when $h\nu >$ SBH and again when $h\nu > E_g$ of the semiconductor. From the first big increase in photo-current, we can obtain the SBH. The Absorbed Photon to Current conversion Efficiency (APCE) can be derived from the modified Fowler relation by [4, 51]:-

$$APCE = \frac{C_F(h\nu - E_{SB})^2}{h\nu} \tag{2.20}$$

where, C_F is the Fowler coefficient and E_{SB} is the Schottky barrier energy.

2.2.7. PLASMON INDUCED RESONANCE ENERGY TRANSFER

Plasmonics offers many ways than one to enhance the performance of photo-electrochemical devices. Though the focus of this thesis is on hot electron injection, which provides enhancement below the Optical Band Gap Edge of the semiconductor (OBGE), it is important to also consider other plasmonic effects that might play a role in the enhancement of performance these devices. This knowledge would help to isolate the hot electron injection effect and provide a better insight into its working. The other ways plasmonics can contribute to the enhancement is through light scattering, light concentration and Plasmon Induced Resonance Energy Transfer (PIRET) [4]. Of this, the light concentration and light scattering enhances the performance above the OBGE of the semiconductor and can be easily filtered out as we focus on below the OBGE enhancement through hot electron injection. The PIRET mechanism enhances the performance below the OBGE and requires a closer look.

In the PIRET mechanism, the concentrated energy from the localised surface plasmon resonance is transferred to the semiconductor. This is done via the near field of the nanoparticle, which penetrates into the semiconductor inducing charge separation in the semiconductor. Cushing et al. [52] studied this mechanism by using an insulating layer between the nanoparticle and the semiconductor, essentially preventing any hot electron injection into the semiconductor, allowing them to isolate the PIRET mechanism. Their studies showed enhancement both above and below the OBGE of the semiconductor. This could be one of the main factor that distinguishes the performance enhancement from the plasmon induced hot electron injection to that from the PIRET mechanism, as the performance enhancement from the hot electron injection is only below the OBGE.

2.2.8. DECAY OF SURFACE PLASMON RESONANCE

The surface plasmon decay mechanisms can be broadly classified into radiative decay and non-radiative decay mechanisms. The actual decay of the surface plasmon is an interplay between both these mechanisms depending on the ratio of absorption cross-section to the scattering cross-section of the nanoparticle.

RADIATIVE DECAY OF SURFACE PLASMON RESONANCE

Radiative decay is the dominant mechanism for particles with diameter > ~ 40 nm. [4] Through this mechanism the surface plasmon decays by emitting a photon. If the plasmonic nanoparticle is in a junction between two dielectrics, the emission is preferentially done into the medium with a higher refractive index. This is normally the case with semiconductor-metal-electrolyte junctions. Therefore, the plasmon will decay by emitting a photon back into the semiconductor (under back illumination), thereby increasing the path length of the light and thus improving the light absorption of the semiconductor.

NON-RADIATIVE DECAY OF SURFACE PLASMON RESONANCE

For particles smaller than ~ 40 nm, the non-radiative plasmon decay is the dominant mechanism. Through this mechanism, the plasmon will decay by exciting electron-hole pairs from within the plasmonic metal nanoparticle. For an electron to excited from one state to a higher energy state, the energy and momentum of this transition has to be conserved. Otherwise, such transitions are forbidden. This additional energy and momentum has to be obtained either from the incident photon directly or from some other source. This energy and momentum are conserved for these excitations in different ways, as discussed below -

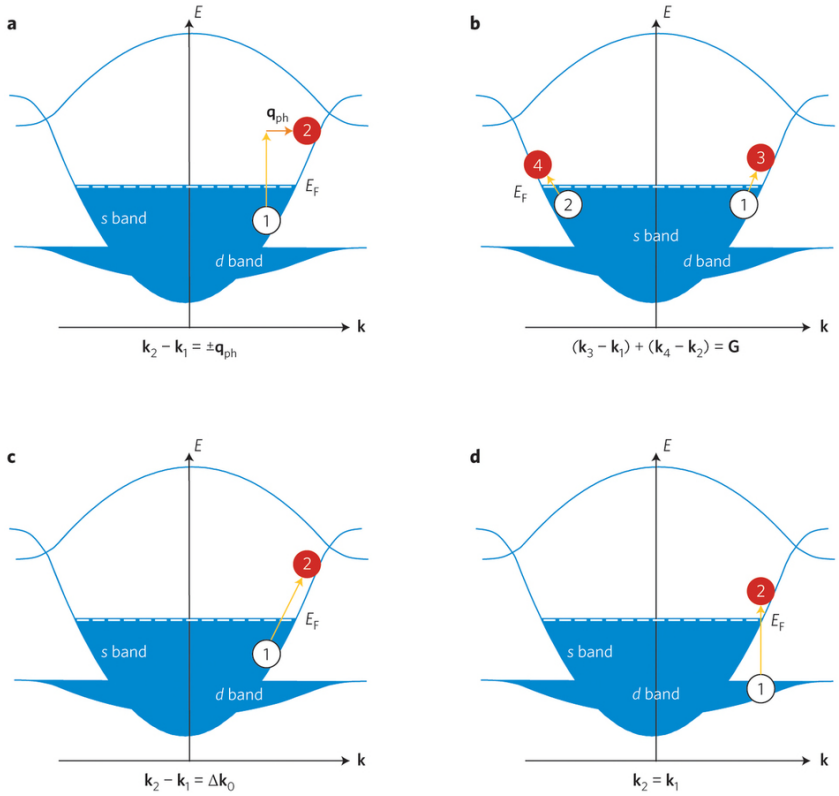

Figure 2.10: (a) Phonon-induced (or assisted) plasmon decay mechanism (b) Plasmon decay by exciting multiple electron-hole pairs in different direction and conserving momentum (c) Surface-induced plasmon decay mechanism (d) Plasmon decay by interband excitations [19]

Interband excitations

As discussed before, interband transitions occur from one band to another and has a minimum energy threshold. If the incoming photon has this minimum energy and momentum to make this transition, then the electrons can be directly excited to a higher energy state. This way the energy and momentum conservation criteria's are satisfied to make this transition. Depending on the metal under consideration, this minimum threshold energy and momentum required to make the interband transitions will change. No hot electrons are formed in such a transition as the electrons are only excited from a lower band until the vicinity of the fermi level of the metal. Though hot holes are formed in the d band, but it quickly recombines due to the high density of states of the d band. Figure 2.10 (d) shows this transition. Other forms of decay mechanisms are intraband mechanisms which occur within the s band as discussed before. In these forms of decay mechanisms, the incoming photon does not have enough momentum to excite the electron and hence requires an external source to transfer this additional momentum. These mechanisms are discussed in detail below.

Electron-electron scattering

Another possible mechanism of non-radiative plasmon decay is the electron-electron scattering mechanism. In this decay mechanism, the momentum is conserved by two electrons getting excited from the s band, in different directions. This form of decay mechanism is depicted in figure 2.10 (b). The photon energy is divided between 4 charge carriers (2 electron-hole pairs) and hence this process does not result in an hot electron.

Phonon-induced decay

The additional momentum required for the excited electrons to move to a higher energy state can also be obtained by collisions with a phonon. Phonons are lattice vibrations which have low energy, but high momentum. This is depicted in figure 2.10 (a). If the phonons can provide the additional momentum required, it creates a hot electron-hole pair which can be extracted.

Surface-induced decay

When oscillations of light is confined in really small nanoparticles, to sustain the oscillations, more electric field energy of light is stored in the form of kinetic energy of the oscillating plasmons. These fast oscillating plasmons will have the energy and momentum to excite an electron directly upon its decay. This mechanism will also result a hot electron-hole pair. This is shown in figure 2.10 (c).

3

METHODS AND EXPERIMENTS

3.1. TiO_2 SEMICONDUCTOR SYNTHESIS

The hot electron injection of the plasmonic nanoparticles were studied on 10 nm TiO_2 semiconductor films as mentioned earlier. The aim was to minimise the effect of the TiO_2 film on the overall performance of the device by decreasing its thickness, to independently study the plasmonic HEI. A brief procedure of the preparation of TiO_2 films is described below.

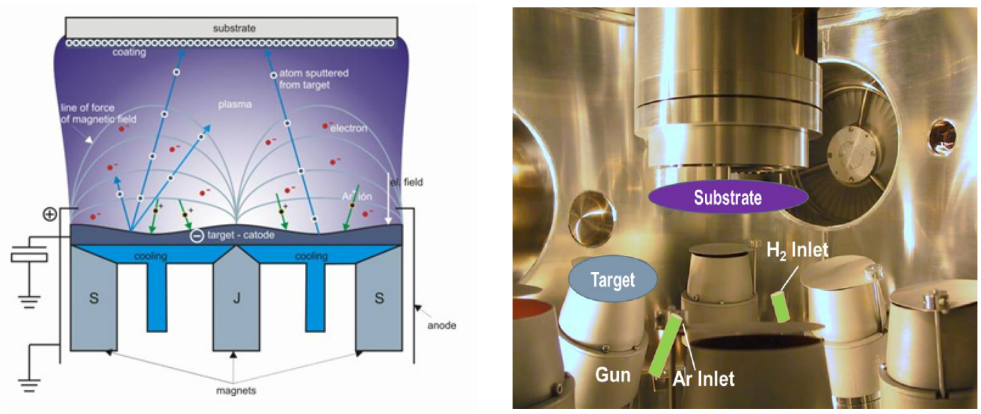

Figure 3.1: (Left) Schematic representation of magnetron sputtering [53] (Right) Inside of the magnetron sputtering vacuum chamber [54]

A 10 nm titanium layer was deposited on a Fluorine-doped Tin Oxide (FTO) substrates of size 20 mm x 15 mm(TEC-15, Hartford Glass Co.) using magnetron sputtering technique (ATC Orion sputtering system with a titanium target (>99.995 % purity)[1]. Briefly, a plasma is produced in the gas (argon is used in this case) between the two electrodes by applying high voltage. The ions thus formed in the chamber accelerates towards the cathode target, which is the titanium metal source. These ions knock out titanium atoms from the target which moves towards the substrate forming a thin film on it, because of Van der Vaal's forces and chemical bond formation. A magnetic field is applied to confine the ions and electrons near the target, making the process more efficient and self-sustaining [55]. The base pressure of the system was 2.10^{-7} mbar. Argon gas pressure was set at 3 µbar. Argon gas flowrate was maintained at 20 sccm and the deposition was done for 3.5 mins to produce 10 nm titanium films.

Prior to the deposition, the substrate was cleaned with laboratory soap and DM water (Milli-Q grade) followed

[1] Magnetron sputtering deposition of titanium was done by Ing. Herman Schreuders (MECS, TU Delft)

by cleaning using the ultrasonification cleaning technique using acetone and isopropanol for 20 mins each. The samples were further dried under compressed nitrogen gas flow. A small portion of the substrate was taped to expose the FTO layer after sputter deposition of titanium, for providing a conducting back contact in the PEC cell. The titanium coated substrate was annealed at 500 °C for 5 hours at a rate of 5 °C/min under a compressed air flow of 100 sccm. Annealing at these conditions produced an anatase type TiO_2, which is suitable for photo-electrochemistry applications.[56–58]

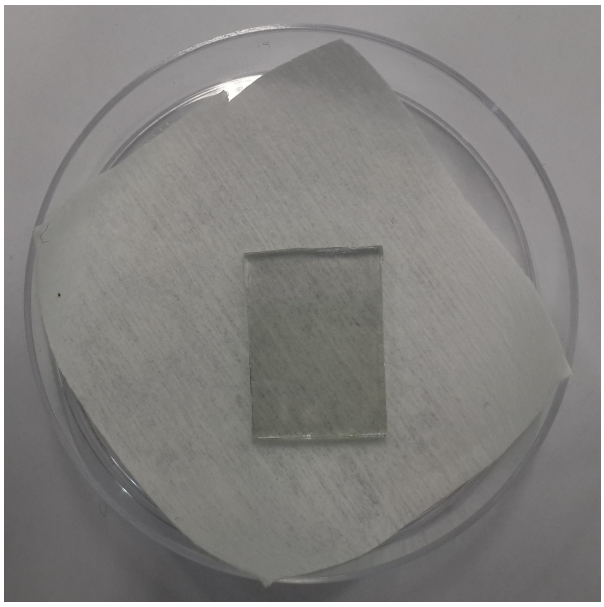

Figure 3.2: Picture of the annealed 10 nm TiO_2 on FTO sample used for this study

3.2. NANOPARTICLE SYNTHESIS

The nanoparticles used for this study were synthesised in the gas phase using the spark ablation technique [59–61]. A High Frequency Spark (HFS) generator was used for producing the silver nanoparticles and a low frequency spark generator was used for the gold and alloy nanoparticles. A spark generator consists of two face-aligned cylindrical electrodes separated by a very small gap (of the order of mm). These electrodes can either be of the same material to produce pure nanoparticles of the electrode material or can be of different materials to produce alloy nanoparticles of different compositions [62–64]. The electrodes could also be made of atomically mixed components at a specific composition to produce nanoparticles of that composition, as used in one part of this study. The setup also consists of a carrier gas inlet and exit nozzle which continuously flushes the gap between the electrodes with an inert/reacting gas, depending on the application. A high voltage is applied between the electrodes which induces a breakdown. This ionizes the gas between the electrode, creating a conducting plasma. This conducting plasma serves a channel to carry charges and hence induces a short current flow between the electrodes which creates a spark between the electrodes. The lifetime of this spark is of the order of few microseconds and results in local hotspots with temperatures of over 20000 K [65] which instantly evaporates the electrode material. The constant flushing of the carrier gas serves to quench the electrodes and vapour material as well as carry away this vapour away from the electrodes. The vapour quenching rates are of the order of 10^7-10^{10} K/s [62]. This sudden quenching results in the nucleation of these particles which later collides and grows into atomic clusters and then primary particles and aggregates and agglomerates, as depicted in the figure 3.3. This breakdown cycle is repeated at a constant frequency providing a continuous production of nanoparticles.

Two types of spark generators are used in this study – the low frequency spark and the high frequency spark. [60] The low frequency spark can be modelled like a resistor-inductor-capacitance spark (RLCS) circuit. Here the breakdown voltage of the gas determines the discharge voltage. The spark frequency can be adjusted by varying the capacitance and distance between the electrodes. This system has an upper frequency limit of about 500 Hz. The other system is the high frequency spark generator. Here the charging and discharging

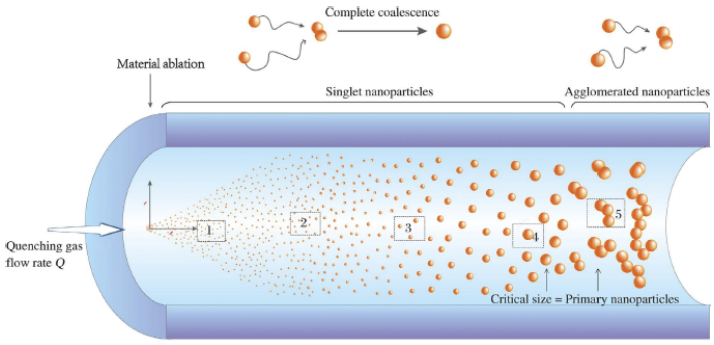

Figure 3.3: Schematic representation of nucleation and agglomeration of particles at the exit of the spark [66]

cycles are decoupled by using switches, and hence provides a better control over the sparking frequency. It also has a glowing circuit which prevents the plasma from completely extinguishing between each spark and hence a lower voltage is needed to induce the breakdown. The electrical circuit models of both spark generators are depicted in figure 3.4. [60]

These agglomerated nanoparticles are then sintered into spherical nanoparticles in a tube oven operating at temperatures above 900 °C. The nanoparticles are then size selected based on their electrical mobility, using a custom made short french type differential mobility analyser (DMA) by varying its voltage and flows [67]. An online condensation particle counter (CPC) was used to monitor the particle concentration at each instant coming from the DMA. These negatively charged nanoparticles are directly deposited from the gas phase, consisting of the size selected nanoparticles from the DMA, onto the TiO_2/FTO substrate using an in-house built electrostatic precipitator. The nanoparticle deposited TiO_2/FTO substrates were stored in sample boxes containing freshly regenerated silica gels to prevent nanoparticle degradation, by ensuring a dry local atmosphere. Schematic representation of the whole setup is shown in figure 3.5. Similar depositions of size selected nanoparticles were also made on a 200 mesh copper microgrids coated with foamvar/carbon (purchased from TED PELLA INC.) for characterisation by Transmission Electron Microscopy (TEM). An average nanoparticle size distribution was obtained (by analysing over 200 nanoparticles) after analysing these images using the imageJ software (Research services branch, National Institutes of Health).

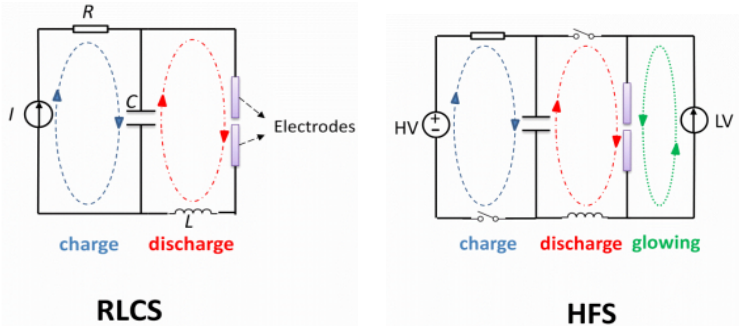

Figure 3.4: (Left) A RLCS circuit used in the low frequency spark (Right) A modified RLCS circuit consisting of fast electronic switches and a glowing circuit used in the high frequency spark [60]

Pure silver and gold electrodes (>99.95% purity, purchased from Goodfellow Cambridge Limited) was used in the study to synthesise pure silver and gold nanoparticles, respectively. The 50-50% gold-silver alloy nanoparticles were produced using atomically mixed electrodes of the same composition (>99.95% purity, purchased from Goodfellow Cambridge Limited). The spark frequencies and carrier gas flowrates were adjusted depending on the nanoparticle material, size and the type of spark generator used. The tube oven temperatures were also adjusted based on the nanoparticle material and size of the nanoparticle, to provide the optimum residence time and temperature for the nanoparticle agglomerates to form a perfect sphere. The operating conditions used for the reported samples are tabulated in Appendix B.

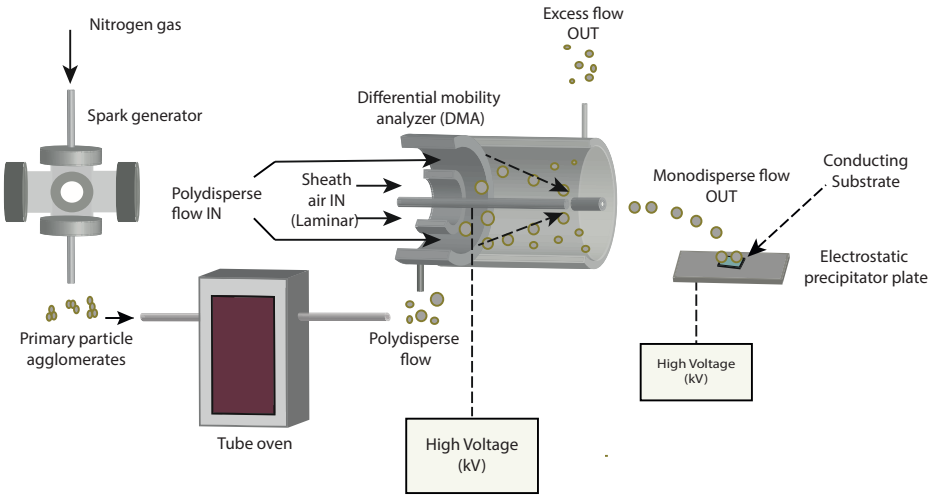

Figure 3.5: Schematic representation of the spark setup used for this study

3.3. UV-VIS ABSORPTION MEASUREMENTS

The UV-Vis absorption spectra of the NP's were obtained using a spectrometer (PerkinElmer – Lambda 900) equipped with an integrating sphere. The Lambda 900 contains a deuterium lamp to provide the UV spectra and a halogen lamp to provide the visible and near-infrared spectra for the spectroscopic measurements. The instrument automatically switches between these lamps. It is also equipped with a monochromator which helps to scan wavelengths individually. The system is equipped with two light detectors. One detector, called the photo multiplier (PMT), consists of a low work function metal and works based on the photoelectric effect. Each electron ejected by the incoming light, which has energy above the required threshold, is multiplied to produce a detectable current. The other detector is a low bandgap semiconductor (PbS) which can detect light which has energy greater than the band gap of this semiconductor [68]. The resultant current is already calibrated for providing the spectroscopic measurements. The PMT is used for wavelengths below 850 nm and the semiconductor for other wavelengths, upto the limit of the instrument.

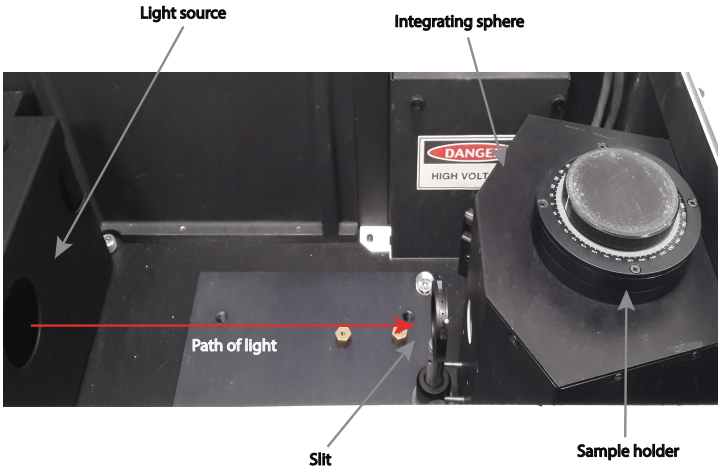

Figure 3.6: Inside of the PerkinElmer Lambda 900 UV-Vis spectrometer

$$\%\Delta A = \%T_{before\ deposition} - \%T_{after\ deposition} \tag{3.1}$$

The transmittance spectra of each TiO_2 sample was taken before the nanoparticle deposition and subtracted from the transmittance spectra of the sample after deposition to get the absorption spectra of the plasmonic

nanoparticles in percentage (% Δ A), as shown in the equation. All measurements were done inside the integrating sphere by front illumination with a slit of 4 mm diameter. The slit was used to focus the light on the nanoparticle deposited area of TiO_2. The samples are placed at a +10° angle from the path of light to minimise light reflection. The detectors within the integrating sphere measures the transmitted and reflected light and provides a spectra. In this report, it is called the "transmittance spectra (T)". The settings used for the Lambda 900 spectrometer are tabulated in 3.1.

Start Wavelength	600 nm
End Wavelength	300 nm
Ordinate Mode	%T
Integration time	0.2 sec
Scan speed	250 nm/min
Mode	Standard

Table 3.1: Settings used in the PerkinElmer - Lambda 900 UV-Vis spectrometer to get the light transmission measurements of the samples

3.4. PHOTO-ELECTROCHEMISTRY

3.4.1. PHOTO-ELECTROCHEMICAL CELL

To facilitate the photo-electrochemical (PEC) study on the photo-electrode under consideration, a PEC cell is used as a reservoir to hold the electrolyte and the electrodes. The PEC cell has an optically transparent glass window made of fused silica. Fused silica was preferred over normal glass because of its lower light cut-off wavelength (200 nm compared to 350 nm of normal glass). The nanoparticle deposited TiO_2 photo-anode is positioned to receive this light by front illumination. A detailed schematic of the in-house built PEC cell is shown in figure 3.7.

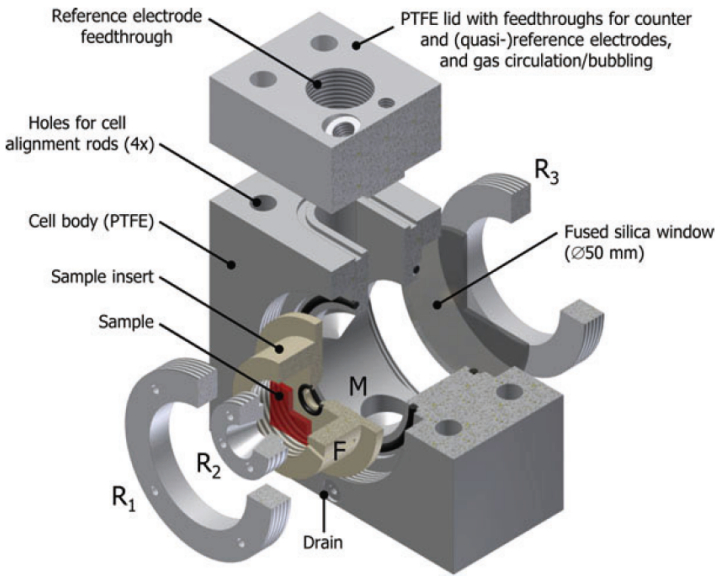

Figure 3.7: Schematic of the in-house built PEC cell used for this study [20]

A three electrode arrangement was used to perform this PEC study. An Ag/AgCl electrode (XR300, saturated KCl + AgCl solution (KS120), Radiometer Analytical) was used as the reference electrode and a platinum wire was used as the counter electrode. EG&G Par 283 potentiostat was used to fix the potential of the working electrode. A three-electrode arrangement was preferred over the otherwise used two-electrode arrangement in PEC studies to eliminate the current dependence of the voltage measurements. The electrolyte has a resistance and the overpotential developed at the electrode/electrolyte interface depends on the current flowing

through this interface. A third electrode (here the Ag/AgCl electrode) helps to break this dependence by acting as a reference by only allowing negligible current to flow through it, ensuring less fluctuations. This way a constant potential can be maintained at the working electrode during the experiments. The PEC cell was designed such that the distance between the working electrode and the reference electrode was kept minimal to decrease the ohmic voltage losses. Platinum was preferred as the counter electrode material, because of its high activity and fast kinetics in hydrogen evolution reactions. This would ensure that it will not act as a limiting factor in the study and would help to independently study the plasmonic hot electron injection.

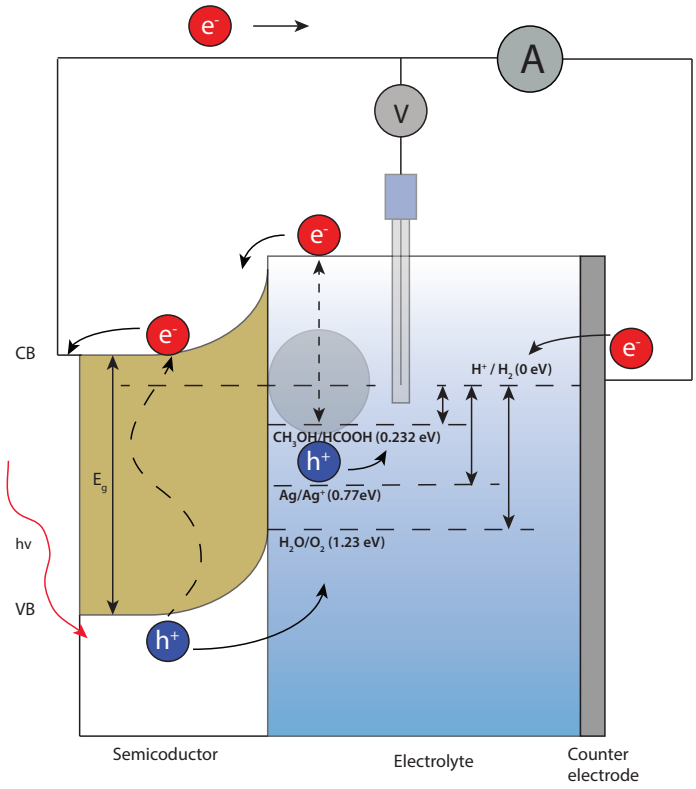

Figure 3.8: Schematic of the working of the PEC cell. Methanol oxidation is preferred over other reactions due to its favourable thermodynamics (Reduction potentials is E^0 vs SHE scale)

A combination of methanol (>99.9% purity, Sigma Aldrich) and 0.1 M phosphate buffer (pH 7), 50% v/v, was used as the electrolyte for the study. Local fluctuations in the pH of the electrolyte, during the course of the experiments, could have an effect on the flat band potential. The buffer solution ensured that the pH fluctuations in the electrolyte are minimal [20]. Methanol was used in the study as a "hole scavenger". This is because of the favourable oxidation potential of the methanol oxidation reaction compared to the water oxidation reaction. This would allow for the easy removal of the holes produced at the photo-anode. This ensures that the hole removal is not a limiting factor, allowing to focus on the plasmon induced hot electron injection of the metal nanoparticles. The possibility of self-oxidation of the silver nanoparticle in the reaction conditions was another reason that led to the choice of methanol as a hole scavenger. A simple schematic representation of the energies required for the oxidation reactions with respect to the hydrogen evolution reaction is shown in figure 3.8. From this, it is clear that the methanol oxidation is thermodynamically more favourable compared to the other two oxidation reactions. Methanol concentration in the electrolyte is ensured to be in excess to prevent this reaction from being kinetically limited. The electrolyte was mixed thoroughly by purging with nitrogen gas at high flowrates. Nitrogen gas was also purged inside the PEC cell during the experiments at 90 sccm. Care was taken to ensure that the nitrogen bubbling was not obstructing the path of the light. The set potential of the working electrode was obtained from the measurements in V vs Ag/AgCl units. This is converted to the often used reversible hydrogen electrode (RHE) scale by using the below formula, where V_{RHE} is the potential in the RHE scale, $V_{Ag/AgCl}$ is the measured potential from the experiments with respect to the Ag/AgCl reference electrode and $V^0_{Ag/AgCl}$ is the standard potential of the Ag/AgCl electrode used with respect to the standard hydrogen electrode (SHE) scale.

$$V_{RHE} = V_{Ag/AgCl} + V^{0}_{Ag/AgCl} + 0.059 * pH \tag{3.2}$$

3.4.2. EFFICIENCY MEASUREMENTS

INCIDENT PHOTON TO CURRENT CONVERSION EFFICIENCY

To understand the practical limitations or performance enhancement factors of a PEC device/material, techniques are required to assess its working. This way, we can hopefully address these issues through optimised engineering. Here, the response of the PEC device to the incoming light is to be studied to better understand the enhancement in the performance of the PEC device due to plasmonic hot electron injection. Solar radiations are a mixture of light of different wavelengths. The PEC device and the plasmonic nanoparticles responds differently to each wavelength of incoming light. Therefore, it is important to study the quantum efficiency as a function of wavelength to understand the contribution of plasmonic hot electron injection to the performance of the PEC device. The Incident Photon to Current Conversion Efficiency (IPCE) technique allows us to study this wavelength dependent response of the PEC device. This technique is also referred to as the External Quantum Efficiency (EQE) technique. It calculates the fraction of incoming photons that gets converted to an extractable electron, measured by outer circuit. [20, 22]

$$IPCE(\lambda_i) = \frac{electron\ \ flux}{photon\ \ flux} = \frac{hc}{e}\frac{j_{photon}(\lambda_i)}{\lambda(i)P(\lambda_i)} \tag{3.3}$$

where, h is the planck's constant (m^2kg/s), c is the speed of light (m/s), e is the charge of an electron (C), $\lambda(i)$ is the i^{th} wavelength (m), $j_{photon}(\lambda_i)$ is the photocurrent density at each λ (A/m^2) and $P(\lambda_i)$ is the power density at each λ (W/m^2).To make proper IPCE measurements, a setup consisting of a lamp, a programmable monochromator and shutter, an optical diode and a potentiostat is required. A schematic illustration of the IPCE setup is shown in figure 3.9. A 200 W quartz tungsten – halogen lamp coupled with a grating monochromator – shutter setup was used to illuminate the sample in 6 nm steps [69] to obtain the photocurrent. An optical filter with a cutoff wavelength of 395 nm was used to minimize the effect of any secondary wavelengths from the monochromator, by blocking the light below 395 nm, i.e., blocking the light to the TiO_2 semiconductor. This also facilitated the independent study of the plasmonic hot electron injection.

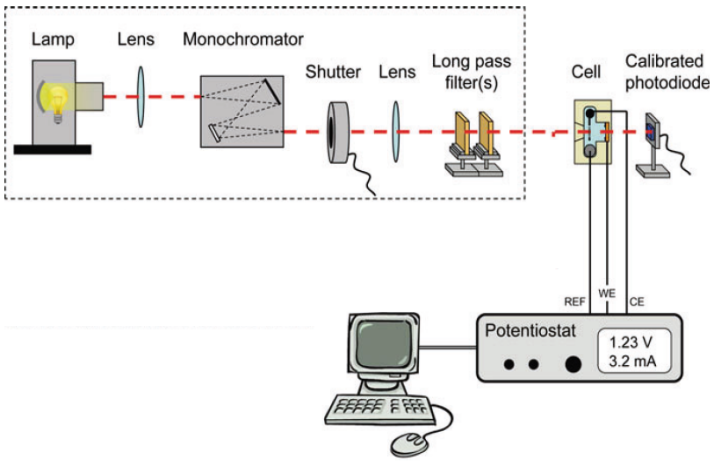

Figure 3.9: A schematic of the IPCE setup used in this study (Adapted from reference [20])

ABSORBED PHOTON TO CURRENT CONVERSION EFFICIENCY

IPCE measurements assumes that all the photons incident on the surface of the electrode is getting absorbed by the material and gets converted into a usable electron. This is useful to get an idea of the maximum current

that can be extracted from a particular photon source. The IPCE values are normally used to compare the performance of different devices. But in practice, all the photons incident on the surface of the photo-electrode does not get absorbed. Some photons might get reflected by the surface and some might be unabsorbed and hence get transmitted through the sample. Therefore, it is useful to normalize the IPCE values by the absorption spectrum of the light absorbing material under consideration. This would give us more insight into the performance effecting parameters within the system. The APCE value takes into consideration efficiencies of three fundamental processes involved – fraction of electrons or holes generated per photon absorbed, the efficiency of electron/hole transfer within the metal to reach the metal – semiconductor/metal - electrolyte interface, respectively, and the injection efficiency with an assumption that the counter electrode does not limit the current flow through the circuit. [70]

3.4.3. CURRENT - VOLTAGE RELATIONSHIP STUDY

A cyclic voltammetry study was performed to understand the current-voltage relationship of the photo-current produced by the plasmonic HEI. In this experiment the potential is ramped up linearly to a particular value and then ramped back to the starting point. The concept is to continually oxidize and reduce the semiconductor surface by cycling this potential. By changing the applied potential, the width of the space charge layer is altered. This would result in increased electron hole separation or increased recombination depending on the band bending resulted from the applied potential. At extreme potentials, the semiconductor surface can get oxidized. In this study, the normal procedure was adapted to prevent the oxidation of the metal nanoparticles. Therefore, a smaller range of potentials, within the oxidation and reduction limits, were used to cycle. A monochromatic light source with a wavelength close to the plasmon resonance frequency of the nanoparticle under consideration was used instead of the normally used AM 1.5 solar simulator light source. This was done to specifically focus on the contribution of photo-current due to plasmonic HEI by minimising the current contribution for TiO_2.

4

RESULTS

As mentioned in chapter 1, the goal of this thesis is to understand the fundamental factors effecting the plasmonic hot electron injection. In this chapter, some of the important results from this research is presented. The whole section is subdivided into three parts. In the first part, the results relating to the tuning of the surface plasmon resonance and its effect on the hot electron injection and its efficiency is discussed. In the second section, the results relating to the size dependence of the of hot electron injection efficiency will be looked into. In the final section, the results related to the effect of nanoparticle concentration, at the substrate surface, on the hot electron injection efficiency will be presented. Each of the above mentioned section would begin with the results from the characterisation tests performed, followed by the results from the photo-electrochemical testing. A detailed discussion of these results is left for next chapter.

4.1. TUNING OF HEI BY VARYING THE NANOPARTICLE COMPOSITION

Plasmon induced hot electron injection provides a direct enhancement in the performance of the PEC device, i.e., it does not depend on the performance of the semiconductor used as the photoanode. The most important fact is that, this technique provides performance enhancement below the OBGE of the semiconductor. If the plasmon induced HEI were active above the OBGE of the semiconductor; light to the semiconductor would essentially be screened, which is detrimental for the performance of the PEC device. But for this technique to be universal for all kinds of semiconductor photoelectrodes, it is important to have a large array of these plasmonic nanoparticles that are active at different wavelengths. This would allow to handpick them based on the OBGE of the semiconductor under consideration. At present we are limited to just gold, silver and copper nanoparticles that are active in the visible region of light (400 nm, 520 nm and 560 nm respectively). Long back, El-Sayed et al. [38] demonstrated that the surface plasmon resonance of the nanoparticles can be tuned by alloying two different plasmonically active materials. This way, the surface plasmon resonance can essentially be tuned over the entire visible spectrum by choosing the right materials. The impact of this tuning, by alloying two plasmonically active materials, on the HEI efficiency has not been investigated before. More importantly, such a study would throw more light into the fundamental principles behind the HEI and the factors effecting the energy distribution of the excited hot electrons. This study was performed as part of this master thesis and in this section, the most important results from this study will be discussed.[1]

[1] Some results from this work are published in [43]

4.1.1. CHARACTERISATION

TEM ANALYSIS

The comparison in the performance efficiency of the silver, gold and the alloy samples were done for the particles of the same size range. This would ensure that any difference in performance is solely down to the inherent property of the material and not due to any geometric effects because of the difference in sizes. A DMA was used to size select the nanoparticles from the aerosol produced from the spark generator, as explained in section 3.2. Same voltage and flow conditions were maintained in the DMA each time to size select the same distribution of the particles. To confirm the size ranges of the particles used, a Transmission Electron Microscopy (TEM) analysis was performed for all three samples. As evident from the TEM micrograph images analysed in figure 4.1, the distributions are nearly monodisperse and is of the same size, as required for the comparison. Some particle agglomerates with the same electrical mobility as that of the size selected nanoparticles is also deposited on the samples. Operating conditions have been controlled to minimise the formation and selection of these agglomerates, but a complete elimination of agglomeration was found to be difficult with the current procedure. The results presented here are from an initial analysis where lower sizes were used. The particle size was later changed to 16 nm (for all three samples) and also lower flow rates were used to increase the residence time in the oven to reduce particle agglomeration. New TEM depositions were made to confirm this, but these samples could not be analysed as the TEM was out of service. Since the same DMA voltage and similar flow conditions were used in each case, same particle size distribution is expected as the initial case shown in 4.1. The gold nanoparticles were found to form higher amount of agglomerates, owing to the high sintering tendency of gold.

UV-VIS ABSORPTION SPECTROMETRY

A main characteristic of plasmonic nanoparticles is their extinction peaks at their respective plasmon resonance frequencies. These extinction peaks contain a lot of information within them. An expert can predict the approximate size, shape and composition of these nanoparticles just by looking at their extinction spectrum. In this subsection, a comparison between the absorption curves of silver, gold and 50% silver – 50% gold alloy nanoparticles is considered. The absorption curves plotted here are of the plasmonic nanoparticles alone, obtained by subtracting the background as discussed in section 3.3. As gathered from the TEM analysis above, all the nanoparticles used for this comparison have similar size distributions and shape. Figure 4.2 shows three distinct absorption curves. From this plot, it can be seen that the plasmon resonance wavelength of pure silver nanoparticles is at ~ 405 nm and for pure gold nanoparticles is at ~ 518 nm, close to the predictions from mie theory. An exact match cannot be made to Mie theory owing to the anisotropic dielectric environment (air-metal-semiconductor). The plasmon resonance frequency of the alloy nanoparticle is at ~ 442 nm. This value is in between the plasmon resonance frequencies of the pure silver and pure gold nanoparticles, as expected. Phase diagram of silver and gold suggests that the components form a homogeneous mixture. [71] The use of atomically mixed electrodes also ensures that a perfect alloy is obtained. The marginally varied levels of absorption peaks for all three samples can be attributed to the difference in concentration of nanoparticles on the surface of the analysed substrates. One other characteristic of the silver nanoparticle curve and alloy nanoparticle curve, that should be noted, is the second peak at ~ 530 nm and ~ 555 nm respectively. This is attributed to the dimer interactions of these nanoparticles at the substrate surface. This concept is widely discussed in literature [72, 73]. The dimer interactions for silver nanoparticles will be revisited in detail in the results section of the third set of experiments of this report. For the gold nanoparticle absorption curve, an increase in absorption is visible below ~ 480 nm. This is attributed to the light absorption due to the interband transitions within the gold nanoparticles, because of the low interband energy threshold of gold (see section 2.2.6). A more detailed discussion on the shift of plasmonic resonance frequency with alloying is done in the Chapter 5.

XPS ANALYSIS

To get a better understanding on what happens by alloying gold and silver and why the plasmonic resonance shifted with alloying, an X-Ray Photoelectron Spectroscopy (XPS) was performed on these nanoparticles. The XPS analysis was performed to study the valance band (d-band) of the alloy with gold and silver as the benchmark. The XPS results were normalised to make the comparison easier. As seen in figure 4.3, there has indeed

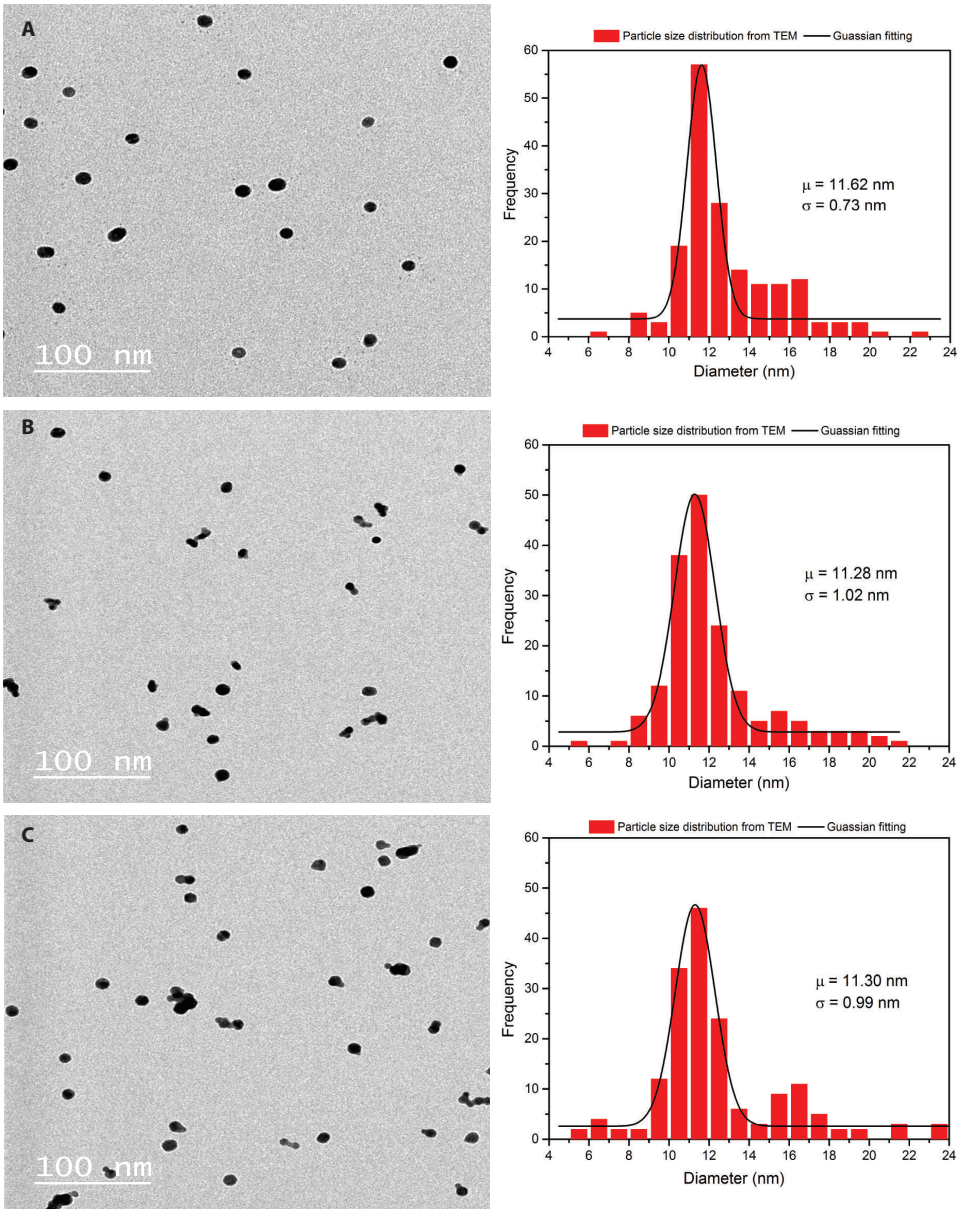

Figure 4.1: (A) TEM image and the particle size distribution for silver nanoparticles (B) TEM image and the particle size distribution for alloy nanoparticles (C) TEM image and particle size distribution for gold nanoparticles. Please note :- This is from an initial result. These TEM results are not of the same size as of the particles studied in this section. New TEM depositions of the actual particle sizes were made, but was not analysed as TEM was out of service.

been a shift in the d-band DOS centre, compared to gold and silver measurements, with alloying. This implies that the alloying has altered the electron density of the valence band and this might have resulted in the shift of the plasmon resonance wavelength for the alloy compared to gold and silver nanoparticles.

4.1.2. PHOTOELECTROCHEMICAL TESTING

INCIDENT PHOTON TO CURRENT CONVERSION EFFICIENCY (IPCE)

As discussed in section 3.4.2, the IPCE measurements offer a method to study the wavelength dependent response of these plasmonic nanoparticles, which is crucial for understanding the fundamentals behind the plasmonic hot electron injection of metal nanoparticles. Figure 4.4, shows the wavelength dependent IPCE plots for the silver, gold and alloy nanoparticles deposited on 10 nm TiO_2 samples. The details of the power

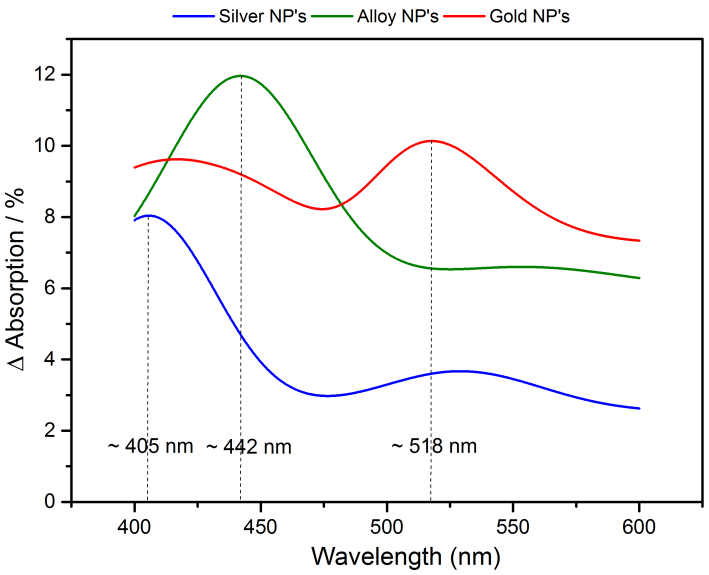

Figure 4.2: Absorption plots of plasmonic nanoparticles obtained using UV-Vis spectroscopy by subtracting off the influence of the semiconductor, as described in section 3.3

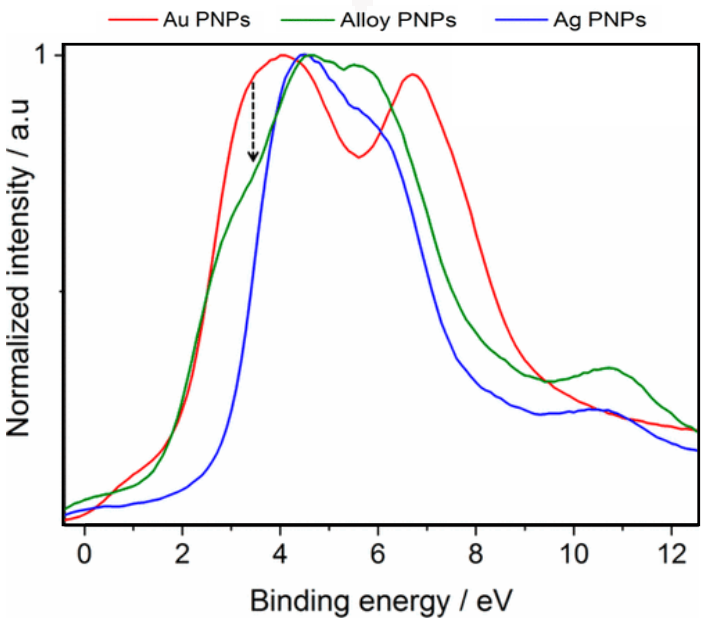

Figure 4.3: Normalised XPS plots of the valence band of silver, gold and alloy nanoparticles

calibration are mentioned in Appendix D. On careful observation, an increase in performance of the three nanoparticle deposited samples can be noticed (less so for the gold nanoparticles) compared to that of the bare TiO_2 sample. Another striking point to notice is that the enhancement is outside the bandgap of the TiO_2 semiconductor which is at < 400 nm. Therefore, this enhancement in performance is not something that is inherent to the semiconductor but can be attributed to the nanoparticles deposited on top of the semiconductor. If the performance enhancement was more of a catalytic or charge transfer contribution of the nanoparticles, the enhancement would not be wavelength dependent as is the case here. Therefore, the enhancement in performance here is clearly a plasmonic enhancement.

The IPCE enhancement of alloy and gold nanoparticles deposited devices are low compared to the silver nanoparticles. A zoomed in image, shown at the bottom of the figure 4.4, of this part of the graph clearly shows that the performance enhancement of the alloy nanoparticles is better compared to that of the gold

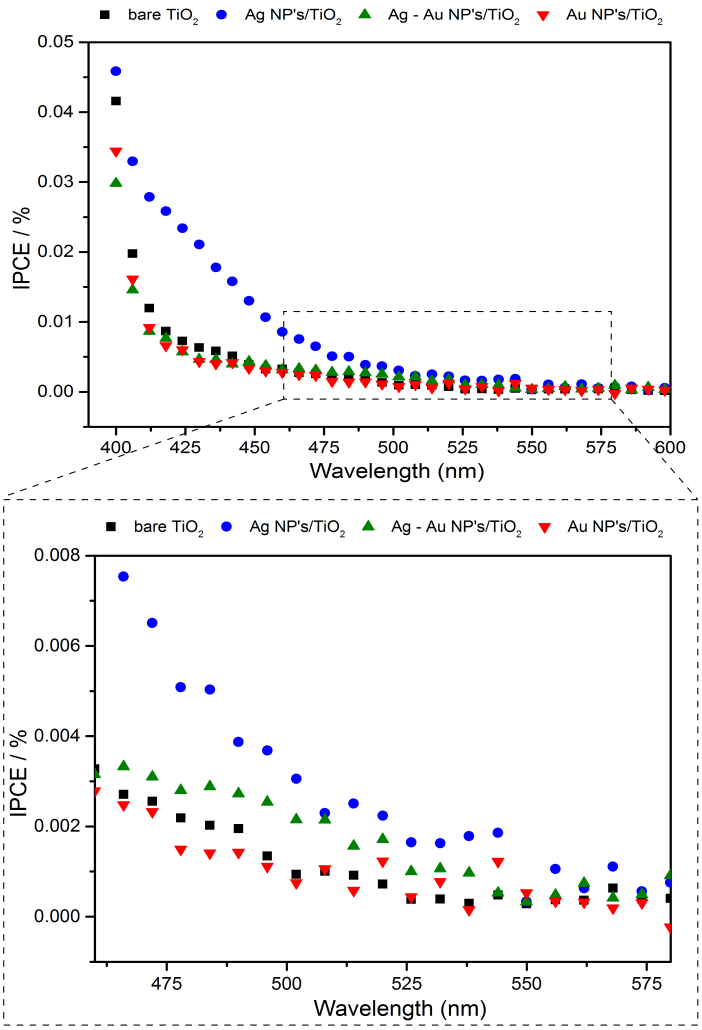

Figure 4.4: IPCE measurements of 15 nm silver, gold and alloy nanoparticles on TiO_2 semiconductor compared to bare TiO_2 semiconductor upon front illumination at a potential of 0.56 V vs RHE

nanoparticles on TiO_2. Figure 4.5 shows the enhancement in performance of these samples due to the contribution of these plasmonic nanoparticles alone, obtained by subtracting off the IPCE performance of the bare TiO_2 sample. A clear peak corresponding to the plasmonic resonance peak is visible for silver at ~ 420 nm. A small bump in the alloy curve could be noticed around ~ 480 nm and an even smaller bump for gold curve at ~ 540 nm. The peaks and bumps in enhancement, outside the bandgap of the semiconductor, confirms that the enhancement is a plasmonic contribution. These peaks and bumps are however shifted by ~ 20 - 40 nm compared to that of the plasmonic peaks obtained by absorption measurements (see figure 3.3). This shift could be attributed to the change in refractive index of the environment as the absorption measurements are done in air and the IPCE measurements are done in the electrolyte environment. This shift in plasmonic resonance frequencies with the surrounding environment is explained in section 2.2.3.

Since the plasmonic enhancement is below the OBGE of the TiO_2 semiconductor, the plasmon induced resonance energy transfer (PIRET) or the plasmon induced hot electron injection (HEI) phenomena's could be playing a role. But if the enhancement was due to the PIRET mechanism, an enhancement in IPCE would be visible both above and below the OBGE of the semiconductor [4, 52]. This enhancement would be proportional to both the surface plasmon resonance curve below the OBGE and the TiO_2 absorption states, which increases with wavelength above the OBGE. But in this case, the enhancement in IPCE is only seen to be proportional to absorption peak due to surface plasmon resonance and there is no enhancement above the OBGE, as seen in figure 4.6. The decrease in performance above the OBGE seen here could be due to the screening of light to the semiconductor. Moreover, works on PIRET mechanism reported in literature [52, 74]

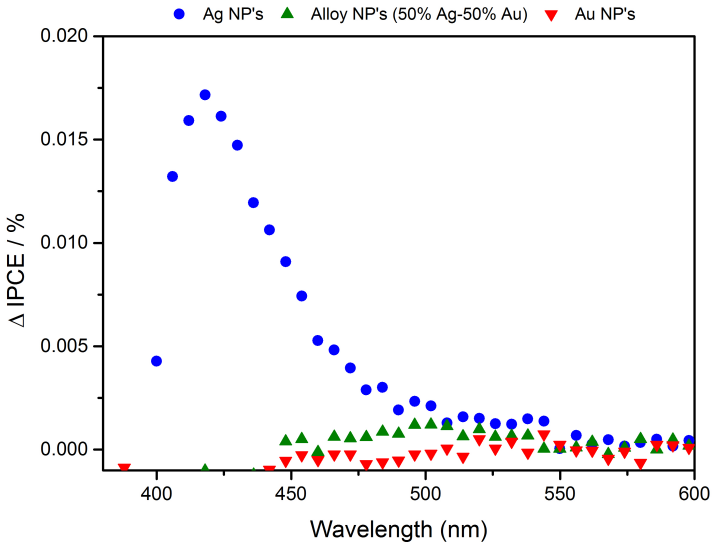

Figure 4.5: Enhancement in IPCE due to the contribution of plasmonic nanoparticles obtained by subtracting off the contribution of bare TiO_2

are mainly with semiconductor encapsulated nanoparticles and not for the configurations used in this study. Therefore, it can be concluded that the enhancement in performance of the nanoparticle deposited devices are due to HEI.

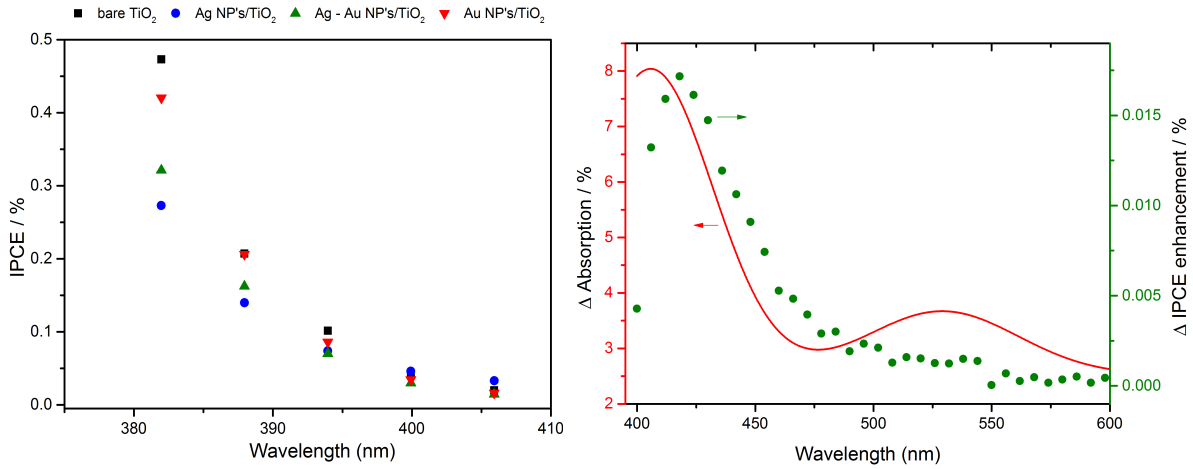

Figure 4.6: (Left) Decrease in IPCE above OBGE due to screening of light by plasmonic nanoparticles (Right) Correlation of the IPCE enhancement, due to silver nanoparticles, to its plasmonic resonance peak obtained from UV-Vis spectroscopy

CYCLIC VOLTAMMETRY

The current – voltage response of the plasmonic nanoparticle deposited TiO_2 photoanodes, compared to that of bare TiO_2 photoanodes, was studied using the cyclic voltammetry tests. These tests were performed under monochromatic light rather than the usual method of using solar simulators. This is was done particularly to look at the impact of plasmonic hot electron injection on the performance of photo-anodes at different applied potentials. The photo-currents from the plasmonic nanoparticles are very small compared to that of TiO_2 semiconductor. Therefore, using a solar simulator would only show currents from TiO_2 semiconductor as the hot electron injection contribution to the overall photocurrent is negligible. This makes it difficult to study the impact of plasmonic HEI with applied potentials and hence a monochromatic light source close to the plasmon resonance frequency was used.

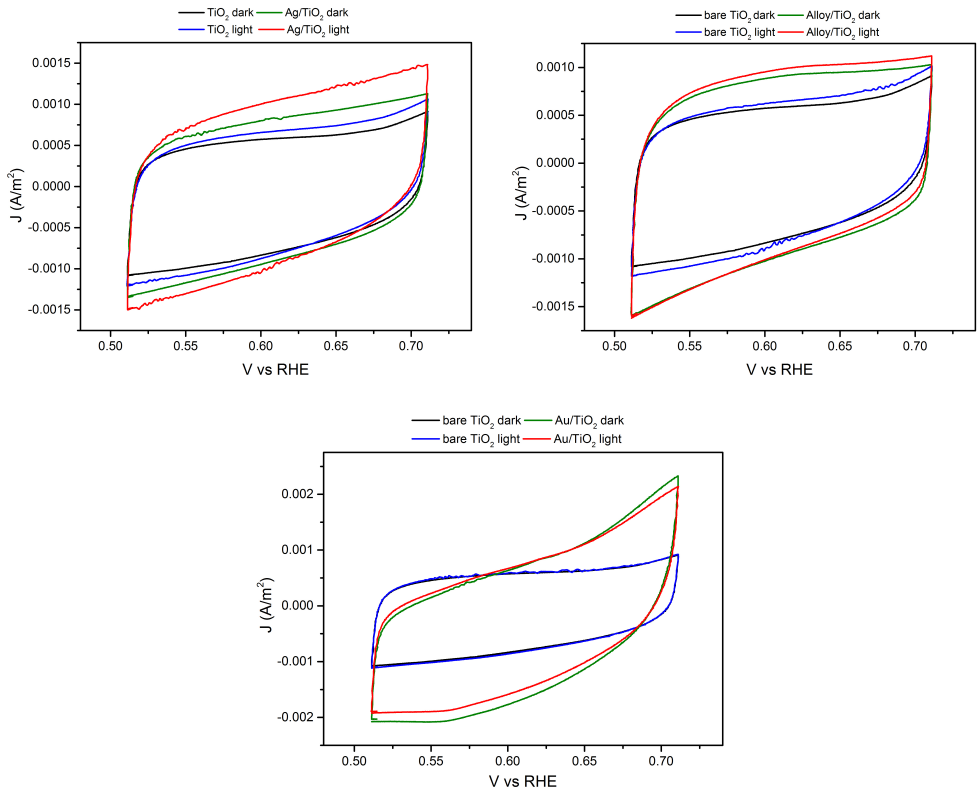

Figure 4.7: (Top left) J-V curves of silver-TiO_2 samples under dark and light illumination compared to that of bare TiO_2 (Top right) J-V curves of alloy-TiO_2 samples under dark and light illumination compared to that of bare TiO_2 (Bottom) J-V curves of gold-TiO_2 samples under dark and light illumination compared to that of bare TiO_2

For silver nanoparticle deposited devices, a monochromatic light of 430 nm was used which is close to the plasmonic resonance of silver nanoparticles in the electrolyte environment. Similarly, a monochromatic light of 470 nm and 540 nm was used for alloy and gold nanoparticles deposited devices respectively. The cycling was done between a small range of potentials (0.51 V vs RHE to 0.71 V vs RHE). This small range was chosen mainly because at higher positive potentials, the silver nanoparticles gets oxidised and goes into the solution as Ag^+ ions. Since the amount of silver nanoparticles used for this study is really small, this dissolution had a big impact. This oxidation of silver was observed in the preliminary experiments wherein a wider range of potentials were used for cycling. An oxidation peak was observed in the first cycle, but no reduction peaks were visible. The oxidation peaks were not visible with further cycling, confirming that the silver was removed from the semiconductor surface. Figure 4.8, shows one of the preliminary results of this potential cycling on silver nanoparticle deposited TiO_2 sample. Therefore, a shorter range of potentials were used for further cycling experiments as mentioned above.

Figure 4.7 shows the results from the third cycle for three nanoparticle deposited samples. For silver nanoparticle deposited sample (top left), a clear increase in the current density under illumination is visible compared to bare TiO_2 under illumination. But the dark measurement of the nanoparticle deposited sample suggests that the increase in current density is not completely the contribution of the plasmonic HEI. The nanoparticles also improves the catalytic properties and the charge transfer characteristics of the semiconductor. But a clear distinction between the light and dark measurements for the nanoparticle deposited sample suggests that HEI does contribute to the increase in photocurrent measurements compared to that of bare TiO_2 samples. A similar trend is also visible, with lesser contribution to enhancement by HEI, for the alloy nanoparticle deposited samples in Figure 4.7 (top right). This result is in accordance with the IPCE results where silver nanoparticles had a higher HEI enhancement. Figure 4.7 suggests that (bottom) there is no photo-current enhancement due to HEI for gold nanoparticle deposited samples. This is again in accordance with the IPCE results for gold deposited samples which showed no improvement in photo-current compared to that of bare TiO_2 samples. The response of gold under illumination is worse compared to the dark measurements. It is

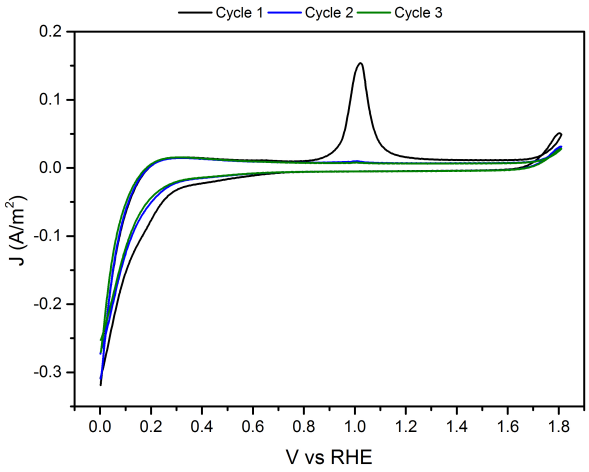

Figure 4.8: Cyclic voltammetry measurement (dark) from preliminary experiments, where the cycling was done for longer potential ranges. Decrease in oxidation peak with each cycle is clearly visible. Also not that the reduction peak for silver is also not visible

difficult to explain why this is so. Maybe few more experiments might be required to check and explain this behaviour, but is out of the scope of this thesis.

STABILITY TEST

Stability of the deposited nanoparticles is an important factor for their eventual application. Silver nanoparticles were found to degrade when exposed to humidity. This degradation was observed in the initial samples. The silver nanoparticles undergo oxidative dissolution, forming Ag^+ ions and migrating out of the nanoparticle, when it comes in contact with moisture and oxygen [75]. Figure 4.9 (top left and right) shows new nanoparticle islands formed adjacent to the parent silver nanoparticle due to oxidative dissolution on exposure to moisture in air. This degradation in further samples was avoided by storing it in silica gel (moisture traps) containers. Figure 4.9 (bottom) shows that the silver degradation was indeed avoided by this procedure. Such degradation was not visible in gold and alloy nanoparticles, when exposed to humid air, implying alloying makes the nanoparticles more stable.

The stability of the samples in the electrolyte solution was also tested. Chronoamperometry test was performed to test the stability of the sample by measuring the photocurrent with time. The electrolyte was always purged with nitrogen gas at high flowrates to remove any dissolved gases. Figure 4.10 shows that the photocurrent generation is stable over time implying that silver nanoparticles are stable in the electrolyte environment. Figure 4.10 also shows the stable photo-current generation due to HEI with time at 430 nm.

4.2. DEPENDENCE OF THE HEI EFFICIENCY ON THE NANOPARTICLE SIZE

As explained in sections 2.2.3, the plasmon resonance frequency can be tuned by varying the size of the nanoparticle. The decay mechanism of the surface plasmon resonance also depends on the size of the nanoparticle. These decay mechanisms of surface plasmon resonance were explained in section 2.2.8. As mentioned earlier, for particles of size less than ~ 25 nm, the non – radiative decay mechanisms of surface plasmon resonance dominates. At each nanoparticle size, below this ~ 25 nm limit, there is a interplay between different non – radiative decay mechanisms. This interplay along with other external factors will affect the energy of the hot electrons produced and hence the hot electron injection efficiency. Therefore, a careful experimental study of the size dependence of the hot electron injection efficiency would give a lot of information on these mechanisms that could be useful for the field of plasmonics in general. This study was done as part of this thesis and the important results are presented here. Silver nanoparticles are used for this study mainly because silver does not have interband excitations in the visible region of light and hence would allow to solely focus on the size dependence of the surface plasmon decay mechanisms. Silver nanoparticles of

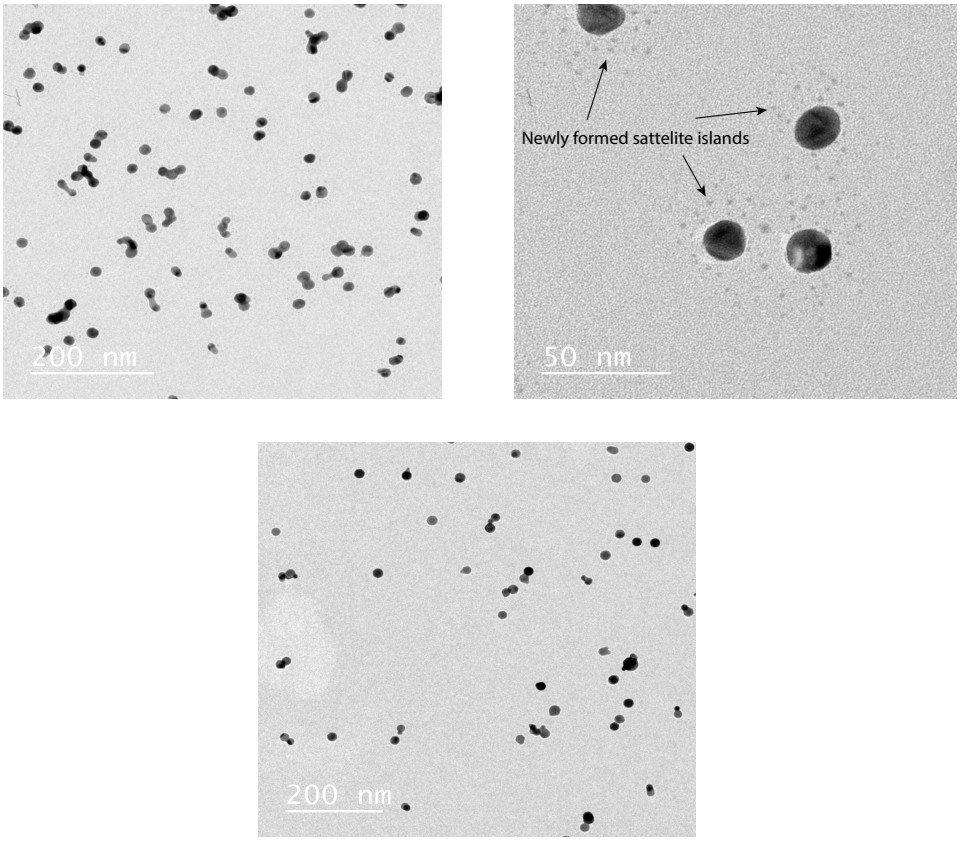

Figure 4.9: (Top left) Degradation of silver nanoparticles when exposed to humidity (Top left) New sub-nanometer silver islands formed by particle degradtion through oxidative dissolution (Bottom) Prevention of particle degradation by storing it in moisture free environment

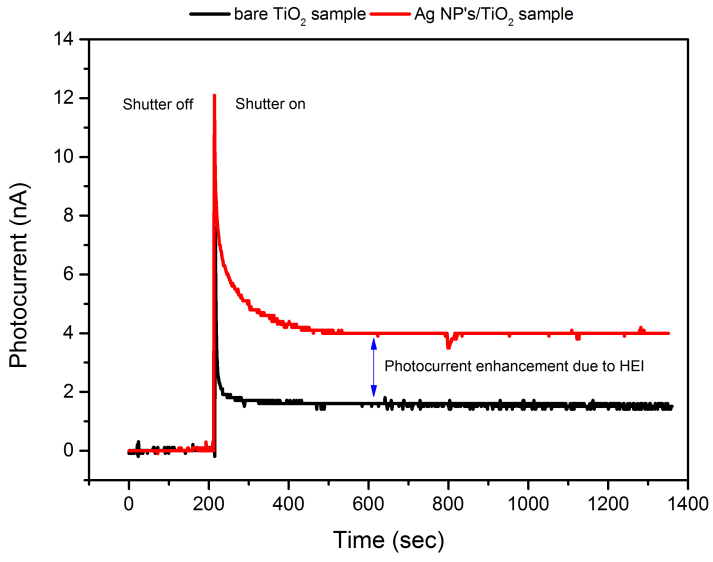

Figure 4.10: Chronoamperometry results of silver-TiO_2 and bare TiO_2 samples under illumination with 430 nm monochromatic light

different sizes can be easily obtained from the spark generator set up, by using different voltages in the DMA for size selection.

4.2.1. CHARACTERISATION

TEM ANALYSIS

Characterisation of the size and shape of the nanoparticles is crucial for this study. A nearly monodisperse size distribution is required to perfectly understand the deviation of HEI efficiency with size. A TEM analysis was performed to check the size distribution of the nanoparticles. 239 particles were analysed to make the size distribution and a gaussian curve was fitted to obtain the mean and standard deviation of this distribution. Only particles with sphericity between 0.7 - 1 was used to make the size distribution, leaving out the agglomerates. The details of the fitting are given in Appendix G. It was observed that the nanoparticles had a nearly monodisperse distribution, as expected. The shape of the nanoparticles were also nearly spherical with minimum agglomeration. Higher amounts of agglomeration was found in bigger particles. This could be due to the insufficient residence time in the oven for these particles to become perfectly spherical. Bigger particles require longer residence time in the oven. It was also noticed that the standard deviation of the size distributions increased with the particle size. The TEM images and their size distributions are shown in figure 4.11, 4.12 and 4.13. The mean particle size and the standard deviation obtained from the fitting are shown in the figures.

UV-VIS ABSORPTION SPECTROMETRY

The plasmon resonance frequency of silver nanoparticles are around ~ 405 nm in this environment (air-metal-TiO_2). This resonant frequency can shift marginally with change in the size of the nanoparticle. The absorption cross-section of the nanoparticles also vary with the size of the nanoparticles. The UV-Vis spectroscopy was performed to study the absorption of the plasmonic silver nanoparticles of different sizes used in this work. The results are plotted in figure 4.14. The characteristic plasmon resonance peak of silver was visible at ~ 405 nm. A second peak was also visible at ~ 525 nm which is attributed to the dimer interactions as discussed in the next section. This second peak position can vary depending on the average particle – particle distance at the substrate surface. The concentration of the nanoparticles on the surface of the substrate was kept low, by using low deposition times, to minimise dimer interactions that could have an effect on the HEI efficiency at very high concentrations (very high concentrations on the surface of the substrate could affect the HEI efficiency, as explained in the next section). A high absorption of light was seen for the bigger particles used in this study even at small concentrations, owing to its high absorption cross-section.

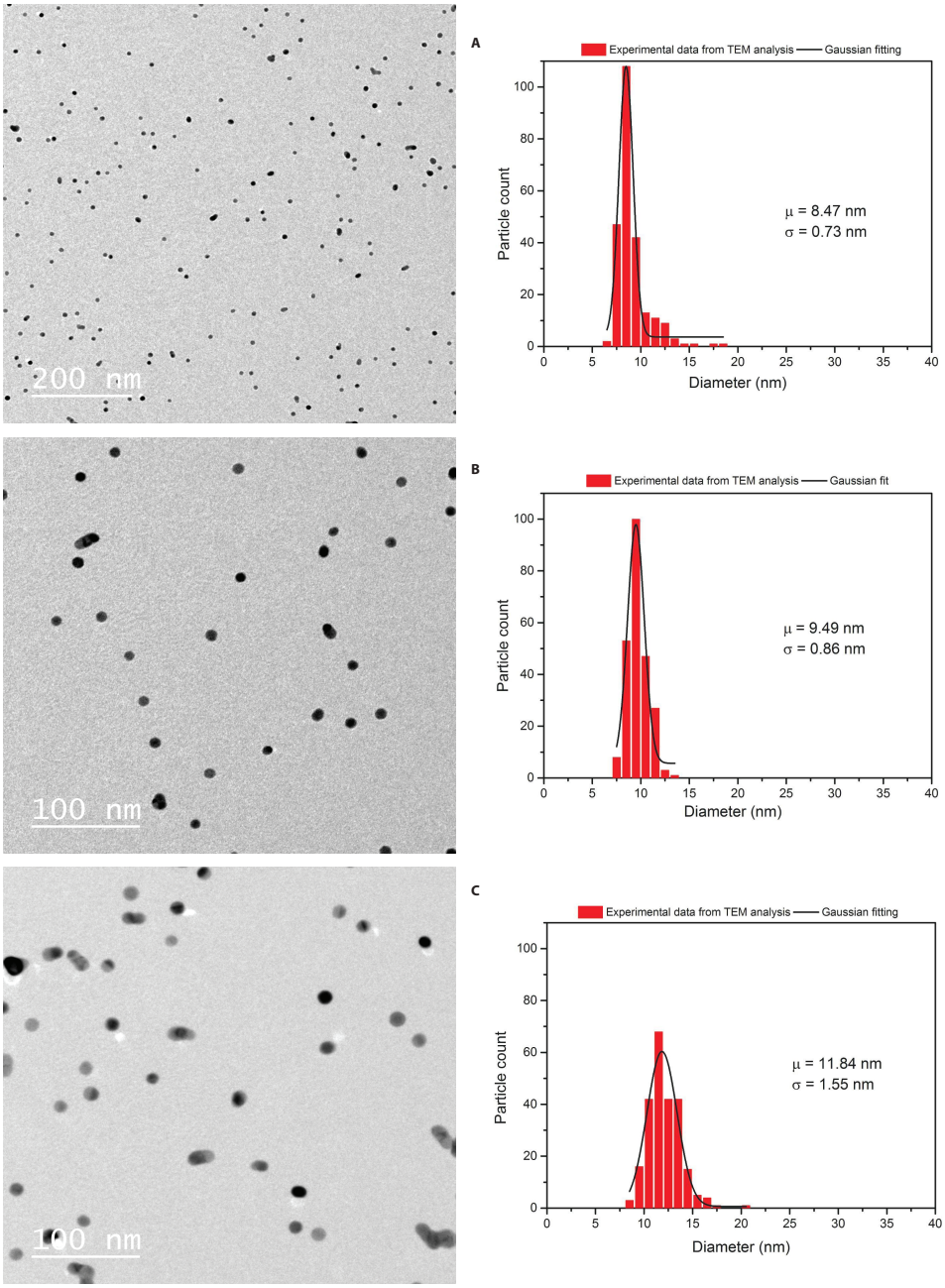

Figure 4.11: TEM images and their particle size distribution for different sizes of silver nanoparticles used in this study in the order A) 8.47 nm B) 9.49 nm C) 11.84 nm. Their gaussian fitted particle size distributions are shown on the right.

4.2.2. PHOTO-ELECTROCHEMICAL TESTING

INCIDENT PHOTON TO CURRENT CONVERSION EFFICIENCY (IPCE)

Photo-electrochemistry was used in this thesis to study the plasmonic behaviour of these nanoparticles. The size dependence of the hot electron injection of the plasmonic silver nanoparticles was studied using the IPCE experiments. The IPCE experiment allows to study the wavelength dependence of the HEI efficiency. Figure 4.15 shows the IPCE responses of the TiO_2 samples deposited with different sized silver nanoparticles used in this study. Figure 4.16 shows the contribution of silver nanoparticles to this enhancement obtained by subtracting of the contribution of the contribution from a blank TiO_2 sample. These measurements were obtained from the third run at a potential of 0.56 V vs RHE. Since the focus of the study was to see the plasmon induced hot electron injection of the silver nanoparticles, the excitations were only done for wavelengths

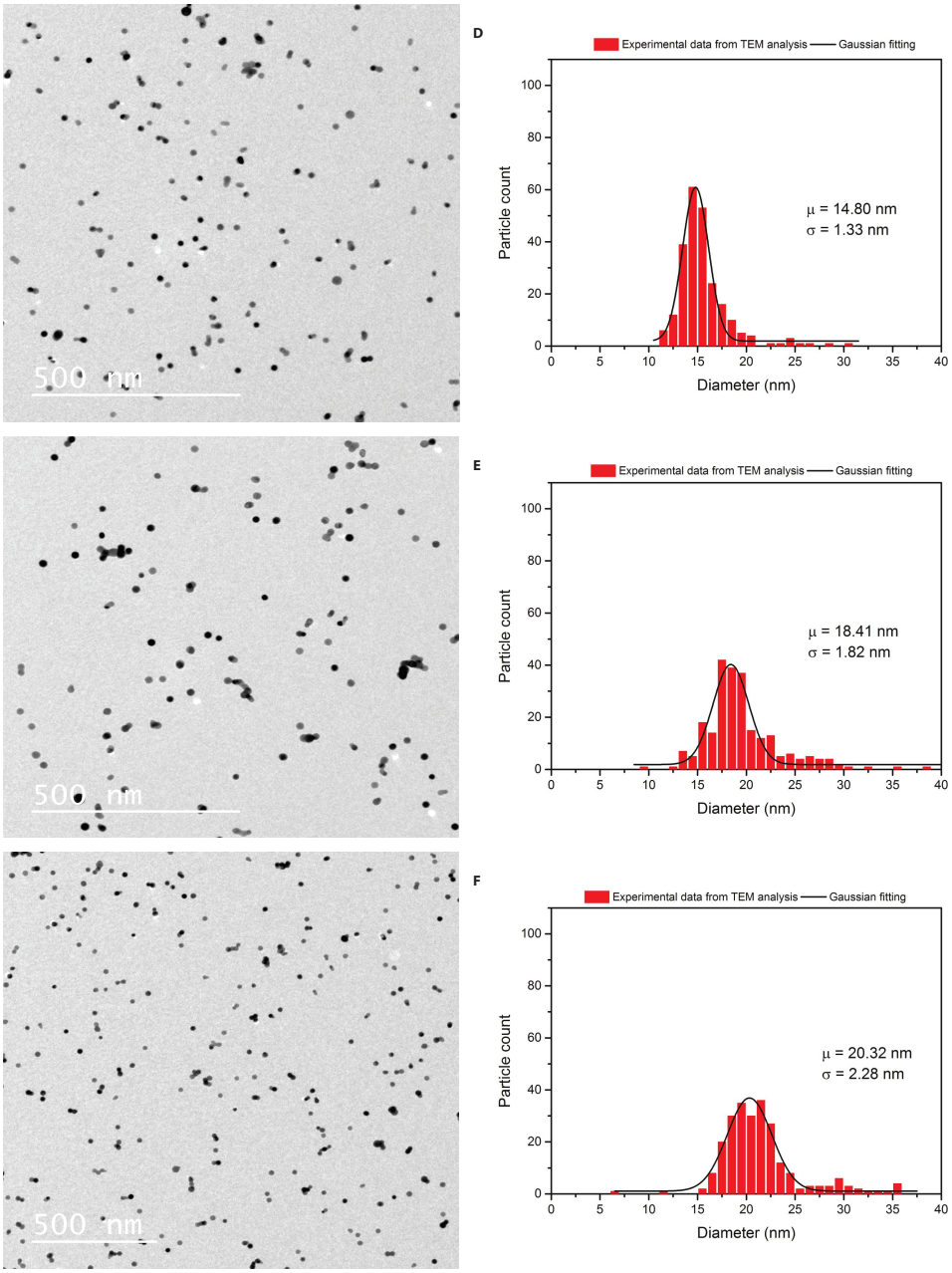

Figure 4.12: TEM images and their particle size distribution for different sizes of silver nanoparticles used in this study in the order D) 14.80 nm E) 18.41 nm F) 20.32 nm. Their gaussian fitted particle size distributions are shown on the right.

longer than 420 nm. These plots showed an increase in IPCE similar to the absorption trend discussed before. From previous studies, it is already known that the peak for plasmon resonance for silver in the electrolyte environment is at ~ 420 nm (Figure 4.6 (Right)). It is difficult to conclude much from the IPCE plots about the size dependence on HEI efficiency, as the IPCE measurements depends on both the size and concentration (and absorption) of the particles. Therefore, the IPCE measurements are corrected for the absorption to facilitate the comparison, as discussed in the next subsection.

ABSORBED PHOTON TO CURRENT CONVERSION EFFICIENCY (APCE)

If the particles have the same shape, the APCE of nanoparticles of different sizes gives the actual HEI efficiency. Here the APCE values are calculated by taking the IPCE values and correcting it with the corrected absorption (accounting for the approximate wavelength shift due to the refractive index change). Figure 4.17,

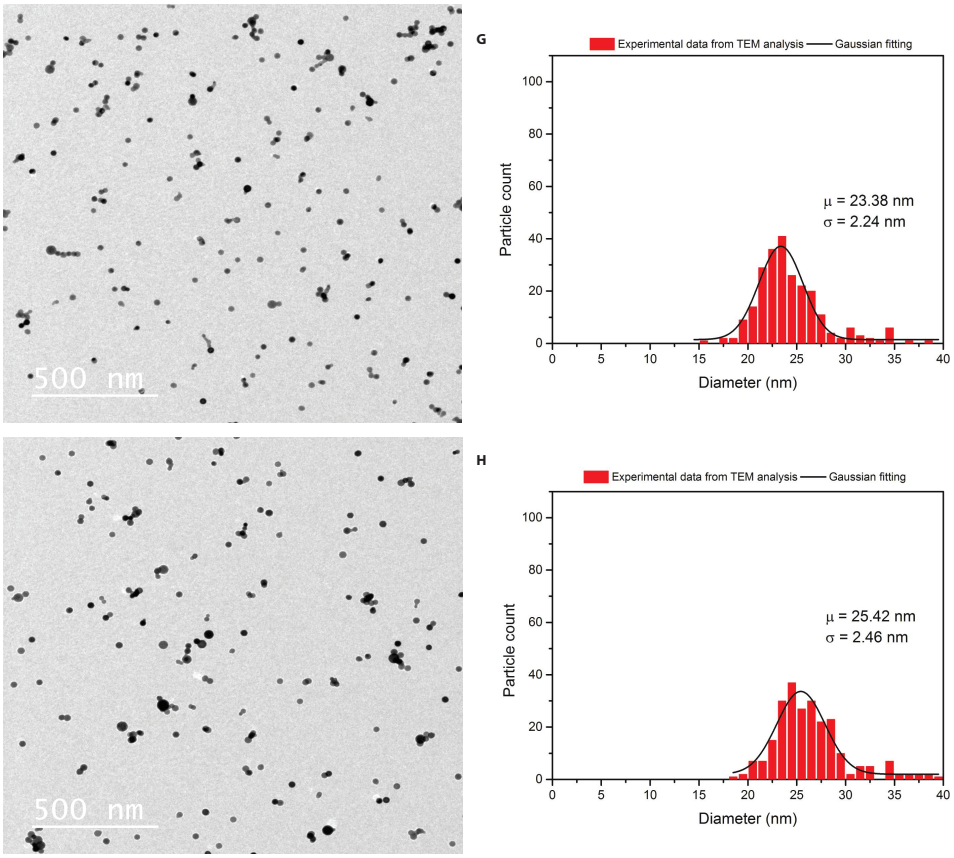

Figure 4.13: TEM images and their particle size distribution for different sizes of silver nanoparticles used in this study in the order G) 23.38 nm H) 25.42 nm. Their gaussian fitted particle size distributions are shown on the right.

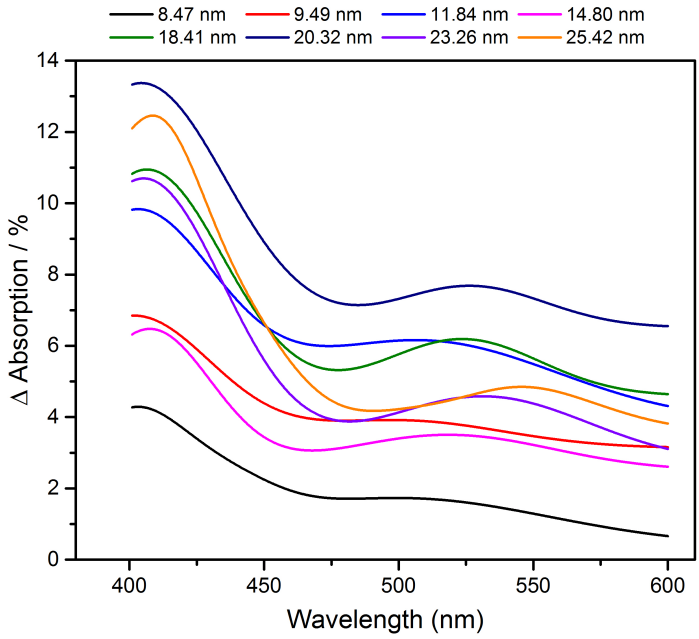

Figure 4.14: UV-Vis spectroscopy measurements showing absorption of the plasmonic nanoparticles of different sizes obtained by subtracting off the background TiO_2

shows the size dependency of APCE values at three different wavelengths. It is clear that the trend for size dependence of APCE is similar at all three wavelengths, suggesting that the same phenomena's are effecting

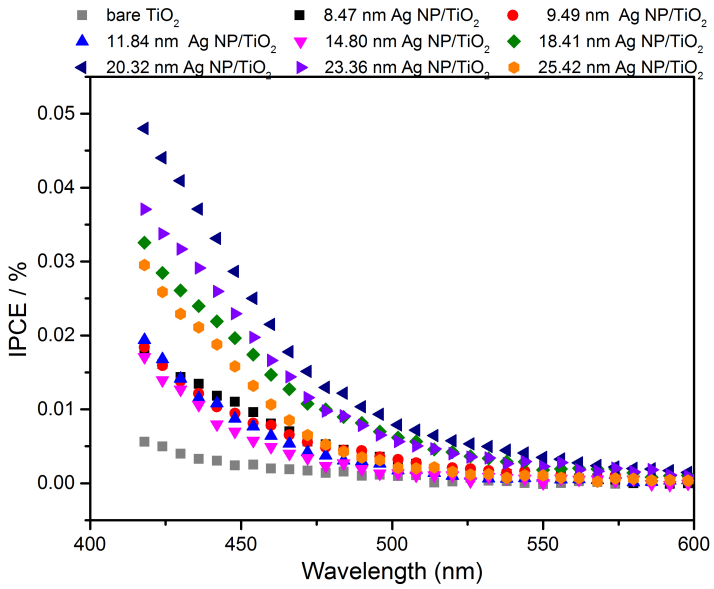

Figure 4.15: IPCE measurements of the silver NP - TiO_2 sample with wavelength of light, for different sizes of silver NP's compared to that of bare TiO_2.

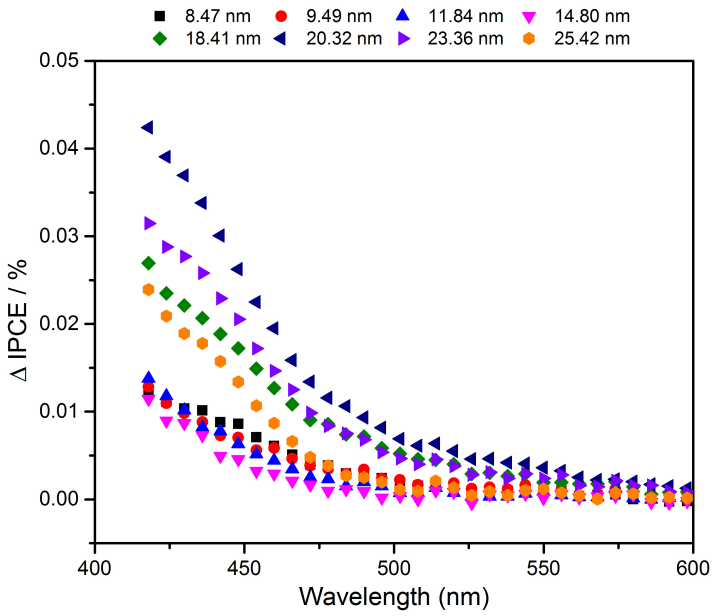

Figure 4.16: IPCE enhancement due to the silver NP's of different sizes obtained by subtracting off the contribution of bare TiO_2.

the overall size dependence. On a close observation of this plot, the HEI efficiency is seen to increase with particle size between 10 nm and 20 nm, dropping above 20 nm with further increase in size. Interestingly, the HEI efficiency was also seen to increase sharply with decrease in nanoparticle size below 10 nm. These trends suggests that there are many competing parameters that effect the size dependence of HEI efficiency and warrants a detailed discussion, which is left for the next chapter. The results reported here are from the second try. In the initial experiments of the size dependence, the particle degradation was not noticed. Therefore, these experiments had to be redone. The results from the initial experiments are given in Appendix F. The APCE plot is very similar to the plot given in 4.17

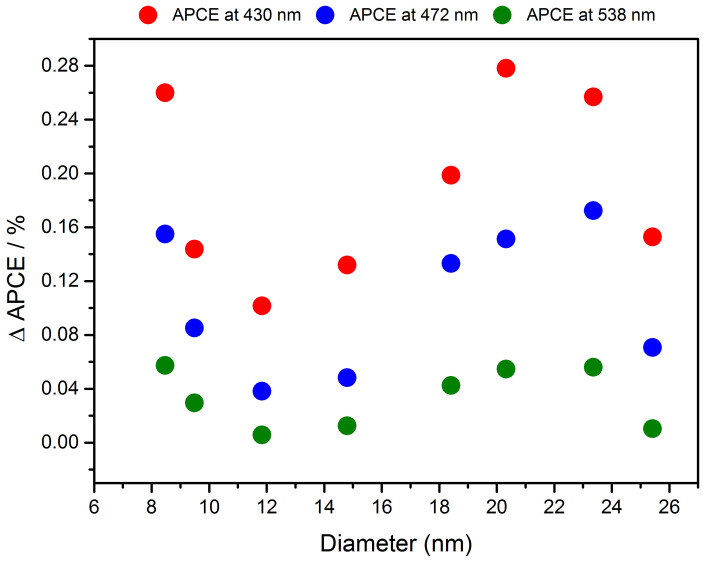

Figure 4.17: APCE of the silver nanoparticles of different sizes at three different wavelengths.

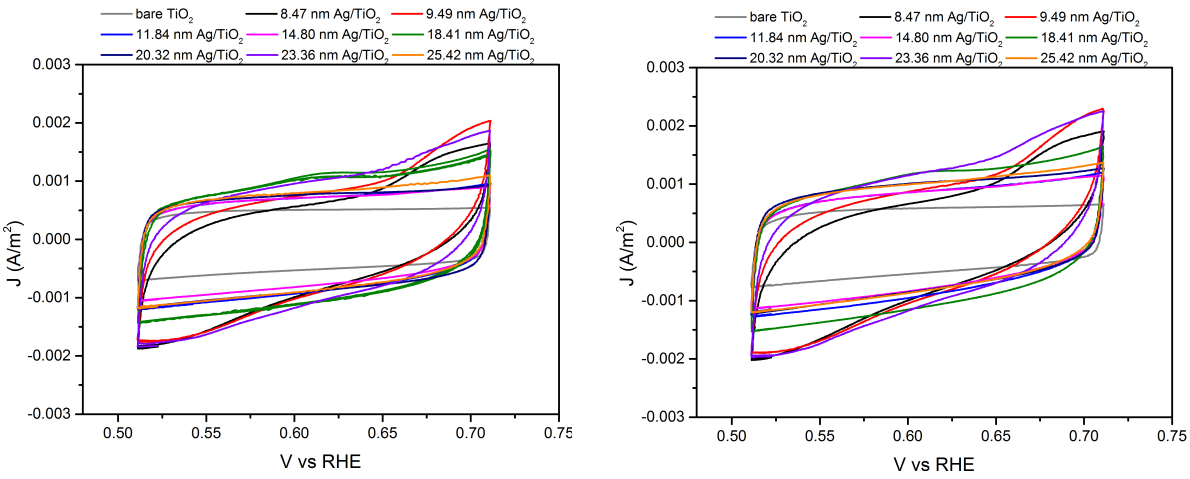

Figure 4.18: JV curves for the silver-TiO_2 samples of different sizes silver NP's - dark (left) and light (right) measurements.

CYCLIC VOLTAMMETRY

Cyclic voltammetry was performed within a small range of potentials to see the approximate behaviour of the photocurrent to the applied potential .This small range of potentials, 0.51 V vs RHE to 0.71 V vs RHE, was chosen to avoid oxidative loss of silver nanoparticles from the substrate surface as discussed before. Figure 4.18 shows the dark and light measurements of all the samples used in this study. The light measurements were done at a monochromatic wavelength of ~ 430 nm. It was difficult to draw any conclusion from these plots, regarding the size dependence, mainly because of the difference in particle concentration at the surface of the substrate. But a clear increase in photocurrents is visible on the nanoparticle deposited substrates compared to bare TiO_2 both in dark and light measurements, as seen in figure 4.19.

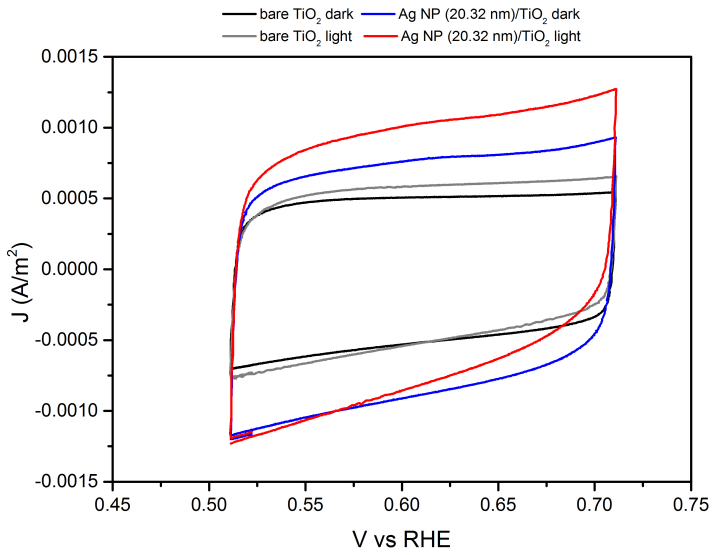

Figure 4.19: Comparison of the dark and light measurements of the silver-TiO_2 sample (20.32 nm) against a bare TiO_2 sample

4.3. DEPENDENCE OF HEI EFFICIENCY ON NANOPARTICLE CONCENTRATION

Dependence of hot electron injection on the particle concentration is looked into in this section of this thesis report. As the concentration of the nanoparticles increases on the substrate surface, the surface starts to become more dense. This would initiate particle-particle interactions along with the particle light interaction in these plasmonic nanoparticles. Especially when these particles are really close to each other, < 1nm, these interactions cannot be considered from a classical perspective anymore. The impact of these particle - particle interactions on the hot electron injection efficiency is not looked into before. In this section, some light is thrown into this aspect based on the observations from these set of experiments. Spherical silver nanoparticles of ~ 14 nm were used for this study.

4.3.1. CHARACTERISATION

UV-VIS ABSORPTION SPECTROMETRY

Particle concentration on the surface of the substrate was increased by longer times of deposition of nanoparticles from the spark discharge set up. More concentration of plasmonic nanoparticles on the substrate surface means that, more light gets absorbed. A UV-Vis spectroscopy measurement confirms that the absorption of the plasmonic nanoparticles have increased with longer deposition times. In figure 4.20, the absorption increase with particle concentration is clearly visible. The plasmon resonance peak for silver nanoparticles is clearly visible at ~ 405 nm similar to the previous measurements. A second peak, at ~ 525 nm, increasing with the increasing concentration is also visible in this figure. This second peak is attributed to the particle – particle interactions and is widely discussed in literature [72, 76].

4.3.2. PHOTOELECTROCHEMICAL TESTING

INCIDENT PHOTON TO CURRENT CONVERSION EFFICIENCY (IPCE)

IPCE experiments were performed on these samples to test the concentration dependence of hot electron injection efficiency. Figure 4.21 shows the IPCE enhancement due to the plasmonic nanoparticles, obtained by subtracting off the contribution of TiO_2. The obtained IPCE curves resemble the plasmon resonance curves as before. A peak was not visible for the sample with the lowest concentration, possibly because of the low enhancement in this case owing to the low concentrations. It was observed that as the concentration

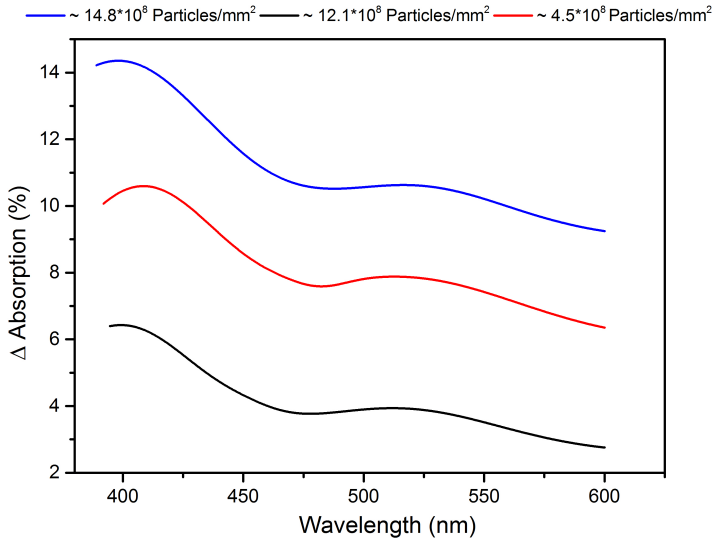

Figure 4.20: Increase in absorption of the sample with concentration of silver plasmonic nanoparticles on the substrate surface (subtracting off absorption off bare TiO_2)

of the nanoparticles increased, the IPCE also increased in the low concentration range. Further increase in concentration (i.e., the high concentration region) resulted in a decrease in IPCE performance. Another striking factor to notice is that the IPCE peaks do not have a second peak at around ~ 525 nm similar to that of the absorption peaks. The particle concentrations mentioned in figure 4.20 and figure 4.21 are are a very rough estimation based on the measured flow and the particle concentration measured by the CPC, assuming a 100% deposition efficiency. More discussion on this is done in the next chapter.

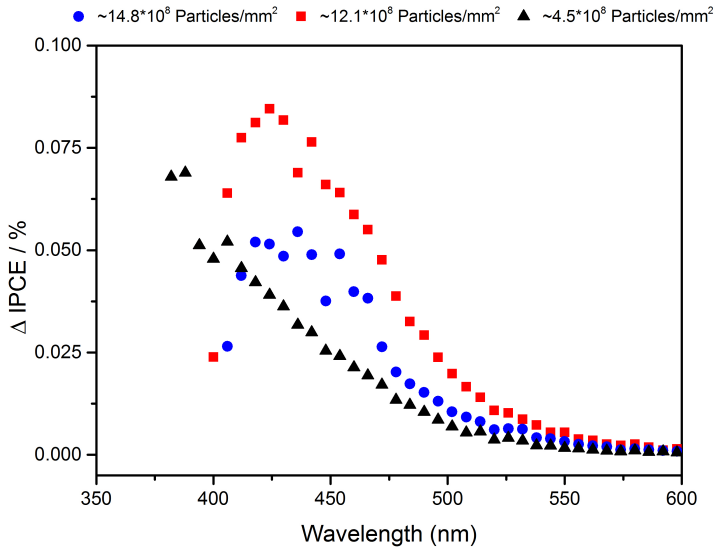

Figure 4.21: IPCE enhancement by the silver nanoparticles at different concentrations (subtracting off bare TiO_2)

One important point to note here is that, these are some of the first experiment results of this thesis. Here, the silver sample was not stored in a moisture free environment as the silver nanoparticle degradation on exposure to atmosphere was not noticed at this time. Therefore, the samples could have a degraded a bit and might have affected the resultant measurements. But since similar time gap was usually maintained between sample preparation and testing, it could be assumed that any possible degradation would be at the same extent for all the samples. The IPCE values reported here are higher than the previous two sections. This increase is attributed to the newly formed sub-nanometer particles upon degradation on exposure to moisture in air. These sub-nanometer particles have high hot electron injection efficiencies owing to their small sizes.

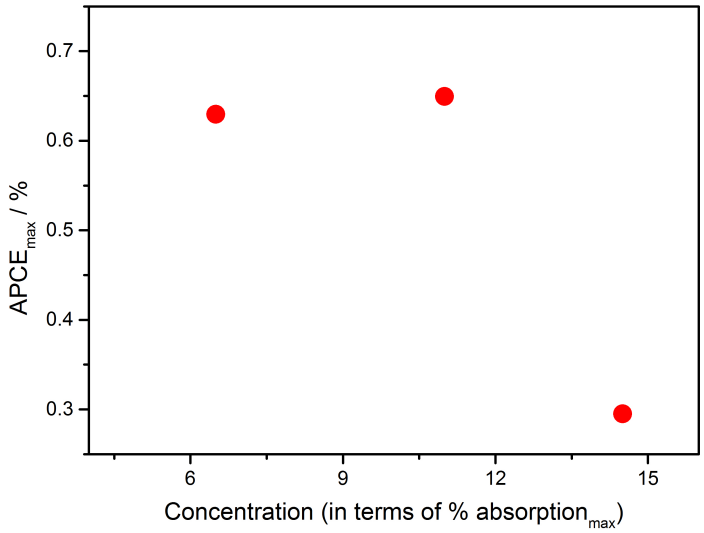

Figure 4.22: APCE of silver nanoparticles at different concentrations. A clear decrease at higher concentrations is visible.

The nanoparticle deposition method used in this thesis does not really allow to accurately control the gap between the nanoparticles, which is important for the better understanding the effect of concentration on the HEI. Since this was not possible with the current set up, these experiments were not redone.

ABSORBED PHOTON TO CURRENT CONVERSION EFFICIENCY (APCE)

APCE calculation were done get an idea in the decrease in HEI efficiency with increase in concentration. APCE calculations corrects for the absorption of the particles in the IPCE measurements, i.e., corrects for the concentration. This would give a better idea of this effect of concentration on the HEI efficiency. Here the $APCE_{max}$ was used to compare the HEI performance. The $APCE_{max}$ value was calculated by taking the peak IPCE values and dividing it with the peak absorption value of the plasmonic resonance. For the lowest concentration sample, the IPCE value at ~ 420 nm was used to make this calculation. As observed from figure 4.22, the $APCE_{max}$ values are almost constant in with increasing concentration at low concentration range, suggesting that particle-particle interactions are not having an effect. At higher concentrations the $APCE_{max}$ value decreased with increased concentration could possibly suggest that the particle-particle interactions, which should increase with increasing concentrations, are having an effect on the HEI efficiency.

5

DISCUSSION

5.1. TUNING OF HEI BY VARYING THE NANOPARTICLE COMPOSITION

As discussed in the results section, the plasmon resonance was successfully tuned by alloying two plasmonic nanoparticles. Since the nanoparticles compared here are of the same size range and shape and the testing is done in similar environments, the shift in plasmonic resonance is due to some inherent factor of the newly formed alloy nanoparticles. Plasmon resonance frequency is also a function of the electron density of the nanoparticle, as explained in section 2.2.3. An XPS analysis (figure 4.3) on the valence band confirms that the valence band has indeed been altered upon alloying. Therefore, this shift in plasmonic resonance with alloying can be attributed to the change in electron density of the valence band. El-Sayed et al. [38] proposed that this shift in plasmon resonance wavelength with alloying is linearly proportional to the silver – gold composition in the alloy. A quick calculation according to this model, based on the experimental values from this thesis, would predict a plasmon resonance peak at ~ 460 nm for the alloy nanoparticles. This value is red shifted by ~ 18 nm compared to our experimental value. One important factor to point out here is that the size distribution of the nanoparticles obtained by spark discharge technique, in this thesis, is much more monodisperse than the samples used in El-Sayed et al.'s work. This could be playing a role in the above mentioned shift. Another factor that could play a role is the surface tension of gold and silver. Gold has a higher surface tension (1138 mN/m)[77] compared to that of silver (910 mN/m) [77] at their melting points. Since the spark discharge technique uses a tube oven to make the particles spherical by melting them, it could be that there is more concentration of gold in the centre of the sphere formed owing to its higher surface tension. This means that the silver-gold ratio is not 50%-50% throughout the sphere, but could be an increasing gradient of the concentration of gold towards the centre of the sphere. And since surface plasmon resonance is mainly a surface phenomenon, the blue shift of the observed surface plasmon resonance in these experiments could be explained by the increased amount of silver at the surface of the alloy nanoparticle spheres.

The UV-Vis spectroscopy revealed that the silver, gold and alloy samples had, on an average, ~ 10% absorption. But a similar trend was not visible for the IPCE enhancement by these nanoparticles. Silver nanoparticles had an enhancement of ~ 0.015% compared to that of ~ 0.002% and < 0.0005% for gold, at their respective plasmon resonance frequencies. If the performance was limited by light absorption, these nanoparticles would have exhibited the highest performance at their respective plasmon resonance frequency. But a careful look at figure 5.1, would show that the silver nanoparticles perform better than the alloy and the gold nanoparticles even at the plasmon resonance frequency of alloy and gold nanoparticles respectively. This implies that the nanoparticles are not limited by light absorption but rather by the hot electron energies, transport and the injection process. Literature reports that the mean free path of electrons in silver and gold nanoparticles are ~ 20 nm. [78, 79] Since diameter of nanoparticles used in this thesis are much smaller than this, it would be safe to assume that all the generated hot electrons reach the metal-semiconductor junction for the injection process.

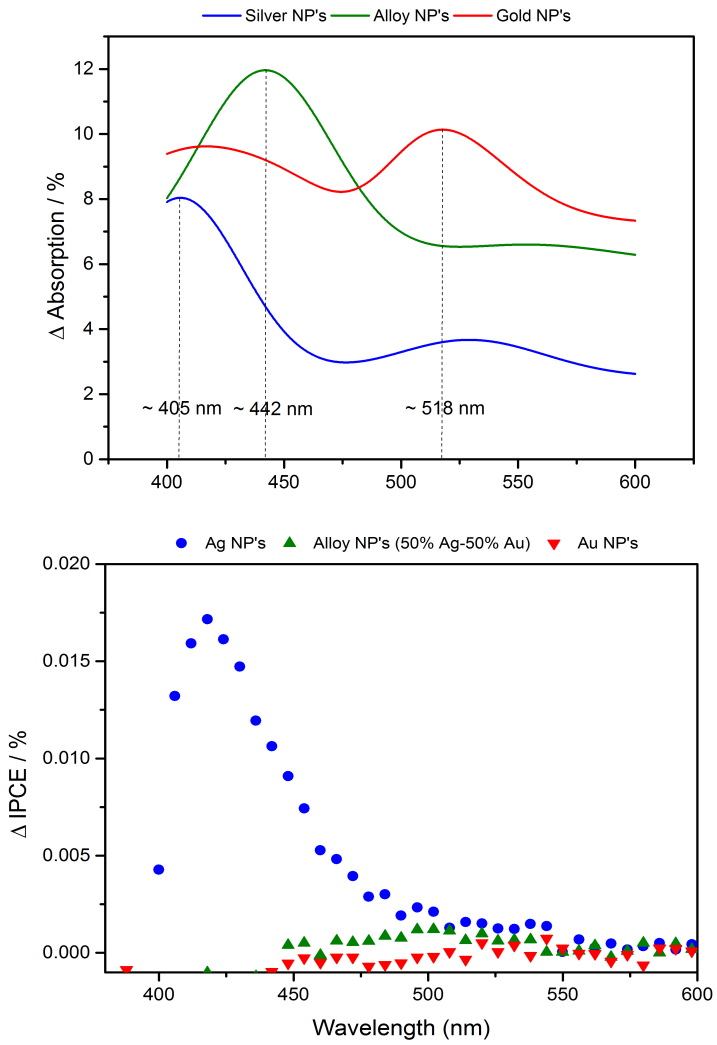

Figure 5.1: (Top) Increase in absorption due to plasmonic nanoparicles. Characteristic peaks of silver, alloy and gold nanoparticles are clearly seen (Bottom) IPCE enhancement of plasmonic nanoparticles outside the OBGE of the semiconductor

This would imply that an inefficient injection process is resulting in the low HEI efficiency. Two factors could result in an inefficient injection process – low hot electron injection energies and a high Schottky barrier. Low hot electron energy distribution in case of gold nanoparticles and hence low HEI efficiency, could be explained by the low interband threshold wavelength for gold (~ 539 nm). This means that most of the electron excitations in gold upon surface plasmon decay, under visible light illumination, is from interband transitions rather than intraband transitions. It was already discussed in section 2.2.6 that intraband transitions result in higher energy hot electrons compared to interband transitions. Similarly, the interband energy wavelength threshold for silver is ~ 335 nm. That is, the silver nanoparticles will have more intraband transitions upon illumination with visible light. The XPS analysis confirmed that the start of the d-bands of silver and gold are in agreement, 3.7 eV for silver and 2.3 eV for gold, with the interband threshold values from literature [80]. The d-band is recognised from an XPS plot by a sharp rise in the plots, owing to the high density of states in the d-band. The XPS analysis was also performed for the alloy sample. However, unlike the metal samples, a sharp peak was not visible in case of the alloy sample. But instead a gradual shift from 2.3 eV to 3.7 eV in the d-band is visible, implying that the density of states (DOS) of the d-band is shifted to higher energies. This shift in d-band density of states also implies that the alloy samples would have lower probability of visible light induced interband transitions compared to that of gold samples. To compensate for this decrease, more intraband transitions would occur in the alloy samples resulting in higher energy hot electrons and higher hot electron injection efficiency. This shift in d-band DOS with alloying and resulting impact on the hot electron injection efficiency is schematically represented in figure 5.2.

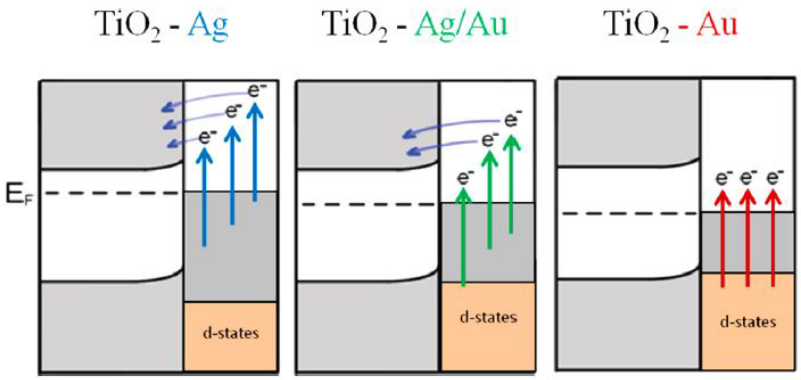

Figure 5.2: Schematic showing the shift in d-band edge and the resulting effect on the decrease in interband transitions and hot electron injection by alloying gold with silver [43]

Another factor, as mentioned above, that could result in an inefficient injection process is a high Schottky barrier. Different metal – semiconductor junctions have different Schottky barrier heights depending on the metal work function and the semiconductor affinity, as discussed in section 2.2.6. The work function of silver is reported to be ~ 4.26 eV [81] and for gold it is reported to be ~ 5.1 eV [81]. The work function of alloy is expected to be in between these two values. The electron affinity for anatase TiO_2 is reported to be around 5.1 eV [82]. Since the electron affinity of the semiconductor is higher than the work functions of the metals, a zero Schottky barrier height is expected. But the predictions using Mott-Schottky rule is not often accurate owing to some surface states that might be present at the semiconductor surface. It has been theoretically predicted that the work function of silver can rise upto 7 eV depending on the oxygen coverage around the silver atom [83]. The actual values of Schottky barriers for silver and gold - TiO_2 semiconductors composites, obtained experimentally, are around ~ 1 eV and ~ 0.9 eV respectively [82]. IPCE measurements suggested that silver nanoparticles had a higher efficiency compared to gold and alloy nanoparticles, even at the resonance frequencies of gold and alloy nanoparticles. This would imply that it is not the SBH that is limiting the hot electron injection efficiency in case of the alloy and gold nanoparticles, instead it is the energy of hot electrons as discussed above.

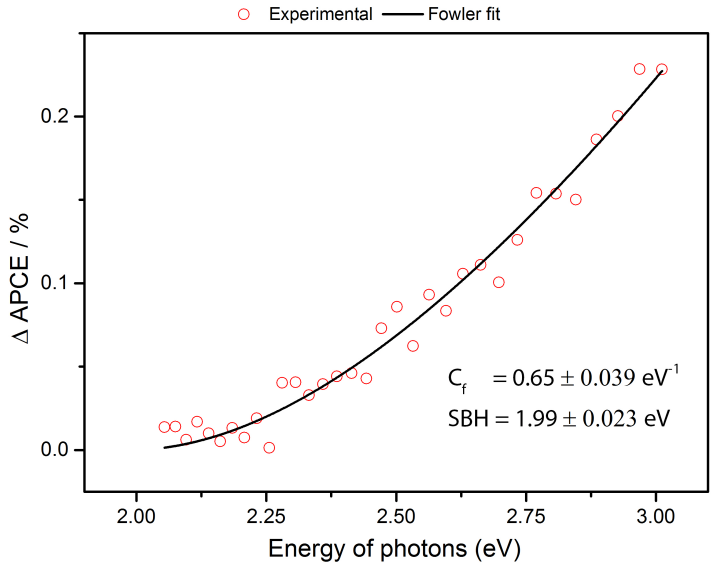

Figure 5.3: Fitting the APCE plot, obtained by correcting the IPCE measurements using the corrected absorption, using the Fowler theory

Fowler theory can be used to predict the photoemission of electrons from a metal. Curve fitting was performed on the APCE curve for silver NP's using the modified fowler equation (see section 2.2.6) to calculate the actual SBH. The fitting estimated the SBH to be ~ 1.99 eV and the fowler coefficient of about ~ 0.65

eV^{-1}.The details of the fitting are given in Appendix E. Both values are reasonable when compared to literature [82, 84]. This value is a bit higher than previously mentioned 1 eV for silver that was determined experimentally [82]. This could be because of the nanostructure form (small spherical nanoparticles) of silver used in this study compared to the silver film used in their experimental study. The nanostructure form of silver could result in more coverage of the reactant undergoing oxidation around a single silver atom and hence could result in a higher work function. The difference in the SBH obtained could also be from the different environments used for these experiments. Theoretical predictions estimate plasmon induced hot electron energies of upto 4 eV [49] for silver nanoparticles. Also, from the APCE trend it is understood that the energy of the hot electron is the limiting factor in case of silver and not the SBH. However, similar fitting in case of gold and silver was unsuccessful due to their very low response possibly suggesting that both high SBH and low hot electron energies are the limiting factors. A lower SBH could be expected in case of gold and alloy nanoparticles, compared to silver, because of the lower affinity of oxygen to gold. But comparing with silver (which has a higher SBH) it can be concluded that it is the hot electron energy, owing to the increased interband transitions, that is the limiting factor in case of gold and alloy nanoparticles. Therefore, to summarise, it can be understood that it is possibly the hot electron energies that is acting as the limiting factor for the plasmonic hot electron injection efficiency. Intraband transitions should be preferred, over interband transitions, to obtain a higher efficiency of plasmonic hot electron injection.

5.2. DEPENDENCE OF HEI EFFICIENCY ON NANOPARTICLE SIZE

The sample characterisation using TEM analysis revealed that the particles are in the expected size ranges and, more importantly, the size distributions are monodisperse. The particles were also almost spherical in shape and had minimum agglomeration. The plasmon resonance frequency of all the samples were seen to be around ~ 405 nm, the resonance frequency of spherical silver nanoparticles in this environment. Mie theory predicts a minor blue shift in this plasmon resonance wavelength with decrease in nanoparticle size. This minute shift in the plasmon resonance is hard to visualize with the current measurements, which are just ~ +/- 2nm apart, because of the comparatively high scan rates used (250 nm/min). However, when particles sizes that are sufficiently far apart from each other, a general trend of blue shift with decreasing particle size is observed as in figure 5.4 (Left). This trend is in agreement with Mie theory predictions shown in figure 5.4 (Right). As mentioned before, the IPCE enhancements are in agreement with the plasmonic resonance peaks suggesting that the enhancement is from plasmonic hot electron injection. But it is difficult to conclude anything regarding the size dependence of HEI efficiency because of the difference in concentration. Therefore, the APCE plots were presented and used for the comparison.

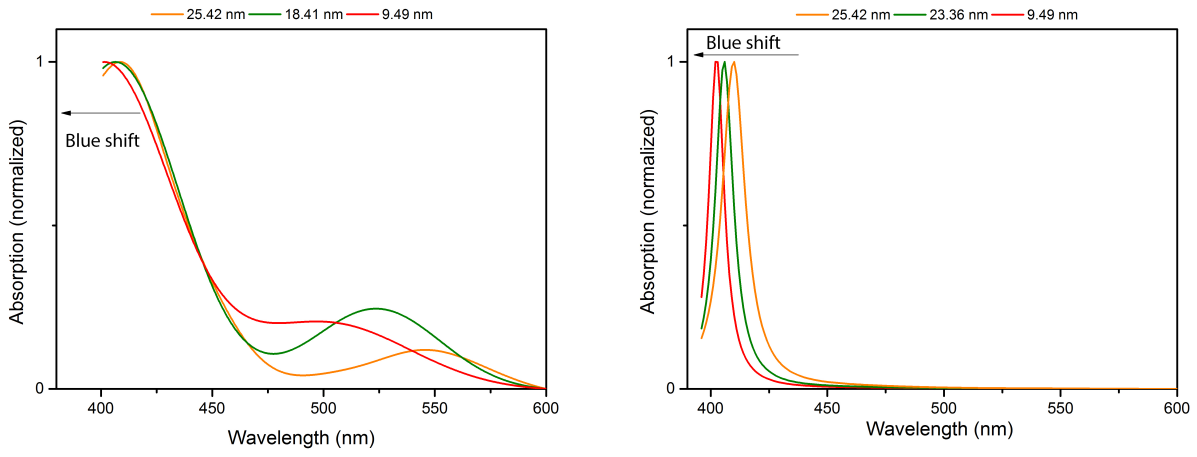

Figure 5.4: (Left) Blue shift of the surface plasmon resonance with decreasing particle size as seen from experimental results (Right) Blue shift in surface plasmon resonance predicted by Mie theory using a refractive index of 1.5 to account of the anisotropic refractive index in the actual case

The HEI efficiency (APCE) is product of the efficiencies of three distinct processes – hot electron generation, hot electron transport from the point of generation to the point of injection and hot electron injection process. Figure 5.3 in the previous section already showed that the plasmon induced hot electrons, in case of

silver, are not completely limited by Schottky barrier height but rather by the low energies of the hot electrons produced. The size dependence of the HEI efficiency (APCE), as seen in figure 4.17, suggests that the size of the nanoparticles has an effect on the hot electron energy at the point of injection. Therefore, the size effect can be subdivided into two factors :-

- The energy of the hot electron formed by the non-radiative plasmon decay
- The energy loss during the transport of the hot electron from the point of excitation to the point of injection (at the metal-semiconductor junction)

As discussed in the previous section, high energy hot electrons are produced via intraband excitations compared to interband excitations. For silver, the energy threshold for interband excitations is at ~ 3.7 eV implying that intraband transitions dominate in the visible region of light. Visible light does not have enough momentum to cause an intraband excitation to a high energy state and requires the assistance, from a phonon or from the surface, to transfer the extra momentum.

The coupling of plasmons with the incoming light in these nanostructures is not self-sustaining and the plasmon will eventually decay. The decay mechanisms of surface plasmons are explained in section 2.2.8 and are broadly classified into radiative and non-radiative decay mechanism. Both these mechanisms compete each other with non-radiative decay dominating for particles of very small sizes and vice versa. As explained before, only phonon-induced and surface-induced decay mechanisms will result in hot electrons. For silver nanoparticles, these hot electron excitations are intraband excitations and hence the light cannot directly excite an electron. A hot electron excited by the decay of a plasmon will need a phonon to transfer the extra momentum to excite it to a high energy state. This is called a phonon induced plasmon decay and is an intrinsic property and hence independent of the size of the nanoparticle. Otherwise this additional momentum is directly obtained from the surface plasmons and is called surface induced plasmon decay. The surface induced plasmon decay mechanism is a size dependent phenomena and is prominent for very small particles. When surface plasmons are confined to oscillate in very small nanoparticles, more electric field energy is converted into kinetic energy of the oscillating electrons (see section 2.2.1) and hence it attains sufficient momentum to directly excite an electron on the decay of this surface plasmon. Both these mechanisms are schematically represented in figure 5.5.

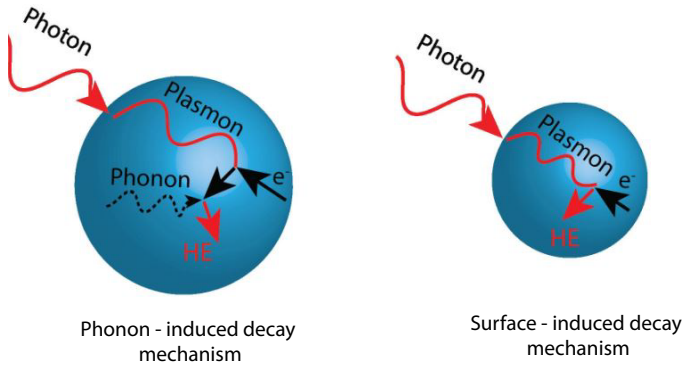

Figure 5.5: (Left) Plasmon decay to produce hot electrons with extra momentum transfer from a phonon (Right) Direct plasmon decay when the plasmon itself provides the extra momentum required for the transition

The surface plasmon decay is normally expressed in terms of linewidth, the full width at half maximum, which is related to the dephasing time of the surface plasmon. And this dephasing time is dependent of the decay mechanism. The overall dephasing time is a result of the competition between the radiative and non-radiative decay mechanisms along with the resistive losses in the metal. The phonon induced non-radiative decay and pure resistive loss are an intrinsic property of the material and can be combined together and called intrinsic decay mechanism. Therefore, the overall linewidth of the surface plasmon decay is expressed as the sum of linewidth contribution of each mechanism as [85],

$$\Gamma = \frac{2\hbar}{\tau} \tag{5.1}$$

$$\Gamma = \Gamma_{int} + \Gamma_{rad} + \Gamma_{surf} \tag{5.2}$$

Where, Γ is the line width of the surface plasmon decay, τ_{int} is the intrinsic plasmon decay contribution to the dephasing time, τ_{rad} is the radiative plasmon decay contribution and τ_{surf} is the surface induced plasmon decay contribution to the dephasing time of the surface plasmon. The dephasing time for intrinsic decay mechanism for silver can obtained from literature ($\frac{\hbar}{\tau_{int}} = 0.125eV$)[86]. The nanoparticle size dependent dephasing time for radiative decay and surface induced decay mechanisms are given by [85, 87]

$$\Gamma_{rad} = 2\hbar\kappa_{rad}V \tag{5.3}$$

$$\Gamma_{surf} = 2\hbar g_s \frac{v_f}{D} \tag{5.4}$$

where κ_{rad} is the radiation damping constant, g_s is the surface factor and D is the particle diameter. The values used for these calculations ($g_s = 0.7$ [86], $v_f = 1.39 * 10^6 m/s$ [88] and $\kappa_{rad} = 5.5 * 10^{-7} nm^{-3} fs^{-1}$ [87]) were obtained from literature. Using these relations the size dependency of these decay mechanisms, for the size range under consideration, on the linewidth is plotted in figure 5.6 along with the linewidth calculated for intrinsic decay mechanism using the value of intrinsic dephasing time from literature. This plot shows that the surface induced decay mechanism dominates for particles below ~ 10 nm and above this threshold, the phonon induced mechanism dominates. The radiative decay mechanism only has minimal contribution in this size range. Based on this information, the APCE results obtained in this thesis can be divided into two regions, for further discussion. The surface induced plasmon decay dominated region below 10 nm and the phonon induced plasmon decay dominated region above 10 nm (Figure 5.7).

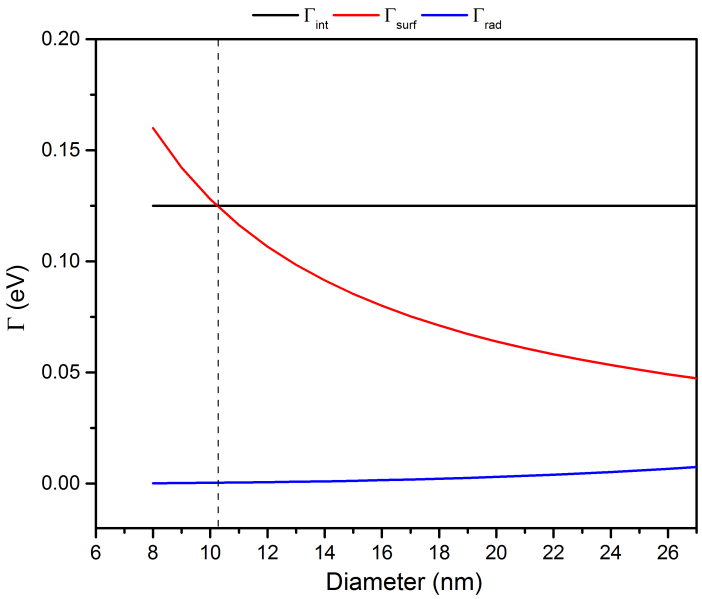

Figure 5.6: Estimation of contributions of the three mechanisms under consideration

The sum of the linewidth contribution of the size dependent decay mechanisms (radiative and surface induced) was also plotted to see the linewidth minimum, as in figure 5.8. The linewidth minimum or the maximum plasmonic enhancement is obtained at ~ 33 nm as per these predictions. Above this size the radiative decay of surface plasmons dominates. Therefore, the silver nanoparticles will have maximum near field enhancement at 33 nm. But this near field enhancement decreases as the size of the nanoparticle decreases

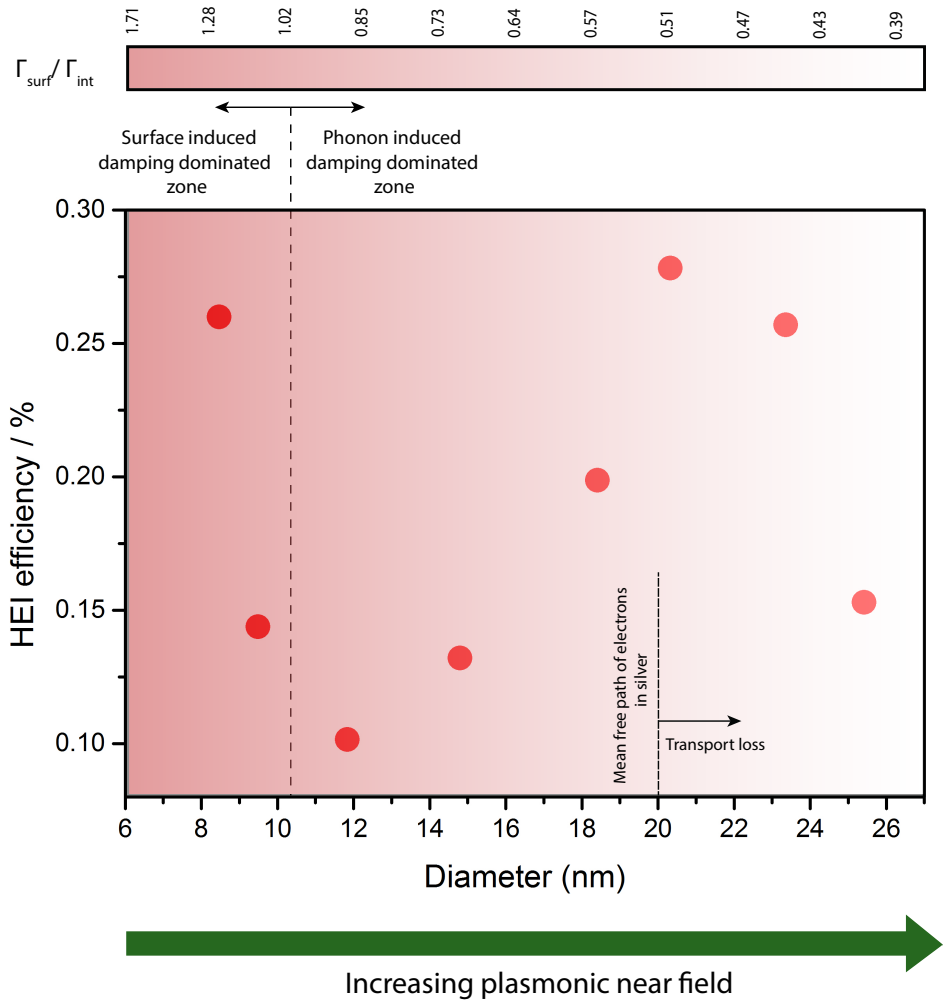

Figure 5.7: Figure summarising all the different effects involved in determining the hot electron injection efficiency. The experimental values of APCE of different sized silver nanoparticles at 430 nm are plotted in combination with the theoretical aspects

due to surface induced decay of plasmons which increases with decreasing particle diameter [39]. Less hot electron excitations are expected with weaker plasmonic near fields [89]. In figure 5.7, in the phonon induced plasmon decay dominated region between 10 nm and 26 nm, the HEI efficiency is seen to peak at ~ 20 nm with the increase in nanoparticle diameter but decreasing with further increase in particle diameter.

The mean free path of electrons in a silver crystal is reported to be ~ 20 nm [78]. This implies that for nanoparticles below 20 nm, there is only minimal energy loss during transport and hence it is the energy of the hot electron produced by the non-radiative plasmon decay that is effecting the overall efficiency. Above 20 nm, the hot electrons could lose energy on transport by electron–electron collisions and thus effecting the overall HEI efficiency. This means that, above 20 nm the probability of electron-electron collisions increases with increase in nanoparticle diameter and hence hot electron injection efficiency decreases. This might be a possible explanation of the decrease in HEI efficiency above 20 nm in figure 5.7. Another possible explanation is the discretization of the energy states with decreasing particle size, as obtained from simulations using the Jellium model [41]. This implies that the higher energy hot electrons could be produced from the excitations from these discrete states and hence an increase in HEI efficiency is achieved as the particle size is decreased from 26 nm to 20 nm.

With all the above arguments, an increase in HEI efficiency with decrease in particle size is expected below 20 nm. But the experimental results in figure 5.7 suggests otherwise. As mentioned before, the electric near field also decreases with nanoparticle size and this electric near field has an effect on the number of hot electrons excited or the hot electron population. The HEI efficiency is directly dependent on the number of high energy

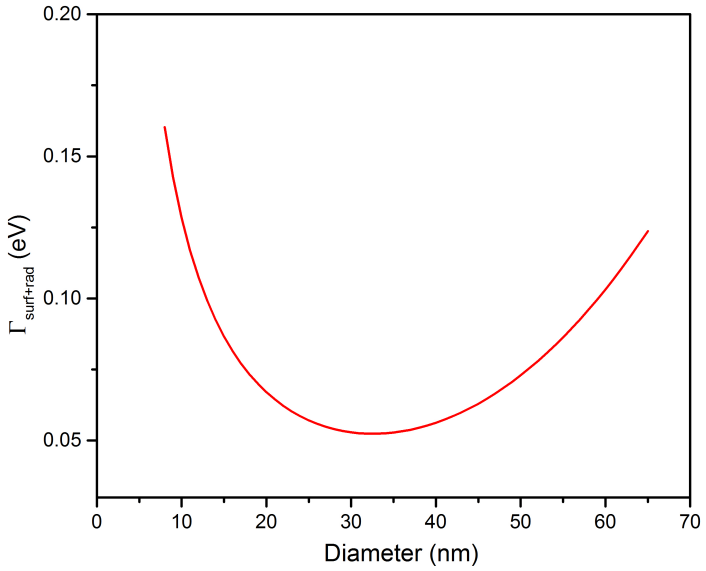

Figure 5.8: Plot of the size dependency of the plasmon decay mechanisms obtained by plotting the sum of the linewidth contribution ofthe size dependent decay mechanisms. A minimum is obtained at ~ 33nm.

hot electron produced and therefore, the decrease in HEI efficiency until the particle size of 10 nm from 20 nm could be attributed to this decrease in electric near field. With weak fields, other intrinsic mechanisms like pure resistive losses (new phonon could get generated on electron - phonon collision) damp the plasmon without generation of a hot electron.

In the surface induced plasmon decay dominated region, below 10 nm, the efficiency is seen to increase with decreasing particle size. This was already observed in an Au/TiO_2 plasmonic solar cell system by Reineck et al. [90]. They attributed this increase in HEI efficiency to the increased contribution to the surface induced decay mechanism, with the decrease in particle size, which they claim to result in higher energy hot electrons. From the results of this work, a possible addition to this argument could be that - it is not only the increased contribution of the surface induced decay mechanism that plays a role in this region but also the decrease in phonon induced hot electron excitations with the decrease in plasmonic near field with particle size that is effecting overall HEI efficiency. The phonon induced plasmon decay normally results in lower energy hot electrons bringing down the HEI efficiency.

5.3. DEPENDENCE OF HEI EFFICIENCY ON NANOPARTICLE CONCENTRATION

As mentioned in the results section, the approximate dependence of HEI efficiency on the concentration was studied in this thesis. The absorption of the nanoparticles were seen to increase with the nanoparticle concentration as expected. A second peak was also visible at ~ 525 nm. This second peak can be attributed to the particle – particle interactions at the substrate surface. When two plasmonic nanoparticles are placed very close to each other, they start interacting. Such a configuration is normally known as plasmonic dimers. As the concentration of nanoparticles on the substrate surface increases, these dimer interactions also increases resulting in the increase in the second peak, as seen in figure 5.9. These dimer interactions and their absorption enhancement are extensively studied in literature [72, 76]. The plasmonic near field of two plasmonic nanoparticles starts to interact when they are close to each other. This interaction is called coupling [76] and results in a hot spot between these particles which has a high enhancement in the electric field. Two types of polarizations results from these interactions – parallel and perpendicular to the dimer axis. The parallel interactions have the plasmonic peak at ~ 520 nm with a shoulder at ~ 430nm and the perpendicular interactions have a peak at ~ 410 nm [76]. These two polarizations along with the single particle polarizations together results in the absorption peaks seen in figure 5.9. Depending on the size and shape of the nanoparticles, a high field enhancement (enhancement factor of ~ 10 compared to singlet particles) between this gap is obtained when the gap distance is of the order of ~ 1 nm as in figure 5.10. [76] But for higher gap distances, the field

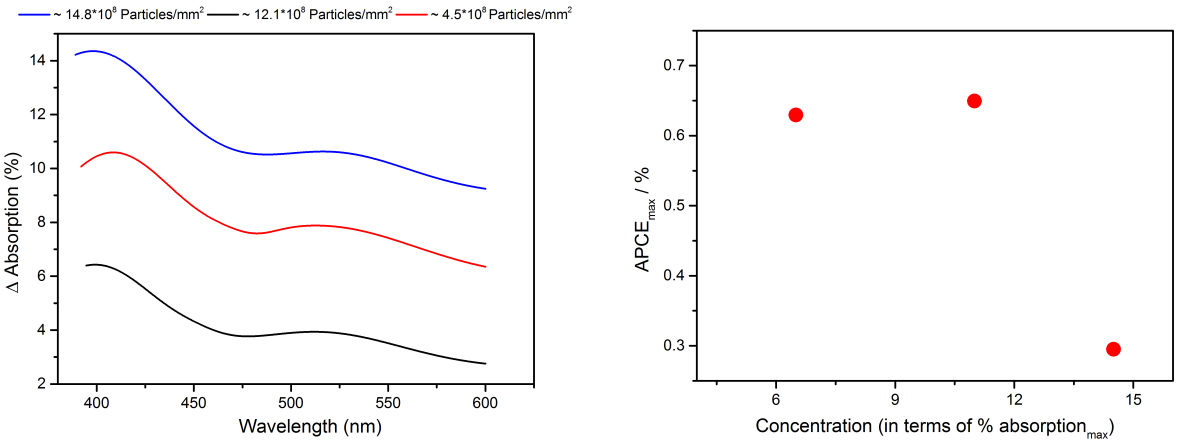

Figure 5.9: (Left)Increase in absorption by the plasmonic nanoparticles with the increase in particle number density on the surface (Right) Decrease in $APCE_{max}$ at higher concentrations

decays exponentially. [91]

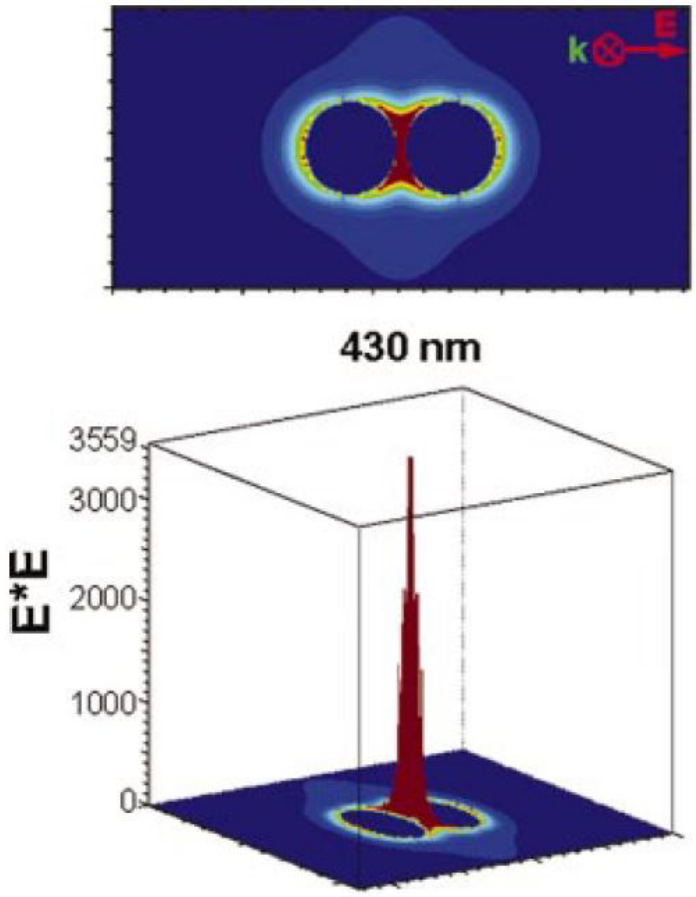

Figure 5.10: Enhancement in plasmonic near field between the gap of a dimer [76]

The increase in IPCE performance is expected with the increase in concentration of particles on the substrate surface, as each particle contributes a fraction of hot electrons injected into the semiconductor. But a decrease in IPCE performance at higher concentrations was unexpected. A plausible explanation for this could be that at higher concentrations, the nanoparticles at the substrate surface are too close to each other which

results in electron tunnelling between the dimer junction, as reported by Scholl et al. [91] This implies that excited hot electrons could get tunnelled into the neighbouring nanoparticle and can neutralize the field rather than getting injected into the semiconductor, thereby decreasing the HEI efficiency. When the particles start to touch each other, the near field is also found to decrease. [76]

As mentioned before, a second peak at ~ 525 nm similar to that of the absorption curves was not observed in the IPCE plots. This second peak seen in the absorption curve are from the parallel polarizations of the dimers, along its axis. [76] This could possibly suggest that the parallel polarizations does not contribute to the HEI and only perpendicular polarizations contribute to the HEI. The orientation of the parallel polarization compared to the semiconductor hot electron injection point could be the reason why parallel polarization does not contribute to the HEI.

The $APCE_{max}$ values are constant for low concentrations and decreases at higher concentration. This implies that the particles remain mainly as singlet particles at low concentrations and there are very less dimers within them and therefore does not affect the overall HEI efficiency. But as the particle concentration is increased, more dimers are formed on the surface of the substrate and dimer interaction begins to take place. And when particles are placed too close to each other, electron tunnelling starts to take place decreasing the overall HEI efficiency as discussed before.

The dependence of HEI efficiency on the nanoparticle concentration should be studied using advanced techniques, that can control the interparticle distances on the substrate surface more accurately, to get a better idea of effect of dimerization on hot electron injection. But the APCE results obtained here suggest that low concentrations can be used to study the hot electron injection in singlet nanoparticles.

6

CONCLUSIONS

In summary, silver, gold and silver-gold alloy nanoparticles were used in this study to understand the fundamental factors effecting the plasmonic hot electron injection phenomena. The spark discharge technique was used to prepare a nearly monodisperse distribution of nanoparticles and was electrostatically deposited onto TiO_2 semiconductor. The TiO_2 semiconductor, because of its high bandgap, allowed for the independent study of the plasmonic HEI. The plasmonic nanoparticles were characterized using multiple techniques and was tested for the HEI efficiency using some photo-electrochemistry techniques. Important conclusions from this research are :

- The tunability of plasmonic hot electron injection by alloying two plasmonic nanoparticles was demonstrated. It was shown that, to have high energy hot electrons for higher HEI efficiencies, intraband excitations should be promoted over interband excitations.
- It was shown that the stability of silver nanoparticles, which has comparatively high HEI efficiency due to its high interband energy threshold, could be improved by alloying with much more stable materials like gold. But this would result in a loss in the HEI efficiency due to an increase in interband transitions.
- Theoretical calculations show that the maximum plasmonic near field enhancement for spherical silver nanoparticles is obtained at ~ 33 nm. Below this, the field decreases due to an increase in surface enhanced damping of plasmon resonance (which increases with decrease in particle size) and it decreases above this threshold due to the domination of radiative decay of surface plasmon resonance for particles of higher sizes.
- It was shown that for particle sizes smaller than ~ 10 nm, the surface enhanced non-radiative decay mechanism is the dominating process. Above this size range, the intrinsic decay mechanism of plasmon resonance dominates with negligible contribution of the radiative decay mechanism for the size ranges considered here.
- Through a careful study of the size dependence of the hot electron injection efficiency, it is understood that particles of smaller sizes (< 10 nm) should be preferred for having higher hot electron injection efficiencies. One possible reason for this was suggested to be the increase in contribution of surface enhanced plasmon resonance decay mechanism and the decrease in contribution of the intrinsic plasmon resonance decay mechanism which results in low energy hot electrons.
- The plasmonic near field, which decreases with nanoparticle size, could possibly have an influence on the hot electron population resulting from the intrinsic decay of surface plasmon resonance. Whereas, the increase in HEI efficiency for particles smaller than ~ 10 nm possibly suggests that hot electron population resulting from the surface induced plasmon resonance decay is independent of this plasmonic near field.

- In the intrinsic plasmon decay size range, NP's of ~ 20 nm should be preferred to have the maximum HEI efficiency. Above this size the probability of electron-electron collisions increases, decreasing HEI efficiency with increase in particle size.
- The number density of the nanoparticles on the substrate surface is also an important parameter that effects the plasmonic hot electron injection efficiency. It was shown that at very high number densities, there is a decrease in HEI efficiency possibly due to electron tunnelling between interacting dimers.
- Above all, it was demonstrated that photo-electrochemistry techniques are an easy way to study plasmonics, even though, the eventual application of the plasmonic hot electron injection could be elsewhere because of the very low efficiencies as observed here.

7

RECOMMENDATIONS

Even though, HEI has really low efficiencies in case of photo-electrochemical applications, photo-electrochemistry techniques provides for an easy tool to study plasmonics. Plasmonics is still a young field and hence there is always scope for further research. Some recommendations for further research are as follows :

- Nanoparticles with complex shapes are said to have high hot electron excitations due to high field enhancements [92]. Therefore, looking at the size dependence of HEI efficiency for nanoparticles of different shapes would be interesting and could also give more insight into the plasmon decay mechanism.
- Lossy metals used are one reason for low HEI efficiencies. Exploring other materials like certain semiconductor metamaterials [93] could result in higher efficiencies and hence worth researching.
- From this research, it was shown that lower nanoparticle sizes should be preferred to have higher HEI efficiencies. But going to lower sizes will also imply that related quantum factors starts to get important. Therefore, it is worth investing time to try and study what is the impact of these quantum factors on HEI efficiency at really small sizes of nanoparticles.
- The HEI efficiencies obtained here are lower compared to the previous work done within the MECS group on HEI [43], where a different electrolyte was used with other conditions remaining the same. Therefore, it will be interesting to see what the effect of electrolyte would be on the plasmonic HEI efficiency.
- HEI efficiency also depends on the metal-semiconductor Schottky barrier as discussed before. Therefore, it will be interesting to study HEI efficiency on multiple semiconductors or atleast look into the actual noble metal-semiconductor Schottky barriers of these combinations.
- Methanol was used in this study (in excess) as a hole scavenger, due to its favourable reduction potential. But the kinetic factors also play a role in the eventual reaction pathway selection and hence could be investigated. Different hole scavengers can also be tested to see if there is any change in the HEI efficiency.
- A luggin capillary could be used on the reference electrode for an even finer control on the working electrode potential.
- As mentioned before, precision study using lithography techniques could be explored to study the effect of nanoparticles dimers and dimer gaps on the HEI efficiency.

List of Figures

LIST OF TABLES

LIST OF ABBREVIATIONS AND SYMBOLS

ABBREVIATIONS

PEC	–	Photo-electrochemical
TEM	–	Transmission Electron Microscopy
XPS	–	X-Ray Photo-electron spectroscopy
MECS	–	Materials for Energy Conversion and Storage
OM	–	Opto-electronic Materials
TU	–	Technische Universiteit
UV – Vis	–	Ultra Violet – visible
Mtoe	–	Tonne of oil equivalent
LSPR	–	Localised Surface Plasmon Resonance
HEI	–	Hot Electron Injection
OBGE	–	Optical Band-Gap Edge
FTO	–	Flourine doped Tin-Oxide
IPCE	–	Incident Photon to Current conversion Efficiency
PV – E	–	Photovoltaic-electrolysis
NHE	–	Normal Hydrogen Electrode
SBH	–	Schottky Barrier Height
APCE	–	Absorbed Photon to Current conversion Efficiency
PIRET	–	Plasmon Induced Resonance Energy Transfer
DM	–	De-mineralised
HFS	–	High Frequency Spark
LFS	–	Low Frequency Spark
RLCS	–	Resistor-Inductor-Capacitance Spark
DMA	–	Differential Mobility Analyser
CPC	–	Condensation Particle Counter
PMT	–	Photo Multiplier
SHE	–	Standard Hydrogen Electrode
RHE	–	Reversible Hydrogen Electrode
EQE	–	External Quantum Efficiency
IQE	–	Internal Quantum Efficiency
DOS	–	Density of States

SYMBOLS

D	–	Dielectric displacement
E	–	Electric field
H	–	Magnetic field
J	–	Current density
B	–	Magnetic flux density
ρ	–	Charge density
ϵ	–	Electric permittivity
μ	–	Magnetic permeability
λ	–	Wavelength
U_E	–	Electric energy
U_H	–	Magnetic energy
U_K	–	Kinetic energy
ω	–	Frequency
k	–	Wave number
α	–	Polarizability
n	–	Refractive index
m	–	Relative refractive index
C	–	Area of cross-section
$\Im m$	–	Imaginary part
γ	–	Damping factor
N	–	Electron density
E_n^2	–	Plasmonic near field
E_f	–	Energy of fermi level
φ	–	Work function
χ	–	Electron affinity
E_g	–	Band gap energy
C_F	–	Fowler coefficient
c	–	Speed of light
h	–	Planck's constant
e	–	Charge of an electron
P	–	Power density
Au	–	Gold
Γ	–	Line width
τ	–	Dephasing time
$\hbar$	–	Reduced Planck's constant
g_s	–	Surface factor
v_f	–	Fermi velocity

κ_{rad}	–	Radiation damping constant
TiO_2	–	Titanium dioxide
E^0	–	Electrode potential
H^+	–	Hydrogen ion
e^-	–	Electron
h^+	–	Hole
H_2O	–	Water molecule
O_2	–	Oxygen molecule
H_2	–	Hydrogen molecule
$BiVO_4$	–	Bismuth Vanadate
Fe_2O_3	–	Iron (III) Oxide
Ag	–	Silver
$AgCl$	–	Silver Chloride

BIBLIOGRAPHY

[1] *Key world energy statistics*, Tech. Rep. (International Energy Agency (IEA), 2016).

[2] *2016 World Population Data Sheet*, Tech. Rep. (Population Reference Bureau, 2016).

[3] C. Clavero, *Plasmon-induced hot-electron generation at nanoparticle/metal-oxide interfaces for photovoltaic and photocatalytic devices,* Nature Publishing Group **8** (2014), 10.1038/NPHOTON.2013.238.

[4] M. Valenti, M. P. Jonsson, G. Biskos, A. Schmidt-Ott, and W. A. Smith, *Plasmonic nanoparticle-semiconductor composites for efficient solar water splitting,* J. Mater. Chem. A Published on (2016), 10.1039/c6ta06405a.

[5] A. Fatwa Firdaus, *Towards highly efficient bias-free solar water splitting,* Ph.D. thesis, Delft University of Technology (2013).

[6] A. Fujishima and K. Honda, *Electrochemical photolysis of water at a semiconductor electrode,* Nature **238**, 37 (1972).

[7] P. J. Boddy, *Oxygen Evolution on Semiconducting Ti02,* The Electrochemical Society **115**, 199 (1968).

[8] K. Sivula and R. Van De Krol, *Semiconducting materials for photoelectrochemical energy conversion,* Nature Reviews Materials **1**, 15010 (2016).

[9] A. J. Bard and M. A. Fox, *Artificial Photosynthesis: Solar Splitting of Water to Hydrogen and Oxygen Water Splitting,* Acc. Chem. Res **28**, 141 (1995).

[10] K. Maeda and K. Domen, *Photocatalytic water splitting: Recent progress and future challenges,* Journal of Physical Chemistry Letters (2010), 10.1021/jz1007966.

[11] J. Zhang, Y. Wu, M. Xing, S. Ahmed, K. Leghari, and S. Sajjad, *Development of modified N doped TiO 2 photocatalyst with metals, nonmetals and metal oxides,* Energy & Environmental Science (2010), 10.1039/b927575d.

[12] M. L. Brongersma, N. J. Halas, and P. Nordlander, *Plasmon-induced hot carrier science and technology,* Nature Nanotechnology (2015), 10.1038/NNANO.2014.311.

[13] K. L. Kelly, E. Coronado, L. L. Zhao, and G. C. Schatz, *The optical properties of metal nanoparticles: The influence of size, shape, and dielectric environment,* Journal of Physical Chemistry B (2003), 10.1021/jp026731y.

[14] B. H. A. Atwater, *The Promise of Plasmonics,* Scientific American (2007), 10.1038/scientificamerican0407-56.

[15] S. Eustis and M. A. El-Sayed, *Why gold nanoparticles are more precious than pretty gold: Noble metal surface plasmon resonance and its enhancement of the radiative and nonradiative properties of nanocrystals of different shapes,* Chemical Society Reviews (2005), 10.1039/b514191e.

[16] S. A. Maier and H. A. Atwater, *Plasmonics: Localization and guiding of electromagnetic energy in metal/dielectric structures,* Journal of Applied Physics **98**, 10 (2005).

[17] A. O. Govorov, H. Zhang, and Y. K. Gun'Ko, *Theory of photoinjection of hot plasmonic carriers from metal nanostructures into semiconductors and surface molecules,* Journal of Physical Chemistry C (2013), 10.1021/jp405430m.

[18] S. Mubeen, J. Lee, N. Singh, S. Krämer, G. D. Stucky, and M. Moskovits, *An autonomous photosynthetic device in which all charge carriers derive from surface plasmons,* Nature Nanotechnology (2013), 10.1038/NNANO.2013.18.

[19] J. B. Khurgin, *How to deal with the loss in plasmonics and metamaterials,* Nature Publishing Group **10** (2015), 10.1038/nnano.2014.310.

[20] R. Van De Krol and M. Grätzel, *Photoelectrochemical hydrogen production*, Vol. 90 (Springer, 2012) pp. 13–14.

[21] O. Khaselev and J. A. Turner, *A Monolithic Photovoltaic-Photoelectrochemical Device for Hydrogen Production via Water Splitting,* Science **280**, 425 (1998).

[22] W. A. Smith, *Photoelectrochemical Cell Design, Efficiency, Definitions, Standards, and Protocols,* in *Photoelectrochemical Solar Fuel Production* (Springer International Publishing, 2016) Chap. 4, pp. 163–197.

[23] G. Craig A., O. K. Varghese, and S. Ranjan, *Hydrogen generation by water splitting* (Springer US, 2008).

[24] M. F. Weber and M. J. Dignam, *Splitting water with semiconducting photoelectrodes-Efficiency considerations,* International Journal of Hydrogen Energy (1986), 10.1016/0360-3199(86)90183-7.

[25] A. B. Murphy, P. R. F. Barnes, L. K. Randeniya, I. C. Plumb, I. E. Grey, M. D. Horne, and J. A. Glasscock, *Efficiency of solar water splitting using semiconductor electrodes,* International Journal of Hydrogen Energy (2006), 10.1016/j.ijhydene.2006.01.014.

[26] J. R. Bolton, S. J. Strickler, and J. S. Connolly, *Limiting and realizable efficiencies of solar photolysis of water,* Nature **316**, 495 (1985).

[27] B. H. A. Atwater, *The Promise of Plasmonics,* Scientific American **296**, 56 (2009).

[28] S. A. Maier, *Plasmonics: Fundamentals and Applications* (Springer, 2007).

[29] A. Trügler, *Optical Properties of Metallic Nanoparticles: Basic Principles and Simulation* (Springer Series in Materials Science, 2015).

[30] J. B. Khurgin and A. Boltasseva, *Reflecting upon the losses in plasmonics and metamaterials,* MRS bulletin **37**, 768 (2012).

[31] G. Mie, *Beiträge zur Optik trüber Medien, speziell kolloidaler Metallösungen,* Annalen der Physik **330**, 377 (1908).

[32] M. Quinten, *Optical Properties of Nanoparticle Systems : Mie and Beyond* (John Wiley & Sons, Incorporated, 2010).

[33] J. A. Scholl, A. L. Koh, and J. A. Dionne, *Quantum plasmon resonances of individual metallic nanoparticles,* Nature **483** (2012), 10.1038/nature10904.

[34] S. Enoch and N. Bonod, *Plasmonics: From Basics to Advanced Topics* (Springer, 2012) p. 167.

[35] S. Link and M. A. El-Sayed‹, *Shape and size dependence of radiative, non-radiative and photothermal properties of gold nanocrystals,* International Reviews in Physical Chemistry **19**, 409 (2000).

[36] G. Xu, M. Tazawa, P. Jin, S. Nakao, and K. Yoshimura, *Wavelength tuning of surface plasmon resonance using dielectric layers,* Applied Physics Letters **82** (2003), 10.1063/1.1578518.

[37] S. Linic, P. Christopher, and D. B. Ingram, *Plasmonic-metal nanostructures for efficient conversion of solar to chemical energy,* Nature Materials **10** (2011), 10.1038/NMAT3151.

[38] S. Link, Z. L. Wang, and M. A. El-Sayed, *Alloy Formation of Gold-Silver Nanoparticles and the Dependence of the Plasmon Absorption on Their Composition,* Journal of Physical Chemistry B **103** (1999), 10.1021/jp990387w.

[39] C. Deeb, X. Zhou, J. Plain, G. P. Wiederrecht, R. Bachelot, M. Russell, and P. K. Jain, *Size dependence of the plasmonic near-field measured via single-nanoparticle photoimaging,* Journal of Physical Chemistry C **117**, 10669 (2013).

[40] M. Meier and A. Wokaun, *Enhanced fields on large metal particles: dynamic depolarization,* OPTICS LETTERS **8**, 581 (1983).

[41] A. Manjavacas, J. G. Liu, V. Kulkarni, and P. Nordlander, *Plasmon-induced hot carriers in metallic nanoparticles,* ACS Nano **8**, 7630 (2014).

[42] S. Mukherjee, F. Libisch, N. Large, O. Neumann, L. V. Brown, J. Cheng, J. B. Lassiter, E. A. Carter, P. Nordlander, and N. J. Halas, *Hot electrons do the impossible: Plasmon-induced dissociation of H 2 on Au,* Nano Letters **13**, 240 (2013).

[43] M. Valenti, A. Venugopal, D. Tordera, M. P. Jonsson, G. Biskos, A. Schmidt-Ott, and W. A. Smith, *Hot Carrier Generation and Extraction of Plasmonic Alloy Nanoparticles,* ACS Photonics (2017), 10.1021/acsphotonics.6b01048.

[44] G. Zhao, H. Kozuka, and T. Yoko, *Sol-gel preparation and photoelectrochemical properties of TiO2 films containing Au and Ag metal particles,* Thin Solid Films **277**, 147 (1996).

[45] Y. Nishijima, K. Ueno, Y. Kotake, K. Murakoshi, H. Inoue, and H. Misawa, *Near-infrared plasmon-assisted water oxidation,* Journal of Physical Chemistry Letters **113**, 13433 (2012).

[46] Z. H. Chen, Y. B. Tang, C. P. Liu, Y. H. Leung, G. D. Yuan, L. M. Chen, Y. Q. Wang, I. Bello, J. A. Zapien, W. J. Zhang, C. S. Lee, and S. T. Lee, *Vertically aligned ZnO nanorod arrays sentisized with gold nanoparticles for schottky barrier photovoltaic cells,* Journal of Physical Chemistry C **3**, 1248 (2009).

[47] B. Sharma, *Metal-semiconductor Schottky barrier junctions and their applications*, 1st ed. (Springer US, 2013) pp. 2–6.

[48] R. E. Hummel, *Electronic Properties of Materials*, 4th ed. (Springer Sciene & Business Media, 2011) pp. 247–251.

[49] R. Sundararaman, P. Narang, A. S. Jermyn, W. A. Goddard Iii, and H. A. Atwater, *Theoretical predictions for hot-carrier generation from surface plasmon decay,* Nature Communications **5** (2014), 10.1038/ncomms6788.

[50] R. H. Fowler, *The analysis of photoelectric sensitivity curves for clean metals at various temperatures,* Physical Review **38** (1931), 10.1103/PhysRev.38.45.

[51] C. Wilmsen, *Physics and chemistry of III-V compound semiconductor interfaces* (Springer US, 2013) pp. 98–101.

[52] S. K. Cushing, J. Li, F. Meng, T. R. Senty, S. Suri, M. Zhi, M. Li, A. D. Bristow, and N. Wu, *Photocatalytic activity enhanced by plasmonic resonant energy transfer from metal to semiconductor,* Journal of the American Chemical Society **134**, 15033 (2012).

[53] *Arzuffi SRL,* (2017).

[54] E. Have ten, *Investigation of the photochromic properties of Dysprosium Oxyhydride*, Ph.D. thesis, Delft University of Technology (2016).

[55] AJA International Inc. USA, *Magnetron sputtering,* (2017).

[56] D.-J. Won, C.-H. Wang, H.-K. Jang, and D.-J. Choi, *Effects of thermally induced anatase-to-rutile phase transition in MOCVD-grown TiO 2 films on structural and optical properties,* Applied Physics A **73**, 595 (2001).

[57] J. N. Kondo and K. Domen, *Crystallization of mesoporous metal oxides,* Chemistry of Materials (2008), 10.1021/cm702176m.

[58] N.-G. Park, J. Van De Lagemaat, and A. J. Frank, *Comparison of Dye-Sensitized Rutile-and Anatase-Based TiO 2 Solar Cells,* The Journal of Physical Chemistry B **104**, 8989 (2000).

[59] S. Schwyn, E. Garwin, and A. Schmidt-Ott, *Aerosol generation by spark discharge,* Journal of Aerosol Science **19**, 639 (1988).

[60] J. Feng, X. Guo, N. Ramlawi, T. V. Pfeiffer, R. Geutjens, S. Basak, H. Nirschl, G. Biskos, H. W. Zandbergen, and A. Schmidt-Ott, *Green manufacturing of metallic nanoparticles: a facile and universal approach to scaling up,* Journal of Materials Chemistry A **4**, 11222 (2016).

[61] B. O. Meuller, M. E. Messing, D. L. J. Engberg, A. M. Jansson, L. I. M. Johansson, S. M. Norlén, N. Tureson, and K. Deppert, *Aerosol Science and Technology Review of Spark Discharge Generators for Production of Nanoparticle Aerosols Review of Spark Discharge Generators for Production of Nanoparticle Aerosols,* Aerosol Science and Technology **4611** (2012), 10.1080/02786826.2012.705448.

[62] T. V. Pfeiffer, J. Feng, and A. Schmidt-Ott, *New developments in spark production of nanoparticles,* Advanced Powder Technology **25**, 56 (2014).

[63] J. H. Byeon, J. H. Park, and J. Hwang, *Spark generation of monometallic and bimetallic aerosol nanoparticles,* Journal of Aerosol Science **39**, 888 (2008).

[64] N. S. Tabrizi, Q. Xu, N. M. Van Der Pers, U. Lafont, and A. Schmidt-Ott, *Synthesis of mixed metallic nanoparticles by spark discharge,* Journal of Nanoparticle Research **11** (2009), 10.1007/s11051-008-9568-8.

[65] A. M. and L. E., *The evolution of spark discharges in gases: I. Macroscopic models,* Journal of Physics D: Applied Physics **29**, 2129 (1996).

[66] J. Feng, G. Biskos, and A. Schmidt-Ott, *Toward industrial scale synthesis of ultrapure singlet nanoparticles with controllable sizes in a continuous gas-phase process,* Nature Publishing Group **5** (2015), 10.1038/srep15788.

[67] E. Hontañón, F. E. Kruis, and E. Hontã Nón, *Aerosol Science and Technology A Differential Mobility Analyzer (DMA) for Size Selection of Nanoparticles at High Flow Rates A Differential Mobility Analyzer (DMA) for Size Selection of Nanoparticles at High Flow Rates,* Aerosol Science and Technology **43**, 25 (2009).

[68] *Lambda 800/900 User's Guide,* (2001).

[69] F. F. Abdi and R. Van De Krol, *Nature and light dependence of bulk recombination in Co-Pi-catalyzed BiVO 4 photoanodes,* Journal of Physical Chemistry C **116** (2012), 10.1021/jp3007552.

[70] Z. Chen, H. N. Dinh, and E. Miller, *Photoelectrochemical Water Splitting Standards, Experimental Methods, and Protocols* (Springer New York, 2013).

[71] O. G. Palanna, *Engineering chemistry* (Tata McGraw-Hill Education, 2009) pp. 489–490.

[72] M. Valenti, E. Kontoleta, I. A. Digdaya, M. P. Jonsson, G. Iskos, A. Schmidt-Ott, and W. A. Smith, *The Role of Size and Dimerization of Decorating Plasmonic Silver Nanoparticles on the Photoelectrochemical Solar Water Splitting Performance of BiVO 4 Photoanodes,* ChemNanoMat **2**, 739 – 747 (2016).

[73] D. C. Marinica, A. K. Kazansky, P. Nordlander, J. Aizpurua, and A. G. Borisov, *Quantum plasmonics: nonlinear effects in the field enhancement of a plasmonic nanoparticle dimer,* Nano letters **12**, 1333 (2012).

[74] J. Li, S. K. Cushing, F. Meng, T. R. Senty, A. D. Bristow, and N. Wu, *Plasmon-induced resonance energy transfer for solar energy conversion,* Nature Photonics **9** (2015), 10.1038/NPHOTON.2015.142.

[75] R. D. Glover, J. M. Miller, and J. E. Hutchison, *Generation of metal nanoparticles from silver and copper objects: Nanoparticle dynamics on surfaces and potential sources of nanoparticles in the environment,* ACS Nano **5**, 8950–8957 (2011).

[76] E. Hao and G. C. Schatz, *Electromagnetic fields around silver nanoparticles and dimers,* Journal of Chemical Physics **120** (2004), 10.1063/1.1629280.

[77] E. Ricci and R. Novakovic, *Wetting and Surface Tension Measurements on Gold Alloys,* Gold Bulletin **34**, 41 (2001).

[78] A. M. Brown, R. Sundararaman, P. Narang, W. A. Goddard, and H. A. Atwater, *Nonradiative plasmon decay and hot carrier dynamics: Effects of phonons, surfaces, and geometry,* ACS Nano **10** (2016), 10.1021/acsnano.5b06199.

[79] M. Bernardi, J. Mustafa, J. B. Neaton, and S. G. Louie, *Theory and computation of hot carriers generated by surface plasmon polaritons in noble metals,* Nature Communications **6** (2015), 10.1038/ncomms8044.

[80] D. Rioux, S. Vallières, S. Besner, P. Muñoz, E. Mazur, and M. Meunier, *An analytic model for the dielectric function of Au, Ag, and their Alloys,* Advanced Optical Materials **2** (2014), 10.1002/adom.201300457.

[81] H. B. Michaelson, *The work function of the elements and its periodicity,* Applied Physics Letters **48** (1991), 10.1063/1.105227.

[82] F. Hossein-Babaei, M. M. Lajvardi, and N. Alaei-Sheini, *The energy barrier at noble metal/TiO2 junctions,* Applied Physics Letters **106** (2015), 10.1063/1.4913667.

[83] W.-X. Li, C. Stampfl, and M. Scheffler, *Oxygen adsorption on Ag (111): A density-functional theory investigation,* PHYSICAL REVIEW B **65** (2002), 10.1103/PhysRevB.65.075407.

[84] M. Francombe and J. Vossen, *Advances in Research and Development: Heterojunctions for High-speed and Infrared Applications* (Academic Press, 1998) pp. 91–92.

[85] J. Olson, S. Dominguez-Medina, A. Hoggard, L.-Y. Wang, W.-S. Chang, and S. Link, *Optical characterization of single plasmonic nanoparticles,* Chem. Soc. Rev. Chem. Soc. Rev **40**, 40 (2015).

[86] H. Baida, P. Billaud, S. Marhaba, D. Christofilos, E. Cottancin, A. Crut, J. Lerme, P. Maioli, M. Pellarin, M. Broyer, N. Del Fatti, F. Vallee, A. Sanchez-Iglesias, I. Pastoriza-Santos, and L. M. Liz-Marzan, *Quantitative determination of the size dependence of surface plasmon resonance damping in single Ag@SiO2 nanoparticles,* Nano Letters **9** (2009), 10.1021/nl901672b.

[87] C. Novo, D. Gomez, J. Perez-Juste, Z. Zhang, H. Petrova, M. Reismann, P. Mulvaney, and G. V. Hartland, *Contributions from radiation damping and surface scattering to the linewidth of the longitudinal plasmon band of gold nanorods: a single particle studyw,* Physical Chemistry Chemical Physics **8** (2006), 10.1039/b604856k.

[88] J. W. Mitchell and R. G. Goodrich, *Fermi velocities in silver: Surface Landau-level resonances,* Physical Review B **32** (1985), 10.1103/PhysRevB.32.4969.

[89] H. Harutyunyan, A. B. F. Martinson, D. Rosenmann, L. K. Khorashad, L. V. Besteiro, A. O. Govorov, and G. P. Wiederrecht, *Anomalous ultrafast dynamics of hot plasmonic electrons in nanostructures with hot spots,* Nature nanotechnology **10** (2015), 10.1038/NNANO.2015.165.

[90] P. Reineck, D. Brick, P. Mulvaney, and U. Bach, *Plasmonic Hot Electron Solar Cells: The Effect of Nanoparticle Size on Quantum Efficiency,* The Journal of Physical Chemistry Letters **7**, 4137 (2016).

[91] J. A. Scholl, A. García-Etxarri, A. L. Koh, and J. A. Dionne, *Observation of quantum tunneling between two plasmonic nanoparticles,* Nano letters **13**, 564 (2013).

[92] M. C.-H. B. R.-G. M. P.-L. Z. W. X.-T. K. A. O. G. Sousa-Castillo, Ana and M. A. Correa-Duarte, *Boosting Hot Electron-Driven Photocatalysis through Anisotropic Plasmonic Nanoparticles with Hot Spots in Au-TiO2 Nanoarchitectures,* Journal of Physical Chemistry C **120** (2016), 10.1021/acs.jpcc.6b02370.

[93] A. J. Hoffman, L. Alekseyev, S. S. Howard, K. J. Franz, D. Wasserman, V. A. Podolskiy, E. E. Narimanov, D. L. Sivco, and C. Gmachl, *Negative refraction in semiconductor metamaterials,* Nature Materials (2007), 10.1038/nmat2033.

A

APPENDIX A

ENERGY DENSITY OF DIFFERENT ENERGY STORAGE TECHNIQUES

Energy storage	Energy density	
	Gravimetric (MJ/kg)	Volumetric (MJ/L)
Mechanical		
Compressed air	0.512	0.16 (300 bar)
Pump water uphill	0.001	0.001
Capacitors		
Supercapacitor	0.01	—
Ultracapacitor	0.0206	—
Batteries		
Pb	0.14-0.17	—
NiCd	0.14-0.22	—
Li-ion	0.54-0.72	—
Fuels		
Coal	24	—
Wood	16	—
Gasoline	44	35
Diesel	46	37
Methanol	20	18
Natural gas	54	0.036
Hydrogen	143	0.011 5.6 (700 bar)

Figure A.1: Typical energy density obtained through different energy storage techniques [5]

B

APPENDIX-B

PROCESS CONDITIONS FOR THE SPARK GENERATOR AND THE DMA

Process conditions in the spark generator and size selection system for the reported samples.

Please note : Match both boxes based on serial numbers.

Sl. No.	Electrodes	Spark type	Carrier gas flow	Set frequency/Current	Gap voltage	Oven temperature
1.	Silver	HFS	7 lpm	1500 Hz	235 V	905 C
2.	Alloy	LFS	2 lpm	42 mA	0.64 kV	905 C
3.	Gold	LFS	2 lpm	6 mA	1.82 kV	1000 C
4.	Silver	HFS	7 lpm	1000 Hz	376.2 V	905 C
5.	Silver	HFS	7 lpm	1500 Hz	322.1 V	905 C
6.	Silver	HFS	7 lpm	1500 Hz	274 V	905 C
7.	Silver	HFS	7 lpm	1500 Hz	302.5 V	905 C
8.	Silver	HFS	7 lpm	1500 Hz	273.2 V	930 C
9.	Silver	HFS	7 lpm	1500 Hz	316 V	930 C
10.	Silver	HFS	7 lpm	1500 Hz	265 V	930 C
11.	Silver	HFS	7 lpm	1500 Hz	286 V	930 C
12.	Silver	LFS	5 lpm	48.2 mA	0.69 kV	905 C
13.	Silver	LFS	5 lpm	42.4 mA	0.9 kV	905 C
14.	Silver	LFS	5 lpm	50.5 mA	0.73 kV	905 C

Table B.1: Settings used in the spark discharge setup (1/2)

Sl. No.	DMA voltage/Particle size	DMA flow	Sheath air flow	Average concentration (CPC)	Deposition time
1.	275 V/15 nm	2.282 lpm	9.01 lpm	$4 * 10^5 P/ccm$	30 min
2.	275 V/15 nm	2.284 lpm	9.01 lpm	$5.9 * 10^5 P/ccm$	30 min
3.	275 V/15 nm	2.270 lpm	9.01 lpm	$6.2 * 10^5 P/ccm$	25 min
4.	85 V/8 nm	2.281 lpm	9.01 lpm	$1.2 * 10^5 P/ccm$	180 min
5.	115 V/9 nm	2.259 lpm	9.01 lpm	$1.2 * 10^5 P/ccm$	165 min
6.	185 V/11 nm	2.260 lpm	9.01 lpm	$2.7 * 10^5 P/ccm$	80 min
7.	215 V/14 nm	2.250 lpm	9.01 lpm	$2.5 * 10^5 P/ccm$	50 min
8.	310 V/17 nm	2.270 lpm	9.01 lpm	$2.8 * 10^5 P/ccm$	40 min
9.	372 V/19 nm	2.245 lpm	9.01 lpm	$4.2 * 10^5 P/ccm$	20 min
10.	476 V/22 nm	2.256 lpm	9.01 lpm	$2.6 * 10^5 P/ccm$	23 min
11.	550 V/24 nm	2.251 lpm	9.01 lpm	$2.5 * 10^5 P/ccm$	25 min
12.	215 V/14 nm	2.209 lpm	9.01 lpm	$5.5 * 10^5 P/ccm$	40 min
13.	215 V/14 nm	2.203 lpm	9.01 lpm	$1.5 * 10^5 P/ccm$	120 min
14.	215 V/14 nm	2.237 lpm	9.01 lpm	$1.3 * 10^5 P/ccm$	51 min

Table B.2: Settings used in the spark discharge setup (2/2)

C

APPENDIX-C

CALCULATIONS FOR THE PREPARATION OF 0.1 M POTASSIUM PHOSPHATE BUFFER

A potassium phosphate buffer of pH = 7 was used in this study to avoid fluctuations in local pH that could effect the flat-band potential. The potassium phosphate buffer is prepared by dissolving appropriate amounts of mono-basic and di-basic potassium phosphate in DM water. Calculations were performed, using the Henderson - Hasselbalch equation, to estimate the exact amounts of the potassium phosphate mono-basic and di-basic salts (Sigma-Aldrich) to be added. A pKa = 6.86 was used for the calculations [ref].

$$pH = pKa + log\frac{[A]}{[HA]} \tag{C.1}$$

where, HA (proton donor) is the potassium phosphate monobasic salt (Sigma-Aldrich) and A (proton acceptor) is the potassium phosphate dibasic salt (Sigma-Aldrich).

simplifying,

$$\frac{A}{HA} = 1.38 \tag{C.2}$$

and,

$$A + HA = 0.1 \tag{C.3}$$

Therefore,

$$HA = 0.042M = 5.716g \tag{C.4}$$

$$A = 0.058M = 10.1036g \tag{C.5}$$

These amounts of salts were dissolved in 1 litre of DM water.

D

APPENDIX-D

POWER CALIBRATION OF THE LAMP USED FOR IPCE MEASUREMENTS

Power calibration of the Xenon lamp used for the IPCE measurements was performed using an optical diode. Light intensity (in μW) was measured as a function of wavelength and used to correct the photo-current measurements to express in the IPCE % format. Figure D.1 shows the measured readings. The measurements shows that the intensity has not changed much during the course of the experiments. The difference that is seen could be due to the human error in the measurements because of the placement of the diode each time.

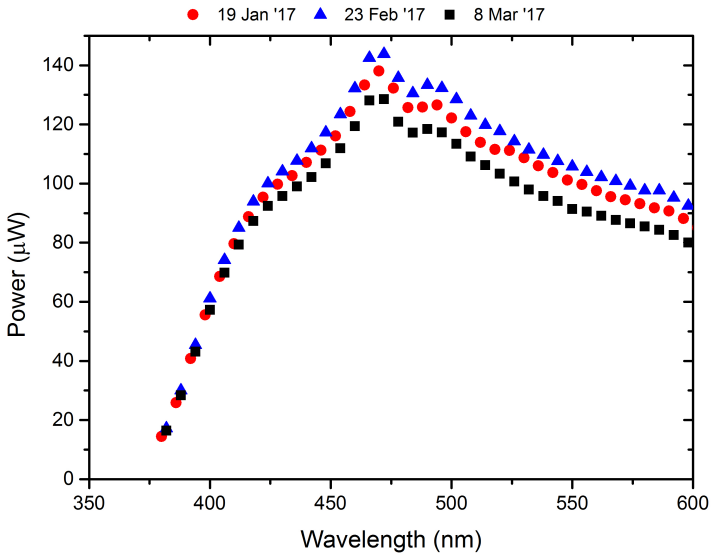

Figure D.1: Results from the power calibration performed at three different instances during the experimentation period, marked with the dates

E

APPENDIX-E

DETAILS OF THE CURVE FITTING USING FOWLER'S THEORY

This section shows the details of the fitting of the Fowler equation to the APCE of the ~ 16 nm silver nanoparticles. Figure E.1 shows the residual distribution obtained from the fitting. The residuals are evenly distributed, implying a good fit of the Fowler equation. Figure E.2 summarises the details of the fitting with the model equation used. This table was obtained from the Origin software used for fitting.

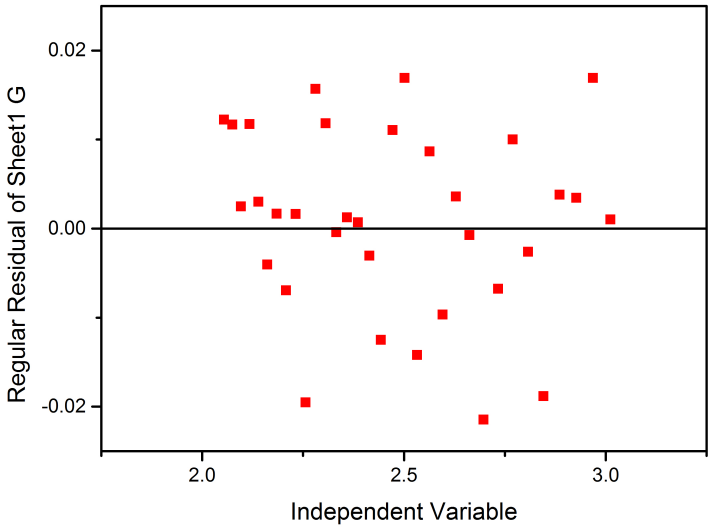

Figure E.1: Residual distribution of the fitting of the Fowler theory showing an even distribution across the 0 point

	A	B	C	D
1	Model	NewFunction4 (User)		
2	Equation	C*((x-S)^2)/x		
3	Reduced Chi-Sqr	1.13344E-4		
4	Adj. R-Square	0.97569		
5			Value	Standard Error
6	G	C	0.65301	0.03965
7		S	1.98768	0.02295

Figure E.2: Table obtained from the Origin software used for fitting showing a 97.7% adjusted R^2 value

F

APPENDIX-F

APCE RESULTS FROM INITIAL RESULTS OF THE SIZE DEPENDENCE OF THE HEI EFFICIENCY

The initial results of the $APCE_{max}$ with nanoparticle size is plotted in figure F.1. The silver particle degradation on exposure to moisture was only noticed after these set of samples. These samples also had a lot of agglomeration. These set of experiments were redone to rectify the degradation and also to minimise the agglomeration. The trend seen in F.1 is very similar to the result obtained in the second try as well. This confirms that the trend is not from an experimental/human error.

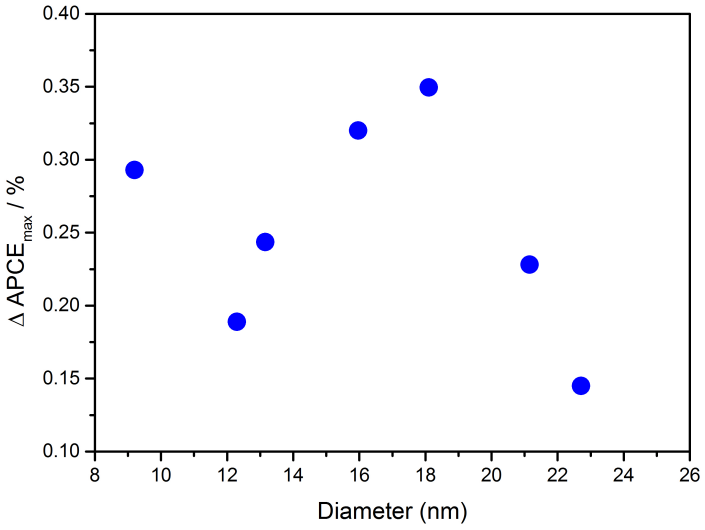

Figure F.1: $APCE_{max}$ values of different sized silver nanoparticles

G

APPENDIX-G

DETAILS OF GAUSSIAN CURVE FITTING FOR PARTICLES OF DIFFERENT SIZE

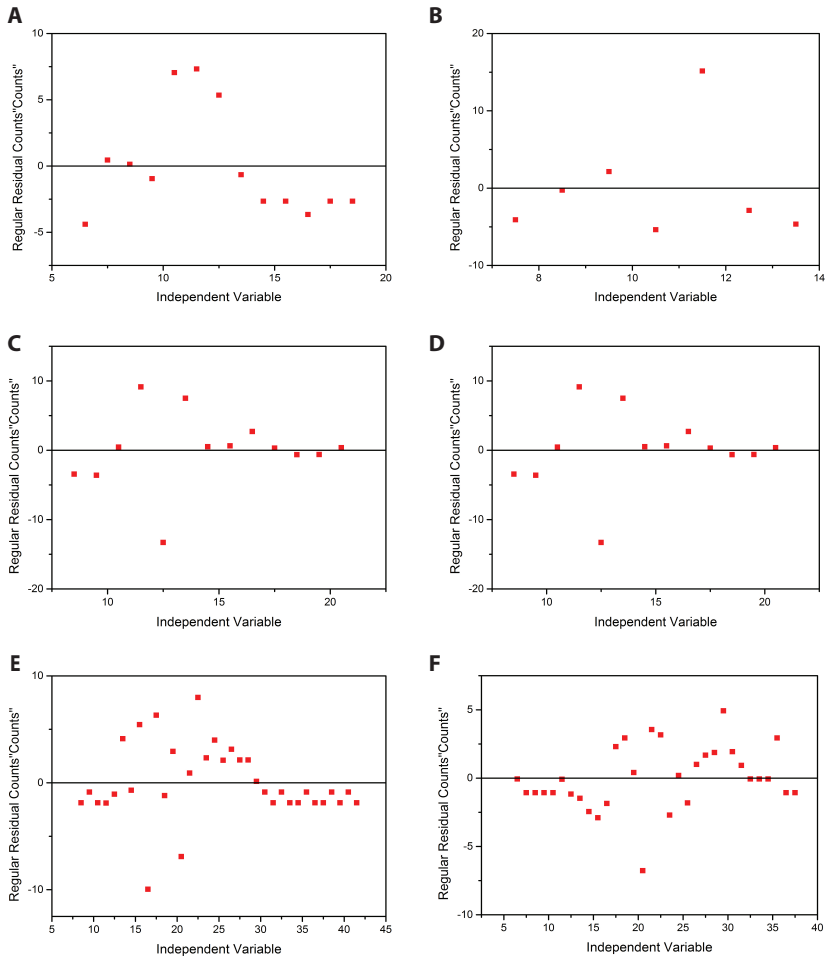

Figure G.1: Residuals for Gaussian curve fitting into size distribution of silver nanoparticle of size A) 8.47 nm B) 9.49 nm C) 11.84 nm D) 14.80 nm E) 18.41 nm and F) 20.32 nm

The adjusted R^2 value for the curve fitting are tabulated in G.1.

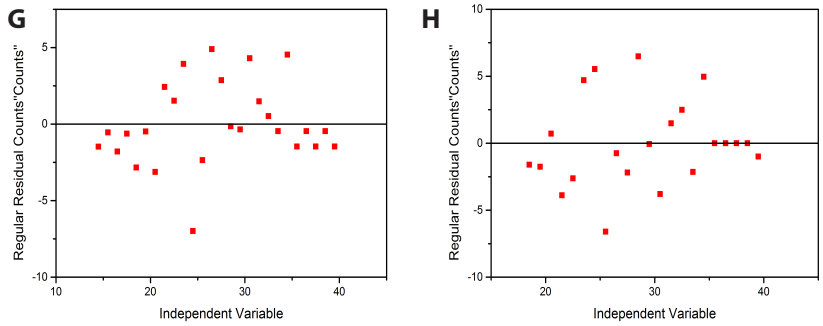

Figure G.2: Residuals for Gaussian curve fitting into size distribution of silver nanoparticle of size G) 23.32 nm and H) 25.42 nm

Diameter (nm)	Adjusted R^2 (%)
8.47	97.7
9.49	91.9
11.8	92.2
14.80	97.19
18.41	89.8
20.32	95.5
23.32	94.37
25.42	90.8

Table G.1: Values of adjusted R^2 for Gaussian curve fitting to the size distributions for different particle diameters

DETAILS OF GAUSSIAN CURVE FITTING FOR PARTICLES OF DIFFERENT COMPOSITION

The adjusted R^2 value for the curve fitting are tabulated in G.2.

Material	Adjusted R^2 (%)
Silver	88.5
Alloy	97.2
Gold	93.9

Table G.2: Values of adjusted R^2 for Gaussian curve fitting to the size distributions for particles of different composition

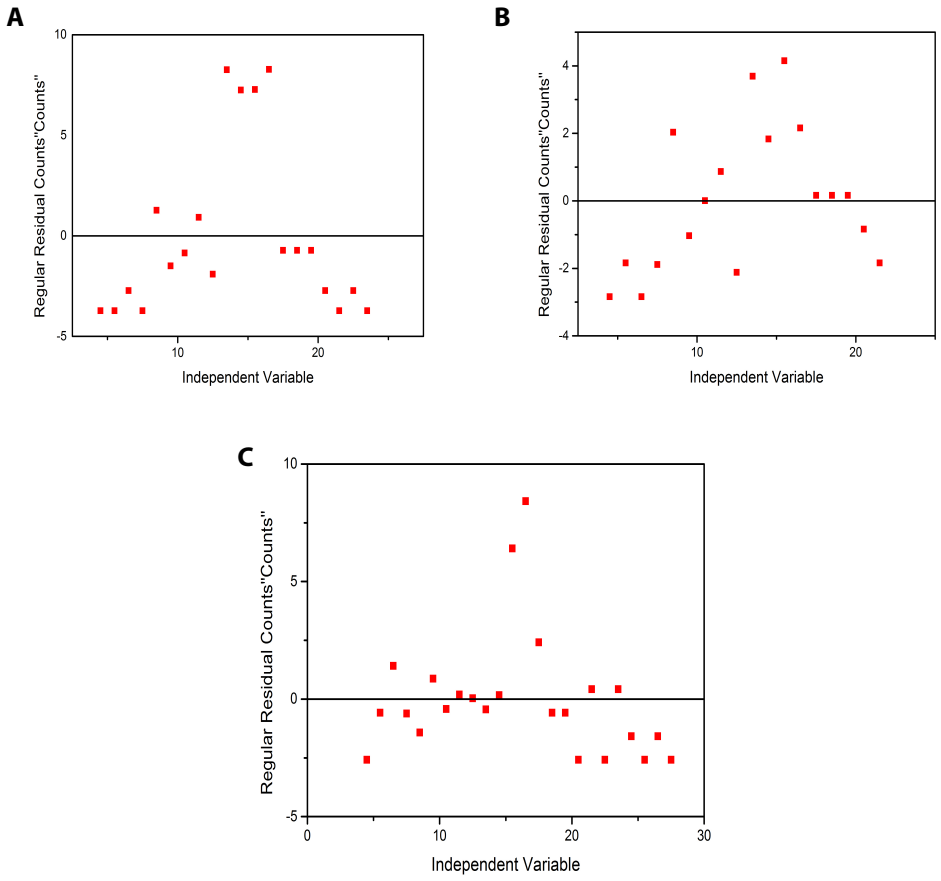

Figure G.3: Residuals for Gaussian curve fitting into size distribution of nanoparticles of different composition A) Silver B) Alloy C) Gold